Institute of Experimental Pharmacology and Toxicology
Centre for Experimental Medicine
University Medical Centre Hamburg-Eppendorf

Evidence for the inhibition of cardiomyocytes cycle activity by cardiac contraction

Dissertation
submitted to the Department of Biology
Faculty of Mathematics, Informatics, and Natural Sciences
University of Hamburg

for the degree of
Doctor of Natural Sciences
(Dr. rer. nat.)

By
Nancy Sorial Samy Shehata

Born in Cairo, Egypt
Hamburg 2025

First examiner: Prof. Dr. Baris Tursun
Second examiner: Assoc. Prof. Dr. Florian Weinberger

Defence committee:

1. Prof. Dr. Baris Tursun
2. Assoc. Prof. Dr. Florian Weinberger
3. Prof. Dr. Lucie Carrier
4. Prof. Dr. Christian Lohr
5. Prof. Dr. Kathrin Anna Otte

Date of disputation: 21/01/2026

Carried out in the Institute of Experimental Pharmacology and Toxicology from January 2022 to September 2025

i. PUBLICATIONS AND CONGRESS PARTICIPATIONS

Publications:

Shehata, N., Srikantharajah, R., Baier, E., Manthey, C., Stüdemann, T., Nehring, M., Covic, A., Müller, C., Siebels, B., Nissen, P., Witten, A., Castellano, M. Z., Rodriguez, Y., Gomez, L. Z., Janssen, I., Rodriguez, J., Enriquez, A. G., Romero, M. A. G., Di Mattia, R., … Weinberger, F. (2025). Contractility governs cardiomyocyte cell cycle activity. bioRxiv, 2025.08.19.671096. https://doi.org/10.1101/2025.08.19.671096

Sönmez, M., Stüdemann, T., Manthey, C., Covic, A., **Shehata, N**., Im, J., Schwarzova, B., Rössinger, J., Srikantharajah, R., Shibamiya, A., Schwedhelm, E., Eschenhagen, T., Christ, T., & Weinberger, F. (2025). Modulation of cardiomyocyte contractility and action potentials with chemogenetic chloride currents. The Journal of Physiology, 603(6), 1399–1415. https://doi.org/10.1113/JP286428

König, K., König, A., Pankin, D., Skorsetz, M., Weinberger, F., **Shehata, N**., Agarwal, K., & Duocastella, M. (2025). Label-free multimodal femtosecond fiber laser microscopy of engineered heart tissue with acousto-optic deflectors. Multiphoton Microscopy in the Biomedical Sciences XXV, 13324, 50–58. https://doi.org/10.1117/12.3039099

Congress Participations:

Nancy Shehata, Tim Stüdemann, Rajiven Srikantharajah, Marie Nehring, Anita Covic, Judith Rössinger, Barbora Schwarzová, Bente Siebels, Paula Nissen, Christian Müller, Thomas Eschenhagen, Florian Weinberger. **Evidence for the inhibition of cardiomyocyte cell cycle activity by cardiac work**. Gordon research conference 2024

Nancy Shehata, Tim Stüdemann, Rajiven Srikantharajah, Marie Nehring, Anita Covic, Judith Rössinger, Barbora Schwarzová, Bente Siebels, Paula Nissen, Christian Müller, Thomas Eschenhagen, Florian Weinberger. **Evidence for the inhibition of cardiomyocyte cell cycle activity by cardiac work**. Cardiovascular Bioengineering Symposium CNIC Conference 2025. Awards: Recognition Award for one of the best posters.

ISHR 2025 Nancy Shehata, Tim Stüdemann, Rajiven Srikantharajah, Marie Nehring, Anita Covic, Judith Rössinger, Barbora Schwarzová, Bente Siebels, Paula Nissen, Christian Müller, Thomas Eschenhagen, Florian Weinberger. **Evidence for the inhibition of cardiomyocyte cell cycle activity by cardiac work**. International Society for Heart Research 2025.

ii. Table of Contents

iii. Abbreviations

Abbreviation	Definition
2D	Two-dimensional
3D	Three-dimensional
AAV6	Adeno Associated Virus serotype 6
ACN	Acetonitrile
ACTC1	Actin Alpha Cardiac Muscle 1
ACTN2	α-actinin
AGC	Automatic Gain Control
AI	Artificial intelligence
ANOVA	Analysis of Variance
AP	Action potentials
APC	Allophycocyanin
ATM	Ataxia-Telangiectasia Mutated
ATP	Adenosine triphosphate
ATR	Ataxia-Telangiectasia and Rad3-Related
BCA	Bicinchoninic acid
BEH	Ethylene bridged hybrid
BMP4	Bone morphogenic protein
BP	Biological processes
BSA	Bovine serum albumin
BTS	N-benzyl-p-toluenesulfonamide
CDK	Cyclin-dependent kinases
CENPF	Centromere protein F
CICR	Calcium-induced calcium release
CKI	CDK inhibitors
CM	Cardiomyocytes
CO_2	Carbon dioxide gas
CRISPR	Clustered regularly interspaced short palindromic repeats
CSV	Comma separated values
CTNT	Cardiac troponin T
DCM	Dilated cardiomyopathy
DDA	Data-Dependent Acquisition
DDR	DNA damage response
DEG	Differentially expressed genes
DMEM	Dulbecco's Modified Eagle Medium
DMSO	Dimethyl Sulfoxide
DNA	Deoxyribonucleic acid

DPBS	Dulbecco's Phosphate Buffered Saline
DSB	Double stranded break
DTT	Dithiothreitol
EB	Embryoid bodies
ECC	Excitation contraction coupling
ECM	Extra-cellular matrix
EDTA	Ethylenediaminetetraacetic acid
EDU	5-Ethynyl-2`-deoxyuridine
EHT	Engineered heart tissue
ERK	Extracellular signal-regulated kinases
ESC	Embryonic stem cells
ESI	Electrospray Ionization
FACS	Fluorescence-Activated Cell Sorting
FBS	Fetal Bovine Serum
FDA	Food and drug administration
FDR	False discovery rate
FGF	Fibroblast growth factor
FOXM1	Forkhead box protein M1
FSC	Forward scatter
FTDA	bFGF, TGF-β1, Dorsomorphin, Activin-A
GFP	Green fluorescent protein
GO	Gene ontology
GSEA	Gene set enrichment analysis
HBSS	Hank's Balanced Salt Solution
HCD	Higher-energy Collisional Dissociation
HCN4	hyperpolarization-activated cyclic nucleotide-gated
HDR	Homology directed repair
HEK	Human embryonic kidney cells
HIPSC	Human induced pluripotent stem cells
HIV	Human immunodeficiency virus
HRP	Horseradish peroxidase
HSA	Human serum albumin
IGF	Insulin-like growth factor
I_{K1}	Inwardly rectifying potassium current
KCNQ1	Potassium voltage-gated channel subfamily member 1
KEGG	Kyoto Encyclopedia of Genes and Genomes
LDH	Lactate dehydrogenase
LNP	Lipid nanoparticles
LVAD	Left ventricular assisting device
MAPK	Mitogen-Activated Protein Kinase

MEF2	Myocyte enhancer factor 2
MG	Matrigel
MHC	Major histocompatibility complex
MNDCM	mononuclear diploid cardiomyocytes
MRTF	Myocardin-related transcription factor
MS	Mass spectroscopy
MYH6	Myosin heavy chain α isoform
NCX1	Sodium-calcium exchanger
NFAT	Nuclear Factor of Activated T-cells
NHEJ	Non homologous end joining
O_2	Oxygen
ORA	Over-representation analysis
PCR	Poly chain reaction
PFA	Paraformaldehyde
PGC	Proliferator-Activated Receptor Gamma Coactivator
PH3	Phospho-histone H3
PI3K	Phosphoinositide 3-kinases
PKA	Protein kinase A
PLK1	Polo-like kinase 1
PLN	Phospholamban
PPAR	Peroxisome Proliferator-Activator Receptor
PSAM	Pharmacologically Selective Actuator Module
$PSEM^{89S}$	Pharmacological small effector molecule
PVDF	Polyvinylidene Difluoride
RFP	Red fluorescent protein
RNA	Ribonucleic acid
RNP	Ribonucleoprotein
ROCK	Rho-associated protein kinases
ROI	Region of interest
ROS	Reactive oxygen species
RPM	Rotation per minute
RPMI 1640	Roswell Park Memorial Institute 1640
RT	Room temperature
SAC	Spindle assembly checkpoint
SarcAsM	Sarcomere Analysis Multitool
SBS	Sequencing by synthesis
SCN5A	Sodium channel protein type 5 subunit alpha,
SD	Standard deviation
SDC	Sodium deoxycholate
SDS PAGE	Sodium dodecyl sulphate polyacrylamide gel electrophoresis

SEM	Standard error of the mean
SERCA	Endoplasmic Reticulum Calcium ATPase
SiRNA	Small interfering RNA
SP3	Single-pot, solid-phase-enhanced sample-preparation
SR	Sarcoplasmic reticulum
SRE	serum response elements
SRF	Serum response factor
SSEA3	Stage-specific embryonic antigen 3
STAR	Spliced Transcripts Alignment to a Reference
TA	Technical assistant
TAE	Tris-acetate-EDTA
TALEN	Transcription activator-like effector nucleases
TCF	Ternary complex factor
TEAB	Triethylammonium bicarbonate
TFA	Trifluoroacetic acid
TGF	Transforming growth factor
TK	Titin kinase
TRA	Transcription regulator analysis
TUNEL	Terminal deoxynucleotidyl transferase dUTP nick end labelling
UPLC	Ultra-Performance Liquid Chromatography
WB	Western blot
WT	Wildtype
YAP	Yes associated protein
ZFN	Zinc finger nucleases

1. Summary

Introduction:

Cardiomyocytes (CM) in the adult mammalian heart lack a regenerative capacity, representing a major barrier to effective repair after injury. One key paradigm, often described as “All work- no repair”, suggests that the constant mechanical (contractile) activity of the heart prevents CMs from re-entering the cell cycle postnatally. While this concept has been described in literature before, direct and reversible experimental systems to test it have been lacking.

Methods:

In this work, I employed the PSAM-GlyR and PSAM4-GlyR chemogenetic tools to transiently inhibit CM contraction electrophysiologically using small molecules, either PSEM^{89S} or varenicline (an FDA-approved anti-smoking drug), respectively. This created a state of contractile silencing without causing irreversible damage. This strategy allowed direct testing of whether inhibition of contraction promotes CM cell cycle activity across multiple experimental systems, two dimensional-cultured CMs, three-dimensional engineered heart tissue, and human adult heart slices. Importantly, this effect was completely reversible upon drug removal. Pharmacological inhibition of contraction was performed using the myosin-ATPase inhibitor mavacamten as a secondary approach to test the hypothesis. Mechanistic insights were further pursued through proteomic and transcriptomic profiling. In addition, a temporal analysis was performed using immunostaining for sarcomeric and cell cycle markers to determine the sequence of events.

Results:

PSAM-GlyR and PSAM4-GlyR CMs either in 2D culture or in EHTs stopped contracting directly after the drug application, and fully recovered after drug washout. Varenicline-treated adult human heart slices transduced with PSAM4-AAV6 dropped in force but did not stop. This transient inhibition of contraction reproducibly induced CM cell cycle re-entry across the different models and revealed concomitant sarcomere disassembly. The effect was linked to contraction itself and not to cardiac excitability as confirmed by the mavacamten experiments. Proteomic and transcriptomic analyses revealed upregulation of cell cycle markers and downregulation of sarcomeric proteins and genes, alongside candidate transcriptional regulators potentially involved in the process. Temporal analysis showed that sarcomere disassembly preceded cell cycle marker expression, suggesting cardiac structural remodelling was a prerequisite for proliferation.

Conclusion:

This work provides direct experimental evidence for the link between workload and proliferative potential in CMs, thereby confirming that cardiac contraction is a physiological regulator of CM cell cycle. By establishing a physiological and reversible model, this study opens the path to mechanistic dissection of workload-regulated cell cycle activity.

2. Zusammenfassung

Einleitung:

Kardiomyozyten (CM) im erwachsenen Säugetierherz besitzen keine regenerative Kapazität und stellen damit ein wesentliches Hindernis für eine effektive Reparatur nach Verletzungen dar. Ein zentrales Paradigma, oft als „All work – no repair“ beschrieben, geht davon aus, dass die kontinuierliche kontraktile Aktivität des Herzen CMs daran hindert, nach der Geburt erneut in den Zellzyklus einzutreten. Obwohl dieses Konzept bereits in der Literatur beschrieben wurde, fehlten bislang direkte und reversible experimentelle Systeme, um es experimentell zu überprüfen.

Methoden:

In dieser Arbeit wurden die chemogenetischen Werkzeuge PSAM-GlyR und PSAM4-GlyR eingesetzt, um die Kontraktilität von CMs transient durch die Applikation der kleinmoluklaren Substanzen PSEM^{89S} bzw. Vareniclin (ein von der FDA und EMA zugelassenes Anti-Raucher-Medikament) elektrophysiologisch zu hemmen. Dies inhibierte die Kontraktilität, ohne irreversible Schäden zu verursachen. Mit dieser Strategie konnte, in mehreren experimentellen Systemen (zweidimensional kultivierte CMs, dreidimensionale künstlich hergestellte Herzmuskelgewebe (EHTs), sowie adulte humane Herzschnitte) direkt untersucht werden, ob Hemmung der Kontraktion die Zellzyklusaktivität von CMs fördert. Der inhibitorische Effekt war, nach Entfernen des Wirkstoffs, vollständig reversibel. Als zweiter Ansatz wurde eine pharmakologische Hemmung der Kontraktilität mittels des Myosin-ATPase-Inhibitors Mavacamten durchgeführt. Mechanistische Einsichten wurden zusätzlich durch proteomische und transkriptomische Analysen gewonnen. Darüber hinaus wurde eine zeitliche Analyse von Sarkomer- und Zellzyklusmarkern durchgeführt, um die Abfolge der Ereignisse zu charakterisieren.

Ergebnisse:

PSAM-GlyR und PSAM4-GlyR-CMs stellten sowohl in 2D-Kultur als auch in EHTs ihre Kontraktionen unmittelbar nach der Wirkstoffapplikation ein, und erholten sich vollständig nach dem Auswaschen. In Varenicline-behandelten adulten humanen Herzschnitten, die mit einem Adeno-assozierten Virus, der PSAM 4-GlyR exprimierte (PSAM4-AAV6) transduziert worden waren, nahm die Kontraktilität ab, kam jedoch nicht vollständig zum Erliegen. Die transiente Hemmung der Kontraktilität führte

reproduzierbar zum Wiedereintritt von CMs in den Zellzyklus, begleitet von einer Sarkomer-Desorganisation. Der Effekt was spezifisch auf die Kontraktilität zurückzuführen und nicht auf eine Manipulation der kardialen Erregbarkeit, wie durch die Mavacamten-Experimente bestätigt wurde. Proteomische und transkriptomische Analysen zeigten eine Hochregulation von Zellzyklusmarkern und eine Herunterregulierung von sarkomerischen Proteinen und Genen, sowie Kandidaten für Transkriptionsregulatoren, die an diesem Prozess beteiligt sein könnten. Die zeitliche Analyse ergab, dass die Dissoziation der Sarkomere der Expression von Zellzyklusmarkern vorausging, was darauf hinweist, dass strukturelles kardiales Remodelling eine Voraussetzung für die Proliferation ist.

Schlussfolgerung:

Diese Arbeit liefert direkte experimentelle Evidenz für den Zusammenhang zwischen Arbeitsbelastung und Proliferationspotenzial von CMs und identifizierte damit, kardiale Kontraktilität als physiologischen Regulator des Zellzyklus. Durch die Etablierung eines physiologischen und reversiblen Modells eröffnet diese Studie den Weg zur mechanistischen Aufklärung der arbeitslastabhängigen Zellzyklusaktivität.

3. Introduction

3.1 Cell cycle and proliferation

In multicellular organisms, cell cycle and proliferation are essential for growth, development, and tissue homeostasis. Cell cycle is the main biological process through which a cell duplicates its genetic material and divides into two daughter cells (Morgan, 2007). In regeneration, the ability of cells to re-enter and complete the cell cycle is critical to determine whether a tissue can recover from injury. Thus, understanding how the cell cycle is regulated, and how it becomes silenced in post-mitotic cells, e.g. cardiomyocytes (CM), is central to the field of regenerative biology (Xu et al., 2025).

3.1.1 Phases of the cell cycle

The eukaryotic cell cycle is traditionally divided into four phases: G1 (gap 1), S (synthesis), G2 (gap 2) and M (mitosis). Cells may also enter a reversible or irreversible quiescent phase known as G0. These phases are regulated by cyclins and cyclin-dependent kinases (CDK) (Nurse, 2000).

3.1.1.1 Interphase

Interphase includes the G1, S, and G2 phases and represents most of the cell cycle. During this period the cell grows, replicates its DNA, and prepares for mitosis. In G1 the cell increases in volume and synthesizes nucleotides, RNA, and proteins essential for DNA replication. It also monitors extracellular signals, such as nutrients and growth factors (Cooper, 2000). Cells that do not receive sufficient mitogenic signals may enter G0, which is common in terminally differentiated tissue (Blomen & Boonstra, 2007). The S phase marks the point of the DNA synthesis, where the entire genome replicates once. This is tightly regulated to prevent replication errors or genomic instabilities that can lead to accumulation of mutations (Laskey et al., 1989). Next is the G2 phase that allows the cell to complete its preparation for division. It includes the synthesis of chromosome segregation proteins such as tubulin and spindle fibre precursors. DNA integrity is examined for signs of damage. From there on, G2/M checkpoint takes place to ensure that replication is accurate (Nasmyth, 1996).

3.1.1.2 Mitotic phase

Although the mitotic (M) phase is the shortest phase, it is visually quite dynamic (Walczak et al., 2010). It is divided into four phases as well: prophase, metaphase, anaphase, and telophase. In the *prophase*, condensation of chromatin takes place and chromosomes become visible. In this phase the mitotic spindle begins to assemble, and the centrosomes move to the poles of the cell (Cooper, 2000). An intermediate step between the prophase and the metaphase is often called prometaphase. Here the nuclear envelope breaks open and the spindle microtubules connect to kinetochores at the centromeres (Verdaasdonk & Bloom, 2011).

When the chromosomes align along the equator of the cell it is then called the *metaphase*. The chromosomes are equidistantly placed from each cell pole by the help of the spindle assembly which verifies that the chromosomes are correctly attached. The *anaphase* follows where the microtubules shorten. Thus, the chromatids retract and separate to the opposite poles. Last phase is the *telophase* which is known for the reformation of the nuclear envelope around the newly formed chromosomes sets, which begin to decondense again. Finally cytokinesis takes place by partitioning the cytoplasm and producing two genetically identical daughter cells (Morgan, 2007).

3.1.1.3 Quiescence (G0) phase

The G0 phase is the state where the cells are metabolically active but not dividing. This phase is essential for cells that need to be constantly functioning like CM and neurons (Ahuja et al., 2007). While some cells re-enter the cell cycle from G0 in response to injury or growth factors, others remain permanently post-mitotic. This quiescent state is controlled by cytokines and signals that regulate the cell fate -~~;~~ to divide, differentiate or rest (Crescenzi, 2002).

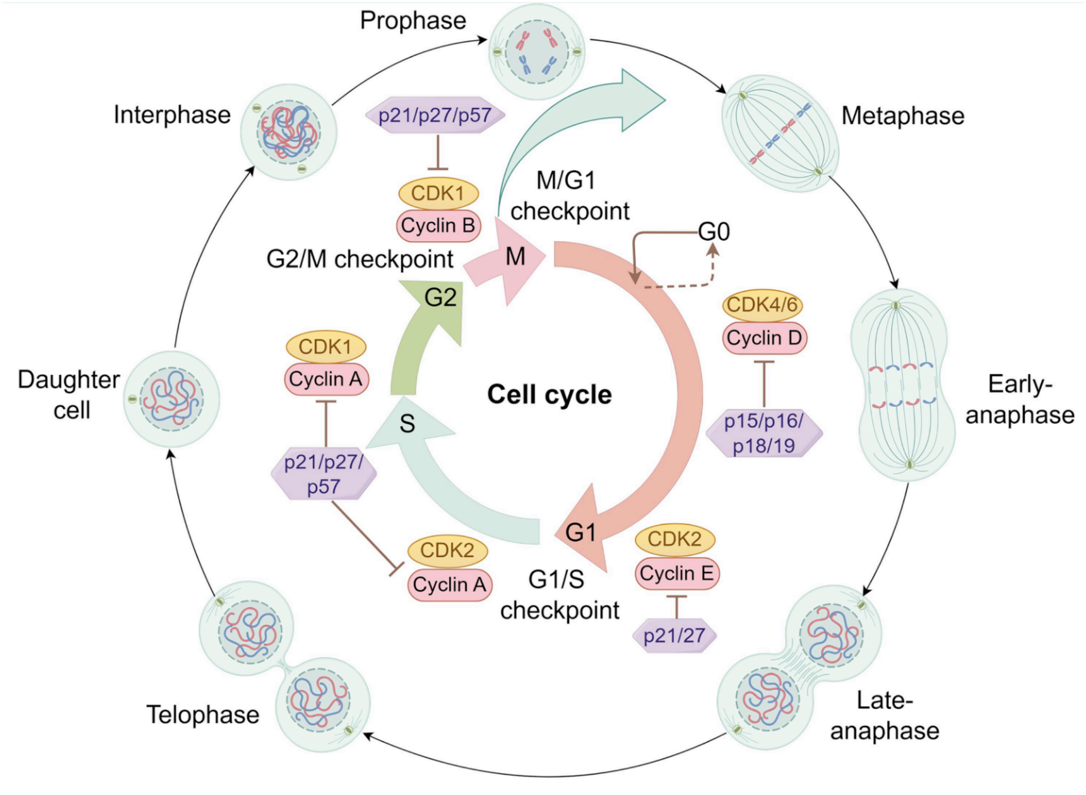

Figure 3.1 Eukaryotes cell cycle, activators, and inhibitors adapted from (Xu et al., 2025).

3.1.2 Cell cycle regulatory mechanisms

The cell cycle is a highly orchestrated process regulated by a complex network of proteins; primarily cyclins and CDKs. Moreover, there are checkpoints, inhibitors and extracellular signals that control the cell cycle progression and ensure its completion or arrest.

3.1.2.1 Cyclins and cyclin-dependant kinases

CDKs are serine/threonine kinases that need to bind to cyclins for activation. There are more than 20 members of the CDK family, however only a certain subset of CDK-cyclin complexes is directly involved in the cell cycle. These cyclin-CDK complexes are expressed in regular intervals to ensure unidirectional cell cycle progression (Malumbres & Barbacid, 2009). In G1, cyclin D binds to CDK4/6, which initiates phosphorylation of the retinoblastoma proteins (Rb). Rb releases E2F transcription factors that drive S-phase gene expression. Cyclin E/CDK2 pushes this process further at the G1/S transition. During the S phase, cyclin A/CDK2 supports DNA replication. Followed by G2/M where cyclin B/CDK1 is essential for entry into mitosis. These complexes are regulated through multiple mechanisms including phosphorylation, dephosphorylation, trans-localization, and degradation by ubiquitination (Gérard & Goldbeter, 2012).

3.1.2.2 CDK inhibitors

There are two families of CKIs: the INK4 family and the CIP/KIP family. INK4 family consists of p15, p16, p18 and p19 which inhibit CDK4/6 and accordingly block G1 phase. The CIP/KIP family consists of p21, p27, and p57, which can inhibit several cyclin/CDK complexes (Lim & Kaldis, 2013). CKIs act as brakes on the cell cycle in response to differentiation signals, contact inhibition and genotoxic stress like DNA damage.

3.1.2.3 Cell cycle checkpoints

There are three main checkpoints that act like quality control mechanisms: the *G1/S* checkpoint checks DNA integrity and the cellular environment, the *G2/M* checkpoint ensures DNA replication is achieved properly, and the *spindle assembly checkpoint (SAC)* verifies proper chromosome alignment and attachment to the spindles (Kastan & Bartek, 2004). These checkpoints depend on the activation of certain kinases such as CHK1 and CHK2. These kinases trigger downstream effects if the DNA is damaged and lead to cell cycle arrest through stabilization of p53, a known tumour suppressor gene because it inhibits cell cycle, and induction of CDK inhibitors (CKI) such as p21 (Lim & Kaldis, 2013).

3.1.2.4 Transcriptional and post translational regulation

Cell cycle progression is controlled at multiple levels, including transcriptional programs and post-transcriptional modification that control the timely expression and activation of the cell cycle regulators. I will focus on YAP1, SRF, E2F, PI3K-Akt and FOXM1, which are directly relevant to the results I obtained in this project.

Yes-associated protein 1, YAP1, a key effector of the Hippo signalling pathway that has been widely reported to regulate cardiomyocyte proliferation during developmental and early postnatal stages. When Hippo signalling is inactive, YAP1 translocates to the nucleus and co-activates TEAD transcription factors to promote the expression of genes involved in cell proliferation and survival (Heallen et al., 2013; Xin et al., 2013). In the heart, YAP1 is highly active during embryonic and neonatal stages, supporting the proliferative capacity of the CM, and YAP inactivation coincides with the postnatal decline in regenerative potential (von Gise et al., 2012). Overexpression or activation of YAP1 in postnatal and adult models has been shown to restore cell cycle activity (Monroe et al., 2019; Moya & Halder, 2018; Xin et al., 2013).

Serum response factor, SRF, is a widely expressed transcription factor that binds to serum response elements (SRE) in the promotor regions of muscle-specific genes (Soulez et al., 1996). In CMs, SRF plays a fundamental role in cytoskeletal organization, sarcomere assembly, and contractile function (Balza & Misra, 2006). SRF activity is tightly coupled to actin dynamics: changes in the G-/F-Actin ratio modulate the availability of its cofactors, myocardin-related transcription factors (MRTF). This influences SRF-dependent transcription by determining whether SRF will bind to MRTF or ternary complex factor (TCF) (Gualdrini et al., 2016). During development, SRF supports the expression of structural and contractile proteins required for CMs maturation, where as its downregulation or functional impairment has been associated with sarcomere disassembly, reduced contractility, and shift towards a less mature cardiac phenotype (Guo et al., 2021).

E2F proteins play a role in controlling the expression of genes involved in the DNA synthesis and the progression of the cell cycle, especially in G1/S phase (Morgan, 2007). During cell cycle arrest Rb is unphosphorylated and bound to E2F, which prevents E2F from binding to cyclin E gene. With the help of cyclin D-CDK4/6 complex Rb is hyperphosphorylated and releases E2F which drives transcription of genes that are essential for cell cycle progression and DNA replication (Pellarin et al., 2025). Furthermore, the E2F family is composed of both activators (E2F1-3a) and repressors (E2F3b-8) isoforms. Activators promote proliferation while repressors facilitate cell cycle exit and enforce G0 (Morgan, 2007).

The neuregulin-1 (NRG1) – ERBB2 signalling pathway is a pivotal regulator of cell proliferation, survival, and differentiation. NRG1, a member of the epidermal growth factor (EGF) family, binds primarily ERBB3/4, a member of epidermal growth factor receptors, which subsequently heterodimerize with ERBB2, a receptor tyrosine kinase that lacks a direct ligand (Holbro et al., 2003; Pinkas-Kramarski et al., 1996). Activation of ERBB2-containing receptor complexes initiate downstream signalling cascades such as PI3K-Akt-mTOR and RAS-RAF-MEK-ERK pathways, which are crucial drivers of cell proliferation (Citri & Yarden, 2006). Dysregulation of ERBB2-NRG1 signalling is strongly implicated in oncogenesis, as ERBB2 amplification promotes uncontrolled proliferation and tumour progression in several cancers (Moasser, 2007; Slamon et al., 1987).

Forkhead box M1 also known as FoxM1 is another transcription factor required for proper mitotic entry and progression. It is mainly expressed in proliferating cells and is induced during the late G1 phase, with peak activity observed in S and G2/M phases (Wierstra, 2013). FoxM1 directly activates transcription of a broad array of mitosis-related genes, including cyclin B1, PLK1, CENPF, Aurora A, and Survivin (Laoukili et al., 2005). Without FoxM1 cells exhibit impaired spindle formation and chromosomal instability. In cardiovascular research, FoxM1 has attracted interest for its role in promoting cardiomyocyte proliferation. Transient activation of FoxM1 in neonatal mouse hearts enhanced CM mitosis and supported myocardial regeneration after injury (Zuppo et al., 2023).

While the cell cycle framework is universal across somatic cells, CMs deviate from this model, as their ability to progress through the cell cycle becomes profoundly restricted after birth.

3.2 Factors influencing cardiac regeneration

The adult human heart lacks a relevant CM proliferative capacity (Bergmann et al., 2009). This creates a challenge as after myocardial infarction, the heart irreversibly loses up to 1 billion CM, which leads to scar formation and eventually heart failure (Laflamme & Murry, 2005). Similarly, long lasting hypertension or structural heart disease results in a loss of CM (Liu et al., 2000; Olivetti et al., 1991). Ischemic heart disease and stroke alone account for over 18 million death yearly (Roth et al., 2020). Leading to the fact that cardiovascular diseases (CVDs) remain the major cause of death globally. Subsequently, 45% of all deaths in Europe are due to CVDs, which exerts a huge toll clinically and economically (Townsend et al., 2022). Although numerous advances in prevention and therapy have improved life expectancy for patients suffering from CVD, the main challenge persists: the majority of adult CMs do not proliferate.

While zebrafish have proliferative potential for life and can recover from cardiac injury (Jopling et al., 2010; Poss et al., 2002), adult rodent and human CM rarely re-enter the cell cycle, and even when they do, cytokinesis often fails (Derks et al., 2025). Experimental models of apical resection and myocardial infarction demonstrated complete regeneration in mice within the first postnatal week, followed by a shift toward fibrotic scarring (Porrello et al., 2011). A regenerative window has also been described in pigs (Ye et al., 2018; W. Zhu et al., 2018) and there is anecdotal evidence that it might also exist in humans (Gur et al., 2025; Haubner et al., 2016). Yet CM exit the cell cycle early after birth and an irreversible loss of CM takes place in the adult heart without a chance to replace the lost CM with new daughter cells. Studies confirm that basal cell cycle activity in adult mammalian CM are insufficient to repair the heart (Bergmann et al., 2009; Senyo et al., 2013; Soonpaa et al., 1996).

In this chapter I will take a deeper look into the adult CM features that might lead to their cell cycle arrest.

3.2.1 Polyploidy and multinucleation

Neonatal CM are known to have a robust proliferative capacity, as they grow extensively in the womb and can regenerate even after injury (Hesse et al., 2018; Lam & Sadek, 2018). This capacity is lost after birth coinciding with nuclear changes, namely binucleation and polyploidization (Soonpaa et al., 1996). In mice, pulse-chase labelling with thymidine analogues and nuclear staining revealed that over 90% of adult murine CM become binucleated by postnatal day 14 (Velayutham et al., 2019). in humans, histological and flow cytometry analysis show that binucleation rarely exceeds 20%, but flow-based karyotyping demonstrated that polyploidy increased markedly within the first year of life (Derks et al., 2025; Mollova et al., 2013). Polyploid nuclei exhibit abnormal chromosome segregation during mitosis and do not proceed to the following phase. These defects resulted in unequal DNA distribution and mitotic failure (Derks & Bergmann, 2020). Adult CM display lack of proliferation in parallel to increased polyploidization and multi-nucleation. To test whether polyploidy itself directly restricts proliferation in CMs, Patterson et al. employed mice with floxed Tnni3k, a gene responsible for the number of mononuclear diploid CMs (MNDCMs). After Tnni3K deletion in CM, it was shown that reducing polyploidization by promoting MNDCM generation restored clean chromosome segregation and cell division. This identified ploidy itself as the root cause of cell cycle arrest rather than secondary factor (Patterson et al., 2017). In zebrafish, forced polyploidization of CM through inducible cytokinesis inhibition was sufficient to abolish the hearts regenerative capacity, although the remaining diploid cells remained capable of proliferation (González-Rosa et al., 2018). In Shen et al, it was demonstrated that insulin-like growth factor-2 (IGF2) dependent regeneration requires a high number of MNDCMs. Using a hypoxia mCAT A/J mouse strain, engineered with mitochondrial catalase which reduces oxidative stress and preserved more MNDCMs, showed that MNDCMs abundance can rescue the regenerative capacity even in the absence of IGF-2 (Shen et al., 2020). However, a central debate in the field of cardiac regeneration remains: Does the regenerative potential of CMs arise predominantly from the small population of MNDCMs or are there other sources? For instance, although approximately 70% of human neonatal CM are MNDCMs, human infants typically fail to regenerate after myocardial injury, suggesting that MNDCMs alone may not be sufficient to enable regeneration (Kirillova et al., 2021). Also experiments in which the abundance of MNDCMs was increased by genetic manipulation, namely deletion of E2F7/8, did not yield improved regenerative outcomes (Z. Yu et al., 2023). Other perspectives stated that while MNDCM may indeed show a higher proliferative capacity than their polyploid or multinucleated counter parts, this alone is insufficient to drive meaningful regeneration in the adult mammalian heart, unlike in zebrafish or neonatal mice (Ding & Braun, 2023; Mehdipour et al., 2023).

3.2.2 Cytoskeletal and extracellular factors

During fetal and early postnatal development, CMs possess a relatively loose and plastic contractile apparatus, where the sarcomeres are shorter, less aligned, and continuously remodelled to accommodate both growth and division (F. Li et al., 1996). As the CM mature, their sarcomere architecture becomes more ordered and stable when compared to neonatal CMs (Siedner et al., 2003). The myofibrillar network expands longitudinally and laterally, Z-lines become well-aligned and sarcomere length increases to approximately 2.2 µm (Guo & Pu, 2020) to support the required force generation (Lundy et al., 2013; Sheikh et al., 2015). During mitosis, sarcomeres undergo stepwise disassembly starting with the Z-disc proteins followed by M- and A-band components, accompanied by transient inhibition of contraction (Ahuja et al., 2004; Fan et al., 2015). This was confirmed in induced proliferation experiments, where the adult CMs often display dedifferentiation-like states and the sarcomere disassemble temporarily until the end of mitosis (Kubin et al., 2011; Xiao et al., 2024; Yuan et al., 2022).

Another important factor is the extra-cellular matrix (ECM). Cardiac ECM in neonates is enriched in ECM proteins such as collagen, fibronectin, and periostin (Marijianowski et al., 1994; Williams et al., 2014). During cardiac maturation, the composition and mechanical properties of the ECM changes substantially (Robinson & Kinne, 1990). After birth, there is a marked decrease in some ECM protein abundance, and change in type or ratio, leading to an increase in ECM stiffness which coincides with their cell cycle exit (Borg et al., 1984). Several studies were done an attempt to understand the correlation between ECM stiffness and cell cycle exit. After myocardial infarction in adult mice, decellularized neonatal mouse ECM were injected into the infarcted regions. This intervention showed a significantly improved heart function and limited post injury remodelling when compared to adult derived ECM (Z. Wang et al., 2019). Moreover, it was observed that neonatal CMs that were cultured on soft compliant matrix exhibited dedifferentiation, sarcomeric disassembly, and mitotic activity. In contrast, stiffer substrate promoted cytoskeletal alignment and resulted in cell cycle arrest and binucleation (Yahalom-Ronen et al., 2015). Agrin, an ECM protein that is abundant prenatally and markedly decreases after birth, showed elevation in CMs proliferation when administered to adult mice CM after injury, through YAP/ERK signalling (Bassat et al., 2017). In another approach, it was shown that primary neonatal rat CM exposed to ECM derived from postnatal fibroblasts exhibited higher rates of binucleation compared to those grown on ECM from embryonic fibroblasts (C.-C. Wu et al., 2020). Finally, using rat EHTs, Ciucci et al. demonstrated that postnatal ECM remodelling- particularly increased stiffness and altered protein composition- restricts contractile plasticity and regenerative responses (Ciucci et al., 2023).

Recent work highlights N-Cadherin`s (Cdh2; a cell-cell junction stabilizer) role as a mediator of CM proliferation, partially through stabilization of the β-catenin pathway. In this study, Cdh2 expression was found to be high in neonatal mice CMs and decreasing with CM maturation and cell cycle arrest. Loss of function experiments demonstrate impaired regeneration in neonatal mice, while Cdh2 overexpression in hiPSC-CM enhanced proliferative activity. Cdh2 was shown to bind directly to β-catenin, promoting downstream transcription of mitotic genes (Tsai et al., 2025).

On top of that, mature CM become more hypertrophic, i.e. they show an increase in cell diameter and anisotropy, which limits their ability to achieve mitotic rounding (Cluzeaut & Maurer-Schultze, 1986). Mitotic rounding has been repeatedly identified as a prerequisite for accurate chromosome segregation (Morikawa et al., 2025; Yahalom-Ronen et al., 2015). Together, these findings reveal that ECM composition and mechanism are critical determinants of CMs proliferative potential.

3.2.3 High metabolic demand

During fetal development, the heart operates in a relatively hypoxic condition. Gas exchange occurs via the placenta and blood is shunted away from the (not ventilated) lungs through the ductus arteriosus and foramen ovale (Rudolph & Heymann, 1969). This results in relatively low arterial oxygen tension, where anaerobic respiration predominates as the source of ATP production (Fisher et al., 1980; Lopaschuk et al., 2010). A few days after birth, CM metabolism shifts from glycolysis to oxidative phosphorylation (OxPhos) due to the cut off of the placental and the increased oxygen availability (Lopaschuk et al., 1992; Piquereau & Ventura-Clapier, 2018). Consequently the cardiac-specific mitochondrial biogenesis, size, and cristae organization increase, spreading throughout the cell to provide adequate amount of ATP needed by the mature CM (Hom et al., 2011). The metabolic shift after birth derived by the increased biomechanical workload is accompanied by transcriptional remodeling involving Peroxisome Proliferator-Activator Receptor alpha (PPARα) and Peroxisome Proliferator-Activated Receptor Gamma Coactivator 1-alpha (PGC-1α) (Lopaschuk et al., 2010). A recent study demonstrated that in neonatal rat CMs, activation of PPARα with a pharmacological agonist (WY-14643) increased cell cycle activity while reducing cell size. This suggested that PPARα activation can promote proliferation (Xuan et al., 2025).

After birth, the mitochondria undergo significant expansion in CMs. A direct consequence of mitochondrial expansion is the increase in reactive oxygen species (ROS), leading to the activation of DNA damage response (DDR) pathway (Puente et al., 2014). One of the activated DDR pathways is the ATM/ATR signaling pathway that stabilizes p53 and induces CDK inhibitors such as p21 and p27, both affecting the G1/S checkpoint leading to cell cycle arrest. Pharmacological and genetic interventions that aimed to reduce mitochondrial ROS, e.g. overexpression of antioxidant enzymes, partially prolonged the proliferative capacity of neonatal CM (Puente et al., 2014).

In another attempt to recover the neonatal proliferative capacity in hiPSC-CM, the culture medium was supplemented with high glucose concentration. As a result, CM cell cycle markers were elevated, while CM maturation was suppressed. These findings were derived by increased nucleotide biosynthesis via the pentose phosphate pathway as detected from the metabolic analysis (Nakano et al., 2017).

3.2.4 Postnatal workload

In utero, the mammalian heart operates within a low-resistance circulation, supported by placental gas exchange and shunted blood flow that minimize ventricular afterload (Remien & Majmundar, 2025). At birth, the loss of placental perfusion and the initiation of pulmonary respiration abruptly increases systemic vascular resistance and left ventricular pressure. Thus, the neonatal heart experiences increase in wall stress and contractile demand within hours after birth (Harvey, 2002).

This dramatic shift imposes substantial mechanical and metabolic demands on CM, requiring structural remodelling that favours hypertrophic over hyperplastic growth (Ahuja et al., 2004). To meet these demands, CM undergo dramatic growth adaptations including mechanosensitive pathways such as integrin signalling, MAPK cascade and calcineurin-NFAT activation, leading to the addition of sarcomeres in series and parallel increasing CM size and wall thickness (Remien & Majmundar, 2025). Studies in rodent models showed that neonatal CMs rapidly enlarged after birth, doubling in volume within the first week (Velayutham et al., 2019). This early hypertrophy coincides with binucleation and polyploidization, together favouring cell cycle arrest.

Evidence that contraction is linked to cell cycle comes from patient samples. Patients with advanced heart conditions such as dilated cardiomyopathy, ischemic cardiomyopathy or end-stage heart failure often receive left ventricular assisting device (LVAD) to mechanically unload the ventricles and reduce myocardial workload

(Kayali et al., 2024). Interestingly, several studies have reported that hearts of the subfraction of patients that showed improved contractile function after LVAD-induced reduction in workload (“responders”) had higher cell cycle activity and proliferation (Canseco et al., 2015; Derks et al., 2025), highlighting the effect of the workload on cardiac cell cycle arrest.

3.2.5 Genetic and epigenetic regulators

The permanent CM cycle arrest in the early postnatal period is not an isolated event, but the result of several coordinated genetic and epigenetic reprogramming events. This transition involves several transcriptional changes, chromatin remodelling, and activation or inhibition of different signalling pathways (Cui et al., 2018).

3.2.5.1 Transcription regulators

During embryonic development, cyclins, CDK and E2F transcription factors are highly active leading to robust proliferation (Ahuja et al., 2007). Soon after birth, the expression of these regulators sharply decreases while the expression of cell cycle inhibitors such as p21, p27 and p57 that block the cell cycle at every checkpoint (Patterson et al., 2017) increases. This switch is coupled to the activation of the retinoblastoma (Rb)/E2F axis, that leads to hypo-phosphorylated Rb blocking E2F-driven mitotic genes (Secco & Giacca, 2023). Cyclin A2, D2 and E2F2 overexpression in different experimental setups led to the cell cycle re-entry and increased proliferation in CM (Busk et al., 2005; Chaudhry et al., 2004; Ebelt et al., 2008). Another factor that enforces cell cycle exit was the thyroid hormone T3 that activated p38-MAPK (Hirose et al., 2019). p38-MAPK activation phosphorylated and inhibited CDK1/2 as well as stabilizing CDK inhibitors like p16INK4a. This pathway is amplified by oxidative stress in the aging heart, creating a feedback loop that in turn worsens cell cycle arrest (Lim & Kaldis, 2013; Sadek & Olson, 2020).

Developmental regulators also play a crucial role in supressing mitosis in mature CM. GATA4, MEF2, and NKX2.5 which are key cardiac transcription factors that have opposing roles pre- and postnatally. During embryonic development they induce cardiac morphogenesis and proliferation while postnatally they lead to the activation of maturation programs rather than cell cycle genes (Padula et al., 2021; Schlesinger et al., 2011). For instance, Mef2a and Mef2c initially associated with myocyte proliferation, later become essential for the expression of structural genes like MYH6 and ACTC1 (Black & Olson, 1998).

These contrasting roles resemble the transcription factors discussed in the previous chapter – such as YAP1, SRF, E2F, PI3K-Akt and FOXM1 - which undergo profound changes during the transition from fetal to adult CMs. As CMs exit the proliferative window, the expression and activity of these transcriptional programs are markedly downregulated, contributing to a stable cell cycle arrest. The following figure illustrates how these regulators interact within a coordinated network to promote proliferation.

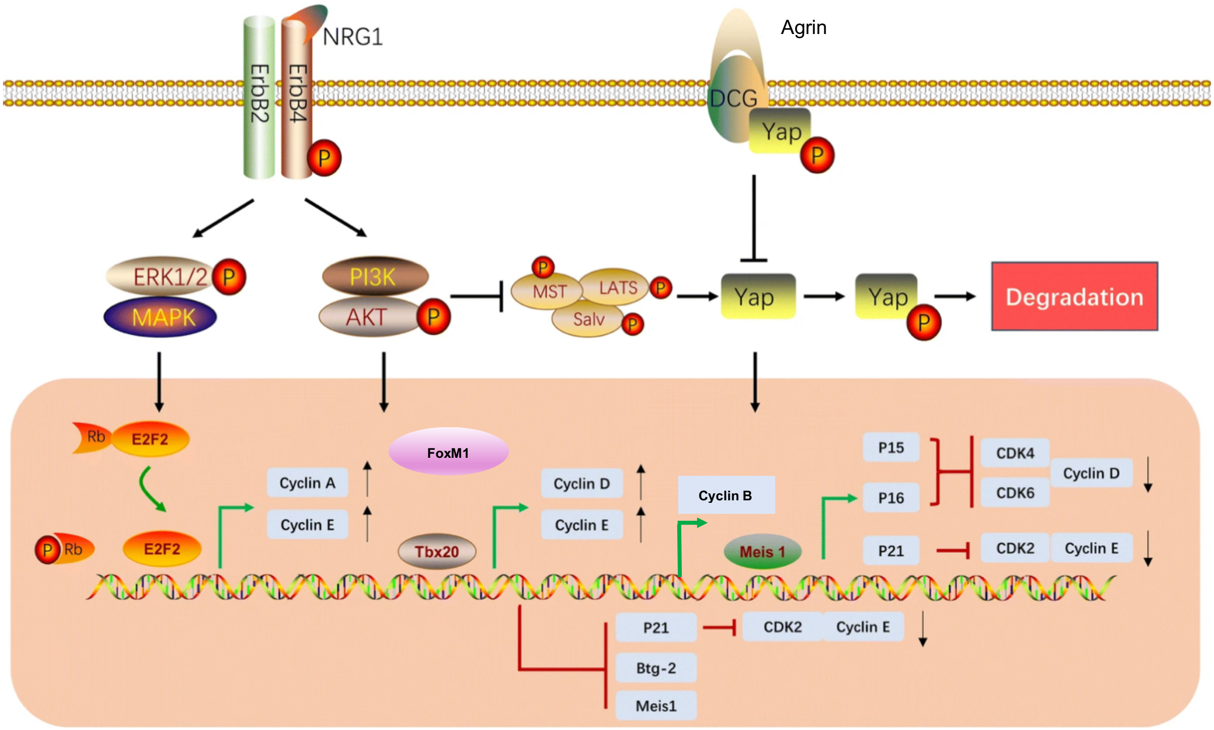

Figure 3.2 Proliferation and cell cycle regulators

An overview representing several molecular signaling pathway, illustrating cardiac cell cycle regulation through transcription factors, and epigenetic regulators, adapted from (F. Zhu et al., 2021).

3.2.5.2 Epigenetic regulators

Epigenetic mechanisms play a role in stabilizing the CM non-proliferative state. Genome-wide analyses demonstrated that during early postnatal maturation, chromatin accessibility at promoters and enhancers of cell cycle genes decreased. One mechanism is through histone modification shifts, activating histone marks H3K27ac and H3K4me3 and supressing H3K27me3 and H3K9me3, that is largely mediated by Polycomb complex, locking the CM in post-mitotic state (Cui et al., 2018; Wamstad et al., 2012).

DNA methylation patterns also shift, stabilizing mitotic loci silencing, while enhancing expression of contractile and metabolic genes (Padula et al., 2021). ChIP sequencing was mapped across cardiac lineage stages and revealed that the active enhancers during early development become neutralized and new enhancers got activated leading to hypertrophic growth and oxidative programs (Wamstad et al., 2012).

Having established that CM progressively lose their proliferative capacity as they mature, the next step is to examine the physiology of the adult CM in details, as it may provide a critical insight into the relationship between their functional role and the accompanying arrest of the cell cycle.

3.3 Physiology of cardiomyocytes

CM are highly specialized in their structures, electrical properties, and metabolic demands. Their physiology has to match their need for coordinated contractions and relaxation in over billions of cycles during human lifetime. Another feature of the CM physiology is the capability to adapt to developmental and mechanical signals (Guo & Pu, 2020). This is tightly linked to their post mitotic nature and limited regenerative capacity. Understanding CM physiology provides essential context for explaining their restricted proliferative capacity and might provide means to reactivate their regenerative capacity.

3.3.1 Sarcomere structure

The contractile machinery of CM is defined by the sarcomere, the motor unit of striated muscles. Sarcomeres are composed of precisely aligned thin (actin) and thick (myosin) filaments (Bárány, 1967). Overlapping myosin filaments with actin form A-bands, while I-bands only contain actin. Myosin serves as the motor protein responsible for active force generation in CM (Sweeney & Holzbaur, 2018). It is composed of myosin heavy chain -mainly MYH7 in adult CM and MYH6 in fetal CM-, along with myosin light chain (MLCs), where the atrial isoform MLC2a is dominant in fetal CM and the ventricular isoform MYL2 predominates in adult CM (Karbassi et al., 2020; Sheikh et al., 2015). Its main function is to hydrolyze ATP to generate force through cyclic interaction with actin (Walklate et al., 2016). The thin filament is composed of α-cardiac actin (ACTC1), associated with regulatory proteins such as tropomyosin, and troponin complexes (Potter & Gergely, 1975). The globular actin (g-actin) is the monomer soluble form that forms filamentous actin (f-actin) by polymerization (Severs, 2000). It functions as track for myosin cross-bridge cycling during contraction. It also contributes to sarcomere integrity, connecting the cell cortex and costameres. Costameres are specialized structure complexes in muscle cells that physically link the sarcomeres to the sarcolemma (the cardiomyocyte membrane). The central H-zone contains only myosin and is bordered by the M-line, a dense region composed mainly of myomesin, M-protein and obscurin and serves as an anchor site to the myosin filaments (Boron and Boulpaep 2020). Each sarcomere is limited by Z-discs, a dense, fibrous structure that is composed primarily of α-actinin. Titin, the largest known protein in the human body, spans half the sarcomere from the Z-disc to the M-line. Titin is composed of multiple subunits and acts as a molecular spring in the sarcomere. It plays a crucial role in the passive elasticity, mechano-transduction, and sarcomere alignment. Mutations in the titin gene are a major cause of dilated cardiomyopathy. This highlights the importance of titin in maintaining the sarcomere integrity specially under mechanical stress (Squire, 1997).

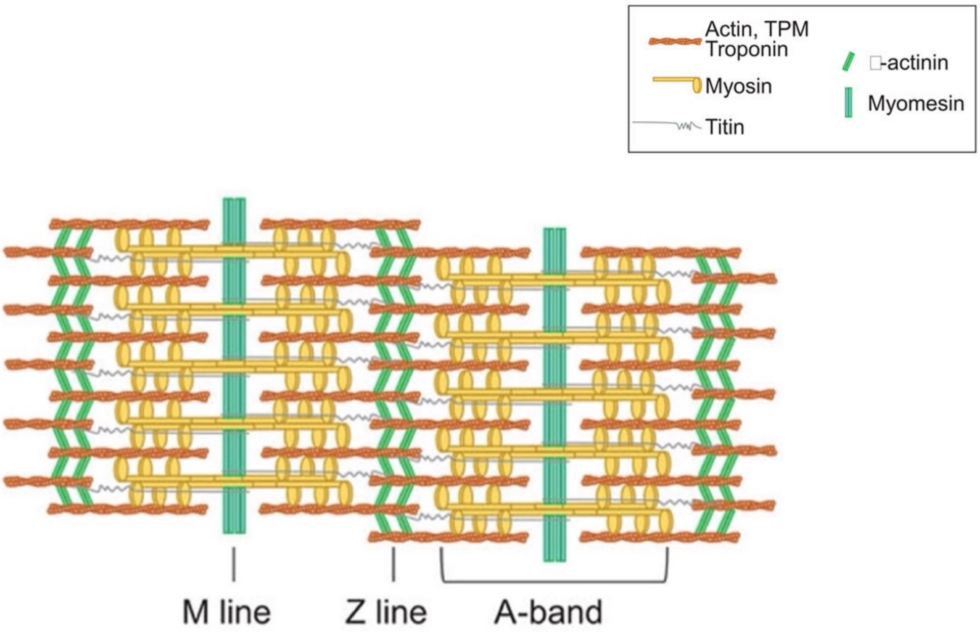

Figure 3.3 Sarcomere structure adapted from (Guo & Pu, 2020).

3.3.2 Intercalated discs and cell-cell contact

CM electrically and mechanically couple through the intercalated discs. These are highly specialized cell-cell junctions that are formed at the longitudinal ends of the CM. They are composed of three types of junctions: desmosomes, adherens junctions and gap junctions. Desmosomes act as anchors of the CM that stabilize the cytoskeleton under high stress by linking desmoplakin and plakoglobin to the intermediate filaments such as desmin. On the other hand, adherens junctions, composed of N-cadherin and β-catenin, connect the actin cytoskeleton between adjacent cells to coordinate mechanical contraction. Lastly gap junctions, which mainly consists of connexin 43 (Cx43), facilitate the passage of ions and second messengers between neighboring CM, thus ensuring electrical and mechanical conduction (Ali et al., 2020; Boron & Boulpaep, 2020; Severs, 2000).

3.3.3 ECM and cytoskeletal network

The internal cytoskeleton is essential for the transmission of sarcomeric contraction to the cell membrane, and further to the surrounding ECM. Costameres, dystrophin, and spectrin are the proteins that anchor the sarcomere to the sarcolemma at the Z-discs. This provides mechanical continuity between internal force generation and ECM (Ali et al., 2020).

These structures serve as mechanical anchors and more importantly as mechano-transducers, converting mechanical changes into intracellular signals. Under physiological conditions, mechanical stress is transmitted through costameres, and focal adhesion sites can activate signaling pathways like MAPK/ERK, PI3K/Akt, and Hippo/YAP. These pathways are known to regulate gene expression profiles related to growth, proliferation, survival and cytoskeletal organization (Martino et al., 2018).
Here I will be highlighting on YAP/TAZ for their central role in the project. YAP and TAZ are transcriptional co-activators downstream of the Hippo signaling pathway and are essential for regulating CM structure and growth (Heallen et al., 2013). They control the transcription of genes encoding sarcomeric and junctional proteins (Morikawa et al., 2015). If Hippo signaling is active, YAP/TAZ remain in their phosphorylated state in the cytoplasm unable to cross the nuclear membrane for any transcriptional function. When the Hippo signaling is off, YAP/TAZ are dephosphorylated and translocate from the cytoplasm to the nucleus to upregulate

structure genes, e.g. focal adhesion (N.-G. Kim & Gumbiner, 2015). As cytoskeletal tension and sarcomere assembly are perturbed, YAP/TAZ localize into the nucleus and modulate the downstream transcriptional program, stabilizing sarcomere organization and cell-cell junction to restore the mechanical balance (Morikawa et al., 2017). This mechano-transduction feedback ensures that CMs continuously adapt their contractile apparatus and intercalated disc composition to workload demand. In postnatal mice, conditional activation of ROCK2 in a gain-of-functional mouse model increased actomyosin contractility and promoted $\alpha5/\beta1$ integrin engagement and fibronectin matrix assembly. These mechanical changes drive YAP/TAZ nuclear translocation and in this model, nuclear YAP is associated with upregulation of transcriptional programs that include both structural/adhesion genes and cell cycle-promoting genes, leading to the increase of CM cell cycle activity (X. Li et al., 2023).

3.3.4 Cardiomyocytes maturation

3.3.4.1 Structural maturation

CM undergo significant maturation after birth. In fetal CM, sarcomeres are shorter and less aligned, intercalated discs are poorly developed, accordingly the gap junctions are distributed throughout the whole cell membrane and not polarized to the intercalated discs as in adult CM (Guo & Pu, 2020). After birth, sarcomeres elongate and align along the longitudinal axis, intercalated discs merge at the cell terminal and gap junctions form end-to-end connections (Vreeker et al., 2014). In vitro, iPSC-CM lack this level of structural maturation. Even after weeks in culture, they show limited sarcomere organization, fewer mitochondria, and weak integration with ECM components (Weinberger et al., 2017). Mechanical stimulation and 3D tissue culture have shown to improve sarcomeric assembly, and contractile function but full adult-like morphology remains unachievable. This presents a challenge in regenerative approaches as the structural immaturity limits force generation and leads to inefficient excitation contraction coupling (ECC) thus generates arrhythmogenic behavior (Dhahri et al., 2022).

3.3.4.2 Metabolic maturation

CM have the highest energetic demands of any cell type. They require continuous and abundant supply of ATP to fuel contraction, calcium cycling and ionic gradients. The adult heart gets approximately 70% of its ATP from fatty acid oxidation, while the rest comes from glycolysis and lactate metabolism. Mitochondria occupy over 30% of the CM volume, forming dense networks aligned with myofibrils to ensure efficient ATP delivery (Lopaschuk et al., 2010). Moreover, the metabolic features of the CM changes from fetal to postnatal states. During fetal development, CM rely on anaerobic glycolysis due to the low oxygen environment of the uterus. After birth, a dramatic shift takes place towards oxidative phosphorylation. This transition is essential for supporting the energetic demands of the contracting mature CM (Kennedy-Lydon & Rosenthal, 2017). However, it imposes a barrier to proliferation, since such high oxidative metabolism can generate high reactive oxygen species levels, which in turn leads to the inhibition of the cell cycle (Lopaschuk et al., 2010).

3.3.5 Cardiac electrophysiology

Electrophysiology is a unique feature of CM, confirming their ability to contract regularly and propagate action potential throughout the myocardium. Such precise electrical signaling in the heart enables coordinated contraction and ensures effective blood pumping (Louch et al., 2010).

3.3.5.1 Cardiac action potential

There are 2 main types of action potentials (AP) in the heart, pacemaker AP generated by pacemaker cells and ventricular AP. Pacemaker AP are characterized by a slow diastolic depolarization phase via the hyperpolarization-activated cyclic nucleotide-gated (HCN) channels carrying funny current (I_f). These cells lack a resting membrane potential and instead they show spontaneous diastolic depolarization, which enables them to generate electrical activity in the heart, followed by the ventricular AP. As for the ventricular AP, they are different from those in the neurons or skeletal muscles, as they are characterized by a prolonged plateau phase that ensures sufficient time for calcium influx and contraction (Bers, 2002).

Ventricular action potential consists of 5 distinct phases (Phases 0-4) (Shih, 1994).

- ◊ Phase 0: **depolarization** phase, characterized by rapid upstroke driven by sudden sodium current (I_{Na}) influx via opened voltage gated sodium channels (Nav1.5; SCN5A).
- ◊ Phase 1: **early repolarization** phase, characterized by a transient brief potassium current (I_{to}) efflux, mediated by Kv4.2/4.3 potassium channels.

◊ Phase 2: **plateau** phase, characterized by the prolonged plateau resulting from a balance between influx of L-type calcium current via Cav1.2 channels and delayed rectifier potassium current.

◊ Phase 3: **repolarization** phase, characterized by dominating potassium efflux (I_{Kr} and I_{Ks}, mediated by hERG and KCNQ1, respectively).

◊ Phase 4: **resting** phase, characterized by maintained inward K^+ current (I_{K1}, via Kir2.1) and Na^+/K^+-ATPase.

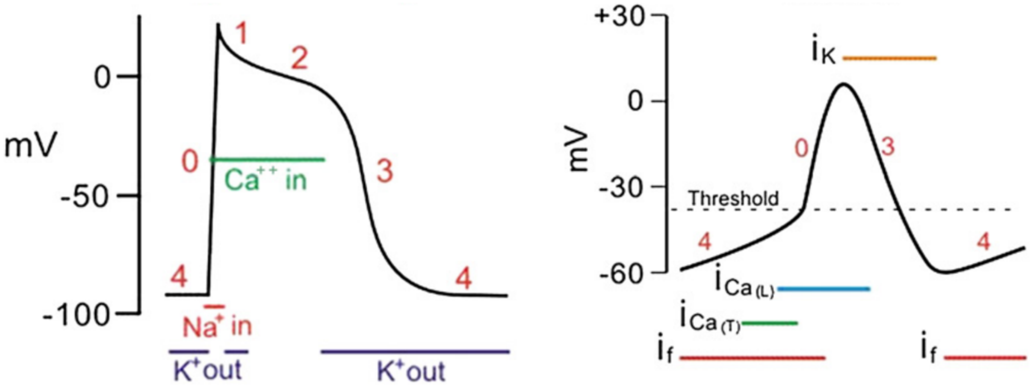

Figure 3.4 Types of action potential in the human heart adapted from (Mizzi et al., 2011).
Left panel shows a ventricular CM action potential, while right panel shows a pacemaker CM action potential.

3.3.5.2 Excitation-contraction coupling

Electrical excitation in CM triggers a precisely coordinated series of molecular events leading to contraction, a process known as excitation-contraction coupling. The main link between depolarization and force generation is the calcium-induced calcium release (CICR). Upon membrane depolarization, L-type calcium channels located in the T-tubules membrane open and allow extracellular calcium ions (Ca^{2+}) to enter the cytosol. This small influx of calcium triggers the release of a much larger quantity of calcium from the sarcoplasmic reticulum (SR) via ryanodine receptor 2 (RyR2) channels (Bers, 2002).

A key player in transmitting the rapid increase in cytosolic calcium into contraction is the troponin complex. It consists of 3 subunits, Troponin C (cTnC), where calcium binds, troponin I (cTnI) referring to its inhibitory function in the absence of calcium, and troponin T (cTnT), which anchors the complex to the tropomyosin (Boron & Boulpaep, 2020). In the resting state, when cytosolic calcium is low, cTnI stabilizes tropomyosin in a position that blocks the myosin-binding site on actin, thereby preventing cross-bridge cycling (Gordon et al., 2000). Upon cytosolic Ca^{2+} binding to cTnC, this inhibition is relived and a conformational change shifts tropomyosin away from myosin binding site on actin. This allows the cross-bridge formation to initiate contraction. Relaxation on the other hand requires re-sequestration of Ca^{2+} into the SR by the Sarco/Endoplasmic Reticulum Calcium ATPase (SERCA) pump, a Ca^{2+} pump that restores diastolic calcium levels. The removal of excess calcium takes place via sodium-calcium exchanger (NCX1), which couples Ca^{2+} efflux to Na^+ influx across the sarcolemma. The activity of SERCA2a is regulated by phospholamban (PLN), a small SR membrane protein that inhibits SERCA2a under basal conditions by lowering its Ca^{2+} affinity. During β-adrenergic stimulation, protein kinase A (PKA) phosphorylates PLN, reliving its inhibition and thereby enhancing SERCA2a activity to accelerate Ca^{2+} reuptake and promote faster relaxation (Boron & Boulpaep, 2020).

Having recapitulated in detail how adult CM sustain uninterrupted contraction, and to add that to how their proliferative capacity declines with maturation, it becomes apparent that several factors may contribute to this phenomenon. The assembly of sarcomeres, well-connected ECM, metabolic shift and increased hemodynamic workload compared to fetal CM together create an environment optimized for contraction but unfavorable for cell cycle re-entry, “All work no repair”. To test this hypothesis, an experimental model is required in which CM contraction can be reversibly switched on and off, without inducing CM cell death.

3.4 Chemogenetic tools in hiPSC-CM

3.4.1 Induced pluripotent stem cells

Stem cells are undifferentiated cells capable of self-renewal and differentiation into specialized cell types. They can be broadly categorized into embryonic stem cells (ESC), adult somatic stem cells, and iPSC. ESC, derived from the inner mass of blastocysts, possess pluripotency but raise ethical concerns due to their origin. Adult stem cells, while less ethically argumentative, are limited in plasticity and do not exist in the heart (Robinton & Daley, 2012). In 2006, a ground-breaking advance by Takahashi and Yamanaka revolutionized the field by introducing the reprogramming of differentiated somatic cells into iPSC. This discovery bypassed the ethical issues and opened ways for regenerative medicine, disease modelling, and pharmacological testing. The reprogramming of human somatic cells was achieved by overexpressing the transcription factors OCT4, SOX2, KFL4, and c-MYC, collectively known as the Yamanaka factors. These factors override the differentiated somatic identity and restart a pluripotent gene expression profile (Takahashi & Yamanaka, 2006). Non integrative methods, such as Sendai virus, have replaced earlier retroviral approaches to avoid disruption of genomic stability (Robinton & Daley, 2012). IPSC resemble ESC in morphology, transcriptome, and differentiation potential (J. Yu et al., 2007). One example is a metabolic shift from oxidative phosphorylation to glycolysis that takes place after reprogramming.

However, iPSCs often retain epigenetic memory of their cell of origin, which can bias differentiation efficiency (K. Kim et al., 2010). Moreover, reprogramming rises concerns about genomic stability and tumorigenicity, which poses challenges for therapeutic applications e.g. transplantation (Hussein et al., 2011; Okita et al., 2007).

3.4.2 Differentiation of iPSC into cardiomyocytes

Generating CM from iPSC can be achieved by replicating the embryonic cardiac development. This involves temporal modulation of the Wnt/ß-catenin pathway with small molecules. Cardiac differentiation typically begins with activation of the Wnt/ß-catenin pathway, promoting mesodermal differentiation. Activation of Wnt signalling is followed by Wnt/ß-catenin inhibition that drives the differentiation into cardiogenic lineage specifically. By day 8-15 of the differentiation, spontaneously contracting clusters are generated (Lian et al., 2012). These cells express cardiac transcription factors (Nkx2.5, Gata4), structural proteins (cTnT, α-actinin) and ion channels (HCN4, SCN5A) (Lian et al., 2012). Despite their functional features, iPSC-CM resemble fetal CM in morphology, metabolism, and electrophysiology (Yang et al., 2014). Maturation strategies include long-term culture and mechanical and electrical stimulation, 3D culture and metabolic modulation (Feyen et al., 2020; Yang et al., 2014).

3.4.3 Engineered heart tissue

Engineered heart tissue (EHTs) has emerged as a valuable platform in cardiovascular research, disease modelling, and regenerative therapy. It was first developed by Eschenhagen’s group in the late 1990s (Eschenhagen et al., 1997; Zimmermann et al., 2002). EHTs are three dimensional (3D) cardiac muscle constructs that recapitulate key structural and functional properties of native myocardium. These systems fill the gap between 2D cell culture systems and animal/in-vivo models, enabling diseases modelling (e.g. arrythmias and cardiomyopathies), drug testing but also allow for regenerative approaches. In 2025, Zimmermann's group represented the first application of EHTs allografts in humans (Jebran et al., 2025).

Early work demonstrated that casting a mixture of CM and collagen around flexible posts could generate functional tissue (Zimmermann et al., 2002). Subsequent improvement generated fibrin-based matrices which enhanced CM maturation and force generation (Hirt, Hansen, et al., 2014). Force transducers and video-optical systems quantify tension, contraction, and responses to drugs. EHTs have also been used for transplantation purposes and now entered the stage of clinical trials (*DZHK Study: BioVAT-HF-DZHK20: DZHK Study*, n.d.).

3.4.4 Genome editing

For decades researchers looked for ways to directly manipulate genes to understand biological processes and even correct genetic disorders at their source. Early attempts at gene editing and gene therapy were largely based on viral gene editing but it was limited due to the imprecise integration, variable expression, and the inability to transfer specific loci (Dunbar et al., 2018). Techniques evolved from random mutagenesis and RNA interference to programmable nucleases such as zinc finger nucleases (ZFN) and transcription activator-like effector nucleases (TALEN). These technologies allowed site specific editing from the first time but remained laborious, expensive, and difficult to scale (Hockemeyer & Jaenisch, 2016).

3.4.4.1 CRISPR technology

Then Clustered Regularly Interspaced Short Palindromic Repeats (CRISPR) came to the surface, and it markedly enhanced gene editing in every aspect. CRISPR offers a remarkably simple and programmable means of gene editing based on an RNA-guided DNA endonuclease (Ran et al., 2013). Unlike earlier systems, CRISPR/Cas9 requires only the design of a short RNA sequence to direct Cas9 to its genomic target. This introduces double stranded breaks (DSB) at the target site. The cell then repairs the DSB using non homologous end joining (NHEJ) or homology directed repair (HDR). As NHEJ comes with insertions/deletions, they are used for gene knock-out.

HDR is used by the cell to repair double stranded breaks by using the homologues chromosome as a template. In experimental setups, however, a synthetic donor DNA template can be supplied, allowing researchers to introduce precise genetic changes such as corrections or knock-ins. Accordingly, this system significantly lowers the barrier to genome editing and enables rapid inclusion across biology and medicine (Doudna & Charpentier, 2014).

In parallel, the iPSC field flourished and offered a platform that eased the ethical dilemma that the gene editing field has been facing. This allowed the generation of patient-specific cell lines, and created genetic diseases model in a dish for further analysis (Hockemeyer & Jaenisch, 2016).

3.4.4.2 PSAM- and PSAM4-GlyR cell line

The Pharmacologically Selective Actuator Module (PSAM) system represents a major advancement in the chemogenetics field, enabling a selective control over cellular excitability through artificial ligand-gated ion channels. Developed by Magnus et al. (Magnus et al., 2011), the PSAM- and PSAM4-GlyR constructs are engineered receptors that combine a modified α7 nicotinic acetylcholine receptor ligand-binding domain with the chloride-conducting glycine receptor pore. This fusion creates a receptor with higher affinity to a synthetic agonist over the endogenous ligands. PSAM-GlyR interacts with a pharmacologically selective effector molecule ($PSEM^{89S}$), while PSAM4-GlyR responds to the FDA-approved anti-smoking drug varenicline (Magnus et al., 2011, 2019).

Originally designed to achieve potent, selective, and reversible inhibition in neurons, this chemogenetic system was later adapted to iPSC-CM by the group of Weinberger in our Institute using CRISPR/Cas9 technology. These CM undergo a chloride-driven depolarization which blocks the action potential, subsequently, the contraction of the PSAM- and PSAM4-GlyR CM stops. The effect is fully reversible by washing off the ligand. The construct has a green fluorescent protein (GFP) reporter linked via 2A linker allowing identification of successfully CRISPR-edited cells (Sönmez et al., 2025).

With the hypothesis and the tools now available, I was encouraged to pursue this project as will be described in the following chapter “Aim”.

4. Aim

In this study, we hypothesized that the persistent mechanical workload of CM plays an important role in maintaining their cell cycle arrest. To test this hypothesis, I employed the chemogenetic tools PSAM- and PSAM4-GlyR that allowed for precise and reversible control of CM contraction. Using this system, I aimed to investigate whether inhibition of contraction facilitates re-entry into the cell cycle. Our approach included both in vitro and ex vivo models. In the in vitro experiments, I used PSAM4 and PSAM hiPSC-CM as monolayered CMs and engineered heart tissue, respectively. In the ex vivo experiments, I collaborated with Dr. Christine Poch to use adult human heart slices transduced with the chemogenetic tool PSAM4. Transient contraction inhibition was induced to evaluate the effects on cell cycle and CM proliferation. Furthermore, I aimed to resolve the temporal sequence of events associated with cell cycle reactivation, specifically whether contraction inhibition led to sarcomere disassembly followed by cell cycle re-entry, or vice versa.

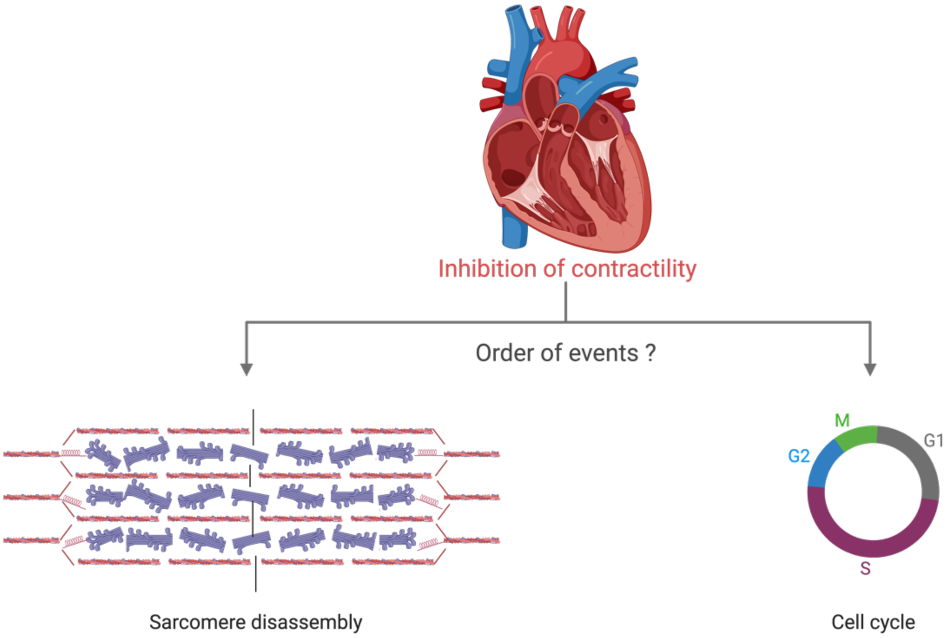

Figure 4.1 The hypothesis claims that CM re-enter cell cycle as they are relieved from the workload.

Does sarcomere disassembly precede the cell cycle activity or vice versa?

5. Methods

5.1 Human induced pluripotent stem cell culture

5.1.1 Geltrex coating

Standard cell culture vessels were coated with Geltrex® (Gibco, A1413302), diluted 1:100 with RPMI 1640 (Gibco, 21875) for 1 hour at room temperature or alternatively for 20 minutes in at 37 °C. Geltrex (0.1 mL/cm^2) was used to cover the culture vessels. For storage up to 1 month, parafilm was used to avoid evaporation at 4 °C on a flat surface.

5.1.2 Culturing and expanding hiPSC

The human iPSC wildtype cell line used in this project was UKEi001-A. It was reprogrammed from skin fibroblasts with a sendai virus strategy by the HEXT core Facility, UKE. The PSAM-GlyR and PSAM4-GlyR cell lines were derived from the UKEi001-A line. Gene editing was performed by Dr. Tim Stüdemann and is described in detail in (Sönmez et al., 2025). The 3 cell lines were negative for mycoplasma and had a normal karyotype. Regular SSEA3 analysis was performed to ensure pluripotency. Cell culture was performed under sterile conditions, without the usage of antibiotics. Precautions were taken during cell culture work, such as a facial mask, gloves, and plastic arm covers. 70% ethanol was used to disinfect all items that came in contact with cell culture. HiPSC were cultured on Geltrex-coated plates or flasks with FTDA (bFGF, TGF-β1, dorsomorphin, activin-A) medium (detailed in Table 5.1).

Cells were cultivated at 37 °C in hypoxia incubators (5% CO_2, 5% O_2), with 50-70% starting density. The feeding medium (FTDA) was changed daily. When cell confluency reached 100%, the cells were split. For this, cells were washed with 1X with dPBS (Gibco, 10010-049), followed by incubation with the dissociation agent (Accutase; Invitrogen, 00-4555-56, 0.1 mL/cm^2) for 5 minutes at 37 °C. The cells were collected in a falcon and FTDA was used to neutralize the effect of Accutase in 1:1ratio. Falcon size was determined according to the final volume of cell suspension. The cell suspension was centrifuged at 200 G for 2 minutes and the supernatant was discarded. The cell pellet was dislodged (by tapping) before resuspension. FTDA was used for resuspension and a sample (15 µL) was taken to be counted manually using the Neubauer chamber and Trypan Blue (Gibco, 15250061, 30 µL). According to the count, cells were seeded with FTDA supplemented with Y-27632 (Biorbyt, orb154626, 10uM) on the Geltrex® coated plates.

Table 5.1 FTDA medium composition

<table>
<tr><td>Components</td><td>Concentration</td><td>Supplier</td></tr>
<tr><td>DMEM without glutamine</td><td>-----</td><td>Sigma-Aldrich, D6429</td></tr>
<tr><td>L-glutamine</td><td>2 mM</td><td>Gibco, 25030081</td></tr>
<tr><td>Transferrin</td><td>5 mg/L</td><td>Sigma-Aldrich, T8158</td></tr>
<tr><td>Sodium selenite</td><td>6.6 µg/L</td><td>Sigma-Aldrich, S5261</td></tr>
<tr><td>Human serum albumin (10% solution)</td><td>1% (v/v)</td><td>Bio. Industries, 05-720</td></tr>
<tr><td>Lipid mix</td><td>0.1% (v/v)</td><td>Sigma-Aldrich, L5146</td></tr>
<tr><td>Human recombinant insulin</td><td>5 mg/L</td><td>Sigma-Aldrich, 10161</td></tr>
<tr><td>Dorsomorphin</td><td>50 nM</td><td>Abcam, ab120843</td></tr>
<tr><td>Activin A</td><td>2.5 µg/L</td><td>R&D systems, 338-AC</td></tr>
<tr><td>Transforming growth factor-β</td><td>0.5 µg/L</td><td>Peprotech, 100-21</td></tr>
<tr><td colspan="3">bFGF (Miltenyi 130-104-921, 30 µg/L) was added immediately before usage.
The medium was sterile-filtered and stored at 4 °C for a maximum of 2 weeks.
During splitting, freezing, and thawing the cells, Y-27632 (10 µM) was added.</td></tr>
</table>

5.1.3 Freezing and thawing of hiPSC

After splitting, the cells could be frozen with 10% DMSO (Sigma-Aldrich, D4540) in cold Fetal Bovine Serum (FBS; Biochrom, S0615). Warm FBS was avoided as the combination of FBS and DMSO leads to an exothermic reaction that will be too hot for the cells. 1 million cells / 1 mL freezing medium were stored in each cryotube. Isopropanol containers ("Mr. Frosty") were used during the freezing process and placed at -80 °C for 24 hours before being transferred to -150 °C for long-term storage.

For thawing the cells, cryotubes were moved from the -150 freezer on dry ice to a 37 °C water path. Two minutes later, the cells were almost completely thawed except for a small clump, to keep the freezing medium cold. Under the hood, the cryotube content was aspirated with a 5 mL serological pipette that contained FTDA (5 mL) and Y-27632, diluting out the freezing medium without inducing osmotic shock. The cell suspension was then pipetted into a 15 mL-falcon and centrifuged at 200 G for 2 minutes. The supernatant was discarded, and the cells resuspended and seeded into 1 well of a 6-well plate previously coated with Geltrex.

5.2 Cardiac differentiation

5.2.1 Monolayer cardiac differentiation

5.2.1.1 Seeding of hiPSC

Monolayer differentiations were performed in 6-well plates coated with high concentration Matrigel diluted 1:100 in RPMI 1640. HiPSC were seeded at least 3 passages after thawing (500,000 - 600,000 cells/well). For this FTDA medium supplemented with Y-27632 (2 mL/well) was used. The medium was changed on the following morning to remove the ROCK inhibitor. To start CM differentiation, the confluency of the cells had to be between 40-60%. If this confluency wasn't reached, cells were allowed to mature as per normal and passaged after reaching 100% confluency.

5.2.1.2 Differentiation media composition

Cardiac differentiation was induced using a modified BMP4/Activin A-directed protocol adapted from (Denning et al., 2015). Three key steps involved were (1) mesodermal induction, (2) cardiac specification, and (3) cardiac maturation. The following media in Table 5.2 were applied to the cells at certain time points. Stage 0 medium remained on the cells for only 16 hours whereas the remaining media were changed every 48 hours. Differentiation was performed in normoxic conditions at 37 °C.

Table 5.2 Media used in 2D cardiac differentiation

Medium (2 mL/well)	Concentration	Supplier
Stage 0 - day 1		
StemPro medium	-------	Gibco, 10639011
StemPro supplement	1:40	
BMP4	1 ng/mL	R&D systems, 314-BP
Glutamine (100X)	1:100	Gibco, 25030081
MG - high concentration	1:100	Corning, CLS354262

Stage 1 - day 2		
StemPro medium	-------	Gibco, 10639011
StemPro supplement	1:40	
Activin A	8 ng/mL	R&D systems, 338-AC
BMP4	10 ng/mL	R&D systems, 314-BP
Glutamine (100X)	1:100	Gibco, 25030081
Stage 2.1 - day 4		
RPMI 1640	-------	Gibco, 21875
B27 w/o Insulin (50X)	1:50	Gibco, 17504044
KY02111	10 µM	Tocris, 4731
XAV939	10 µM	Sigma-Aldrich, X3004
Stage 2.2 - day 6		
RPMI	-------	Gibco, 21875
B27 + Insulin (50X)	1:50	Gibco, 17504044
KY02111	10 µM	Tocris, 4731
XAV939	10 µM	Sigma-Aldrich, X3004
RDM - day 8		
RPMI	-------	Gibco, 21875
B27 + Insulin (50X)	1:50	Gibco, 17504044

5.2.1.3 Dissociation of the monolayered cardiomyocytes

CM began to beat by day 9. The cells were first washed with pre-warmed HBSS and then dissociated with Collagenase II (Worthington, LS004176; 200 U/ml, 1 mL/well) at 37 °C for up to 1 hour. Collagenase was supplemented with Y-27632 (10 µM), and BTS (TCI, B3082; 30 µM) to enhance myocyte survival during the dissociation procedure. Cells were closely monitored under the microscope for signs of singularized cells. Then cells were further dissociated with a P1000 pipette for a maximum of 5 times and collected in 50-mL falcon. For rinsing the wells and neutralizing the collagenase effect, RPMI 1640 (1 mL/well) + DNase II (Sigma-Aldrich, D8764; 12 µg/mL) were used. Next, cells were centrifuged at 100 G for 8 minutes, resuspended in DMEM/F-12, and counted with a Neubauer chamber. On average, 2 million CM were differentiated per well. A sample of 1 million CM was used for cardiac troponin T (cTnT) antibody measurement via flow cytometry. Twenty million CM were frozen per vial as previously described.

5.2.2 3D cardiac differentiation

5.2.2.1 Stage 0 - day 1 embryoid bodies (EB) formation

As described in Breckwoldt et al. 2017, hiPSC with 100% confluency in T75 flasks were washed with dPBS (10 mL). EDTA (Roth, 8043.2; 0.1 mL/cm^2) was added, and cells were incubated for up to 10 minutes at room temperature. When the singularization of the cells was confirmed with microscopy, EDTA was aspirated, and cells were collected with pre-warmed dPBS (13 mL per T175). The flasks were washed with warm FTDA and Y-27632 of similar volumes. Cell suspension was centrifuged at 200 G for 7 minutes, and cells were resuspended in Stage 0 medium at 30000 cells/mL. Manual counting was performed with a Neubauer chamber and Trypan Blue. Spinner flasks were filled with cell suspension at a density of 30-35 million cells per 100 mL. The spinner flasks were placed on a magnetic stirrer in the hypoxia incubator, for 24 hours at 40 RPM to form EB. T175 flasks were coated for 24 hours with 1% Pluronic-F127 (Sigma-Aldrich, P2443) to avoid cell attachment to the flask surface.

Table 5.3 Stage 0 medium

Component	Concentration
FTDA	---------
Polyvinyl alcohol (Sigma-Aldrich, P8136) in 1x DPBS	4 g/L
Y-27632	10 µM
bFGF was supplemented immediately before usage	30 µg/L

5.2.2.2 Stage 1 - day 2 to day 4

After 24 hours in spinner flasks, EB were collected in T175 suspension culture flasks, placed in a V-rack to allow EB to sediment in one corner. In the meantime, the Pluronic coated T175 flasks were washed with dPBS twice and filled with stage 1 medium (40 mL) and placed in a hypoxia incubator. Stage 0 medium was aspirated, and EB washed and resuspended with Stage 1 medium in a known volume. The total EB

volume was measured with a graduated 15-mL falcon tube and 10 mL EB suspension. The EB total volume was then calculated as follows:
$EB_{total} = EB_{10mL} \times V_{total}/10$ mL. 200-250 µL EB were put into one T175 flask and placed in a hypoxia incubator. Half of the medium was changed every 24 hours for 2 days, without aspirating the EB.

Table 5.4 Stage 1 medium

Component	Concentration	Supplier
RPMI 1640	---------	Gibco, 21875
Polyvinyl alcohol	4 g/L	Sigma-Aldrich, P8136
HEPES (pH 7.4)	10 mM	Roth, 9105.4
Human serum albumin (HSA)	1:20,000 (v/v)	Bio. Industries, 05-720
Transferrin	5 mg/L	Sigma-Aldrich, T8158
Sodium selenite	6.6 µg/L	Sigma-Aldrich, S5261
Lipid mix	1:100 (v/v)	Sigma-Aldrich, L5146
Y-27632	10 µM	Biorbyt, orb154626
Phosphoascorbate	250 µM	Sigma-Aldrich, 49752
Filters (0.2 µm) were used to sterilize the medium bFGF 5 µg/L, Activin-A 3 µg/L, and BMP-4 10 µg/L were added before usage.		

5.2.2.3 FDM - day 5 to day 7

V-racks were used to settle all EB in one corner of the T175 flasks, and the supernatant was aspirated. The EB were washed with FDM medium, and the total EB volume was assessed as in stage 1. The EB were distributed to the T175 flasks at 200-250 µL of EB volume per flask, and placed in a normoxia incubator (21% O_2, 5% CO_2). The medium was not changed on day 6 and a half change was performed on day 7.

Table 5.5 FDM medium

Component	Concentration
RPMI 1640	---------
Penicillin/streptomycin (Gibco, 15140)	1:50
HEPES (pH 7.4)	10 mM
HSA	1:50
Transferrin	5 mg/L

Sodium selenite	6.6 µg/L
Lipid mix	1:1000
Y-27632	1 µM
Phosphoascorbate	250 µM
FDM was filter-sterilized with a 0.2 µm filter and stored at 4 °C for up to 1 week.	
XAV-939 1 µM was added before usage.	

5.2.2.4 Stage 2 and RDM - day 8 onwards

The EB were collected at the corner of the flask and resuspended with stage 2 medium (46 mL). Half of the medium was replaced with fresh stage 2 medium daily. The EB started to contract from day 9 onwards. On day 12, the medium was replaced by RDM medium, which was continued until day 17-18.

Table 5.6 Stage 2 and RDM media

Component	Concentration
RPMI 1640	--------
Penicillin/streptomycin	1:50
HEPES (pH 7.4)	10 mM
Y-27632	1 µM
1-Thioglycerol (Sigma-Aldrich, M6145)	500 µM
The medium was filter-sterilized (0.2 µm filter) and stored at 4 °C for up to 1 week.	
B27 + Insulin (1:50) was added freshly before usage	
XAV-939 1 µM was added to stage 2 medium before usage.	

5.2.2.5 Dissociation of EB

After day 17, dissociation of the EB took place. The cells were first washed twice with pre-warmed HBSS then dissociated with Collagenase II (200 U/mL, 25 mL/T175 at 37 °C for up to 4 hours). Collagenase was supplemented with Y-27632 (10 µM), and BTS (30 µM). The cells were monitored under the microscope for the signs of dissociation. The cells were resuspended with a 10 mL serological pipette for a maximum of 5 times and collected in 50-mL falcon. For rinsing the flasks and neutralizing the collagenase II effect, RPMI 1640 (20 mL/ T175) + DNase II (12 µg/mL) were used. Next, the cells were centrifuged (8 minutes, 100 G, 4 °C), resuspended in DMEM/F-12, and counted with a Neubauer chamber. An average of 20 million CM was achieved per T175 flask. A sample of 1 million CM was used for cTnT measurement. If the CM were not used for casting or seeding freshly after the dissociation, 20 million CM per vial were frozen in the same manner as hiPSC.

5.3 Mycoplasma testing

Both cells and culturing medium were tested regularly during the project with HotStarTaq Plus Master Mix Kit (Qiagen, 203645). For cells, one million hiPSC or CM were isolated in a 1.5 mL tube and centrifuged (3 minutes, 8000 G). The pellet was frozen till the time of testing at -20 °C. For the EHTs, the medium was collected and kept at 4 °C. On the day of the analysis, the cells were incubated for 10 minutes at 100 °C and briefly centrifuged. The supernatant (2 µL) was added to PCR Master Mix as shown in Table 5.7. The cycler settings can be found in Table 5.8. Positive and negative controls were included in each run. PCR products were analysed by gel electrophoresis on 1% (w/v) agarose gel with TAE buffer.

Table 5.7 Mycoplasma PCR preparation

Substance	amounts for 1x
10x Buffer	5 µL
Q-Solution	10 µL
$MgCl_2$ (25 mM)	4 µL
Primer pool Myco-F (10 pM)	1 µL
Primer pool Myco-R (10 pM)	1 µL
dNTPs	1 µL
Taq-DNA Polymerase	0.25 µL
DNA sample	2 µL
Nuclease free water	25.75 µL
Total	**50 µL**

Table 5.8 Mycoplasma PCR cycler settings

Temperature	Time	# Cycles
95 °C	15 minutes	Once
94 °C	30 seconds	40 cycles
56 °C	30 seconds	
72 °C	1 minute	
72 °C	10 minutes	Once
4 °C	Hold	--------

Mycoplasma tests were kindly performed by Elisabeth Krämer, IEPT, UKE.

5.4 Cardiomyocytes culture in monolayer

5.4.1 Thawing of cardiomyocytes

Thawing medium was prepared by adding 10% B27 + Insulin and 1% penicillin/streptomycin in RPMI 1640 at 37 °C. CM cryotubes were transferred on dry ice from -150 °C to a 37 °C-water bath for two minutes or until a small crystal remained. with 5 mL serological pipette, the CM were transferred to a 50-mL tube. Thawing medium (1 mL) was used to rinse the cryotube and added to the 50-mL falcon 1 drop every 4 seconds. Another 1 mL was added at a rate of 1 drop every 2 seconds, then 7 mL were added within 30 seconds. The cells were counted manually using the Neubauer chamber and Trypan Blue.

5.4.2 Cardiomyocytes 2D culture

12-well plates were used for 2D CM culture coated with Geltrex as previously described. 440 000 CM/well were seeded with EHT complete medium (1 mL). The plates were placed in a 20% O_2 incubator and left untouched for 72 hours. Next, the medium was changed every 48 hours. After 7 days, a lipid-based maturation medium described in (Feyen et al., 2020) was used. Media changes were performed every 5 days. Three weeks after seeding, the CM were treated with varenicline (100 nM) for 7 days followed by a 7-day washout period. The drugs were re-administered with the medium change.

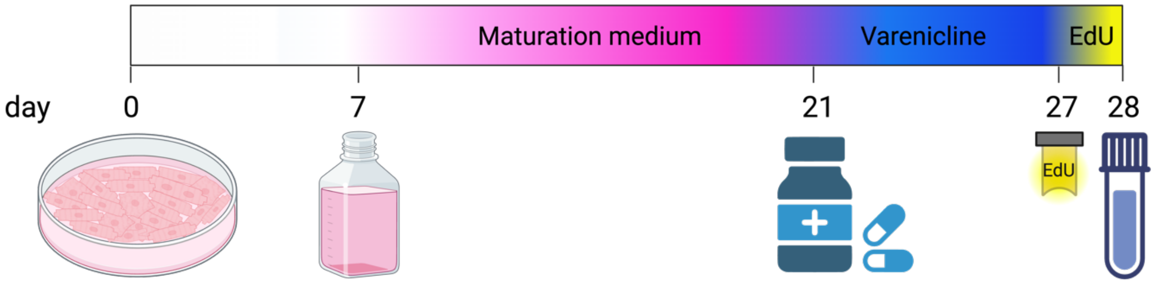

Figure .1 Cardiomyocytes 2D experiment timeline

5.4.4 Cardiomyocytes collection

The wells were washed with dPBS (1 mL/well). Then TrypLE 10X (Gibco, A1217701; 0.5 mL/well) was added and kept for 5 minutes in the incubator. During the incubation time, collection -tubes (2-mL) were prepared with dPBS 1 mL/tube to directly neutralize the effect of TrypLE on the cells. When the CM dissociation was confirmed microscopically, the cells were harvested into the arranged tubes with a P1000 pipette (maximum of 5 pipetting steps). The wells were rinsed with DMEM/F-12 (0.5 mL/well) supplemented with 10% B27/horse serum and 1% insulin, then added to the collection tubes. To avoid aggregates formation by broken DNA, the cell suspension was pipetted up-and-down 2-3 times before centrifugation (benchtop centrifuge: 4 minutes, 1000 G, 4 °C). The samples were decanted and dried on a tissue. Samples that were used for sequencing or mass spectrometry were snap frozen with liquid nitrogen and kept at -80 °C till the time of the analysis. For flow cytometry analysis, the samples were resuspended with paraformaldehyde (PFA, ThermoFisher, 047340.9M) / Histofix (4%, 0.5 mL) and transferred to FACS tubes. Samples were fixed for 10-15 minutes on ice. DPBS (1 mL) was used to neutralize the formaldehyde effect then the samples were centrifuged (3 minutes, 200 G, 4 °C). The samples were decanted as previously described (into the PFA waste) and the samples were washed once more with dPBS (1 mL/tube) then centrifuged and decanted. The samples were then prepared for flow cytometry as mentioned in chapter 5.7.

5.5 Engineered heart tissue (EHTs)

5.5.1 EHTs casting and feeding

First, EHT medium and NKM were prepared according to the following two tables:

Table 5.9 Complete EHT medium composition

Component	Concentration	Supplier
DMEM/F-12	----------	Sigma-Aldrich, D6429
Penicillin/streptomycin	1:100 (v/v)	Gibco, 15140
Horse serum inactivated	1:10 (v/v)	Gibco, 26050-088 LOT: 1590399
Insulin	10 mg/L	Sigma-Aldrich, 10161
Aprotinin	33 mg/L	Sigma-Aldrich, A1153
Prepared freshly on the same day and warmed to 37 °C.		

Table 5.10 NKM medium composition

Component	Concentration
DMEM/F-12	----------
Penicillin/streptomycin	1:100 (v/v)
Horse serum inactivated	1:10 (v/v)
Glutamine	1: 100 (v/v)
Prepared freshly on the same day and cooled to 4 °C.	

2% agarose solution was autoclaved and kept in its liquid form in a 60 °C incubator. In 24-well plates, agarose (1.5 mL) was pipetted in each well. Teflon spacers were immediately placed in the liquid agarose to form casting molds and kept for 10 minutes to harden. Meanwhile, the master mix consisting of CM and the matrix was prepared according to the following table.

Table 5.11 EHTs master mix preparation

Component	Amount for 1 EHTs
Cardiomyocytes	$1x10^6$
2x DMEM (20% of 10 × DMEM Gibco, 52100-021)	5.6 µL
Y-27632 (10 mM)	0.1 µL
Fibrinogen (Sigma-Aldrich, F8630; 200 mg/mL)	2.5 µL
NKM medium	91.8 µL
For each EHT, thrombin (Biopur, BP11-10-1104; 3 µL,100 U/mL) aliquots were prepared and placed on ice to be used directly during casting.	

When the agarose had hardened, the spacers were carefully removed, and silicone racks were situated in the formed molds. With a 100P pipette adjusted to 100 µL, the master mix was aspirated and pipetted into the thrombin aliquot. After mixing shortly, the mixture was then pipetted into the mold. The Plate was left in a hyperoxia incubator (40% O_2 and 7% CO_2, 37 °C) for an hour. To detach the EHTs from the agarose mold, EHT complete medium (0.5 mL) was added on top for 10 minutes. After confirming the detachment by microscopy, the silicone racks with the EHTs were moved gently into a new 24-well plate with complete EHT medium (1.5 mL/well). The plate was kept in hyperoxia, and the medium was changed every 48 hours. On the occurrence of rapid remodelling, i.e. thinning of the EHTs, tranexamic acid (200 µM) was added to the medium.

5.5.2 EHTs video-optical measurement

EHTs in 24-well format were measured with a video-optical platform at specialized incubators at 37 °C temperature and gas exchange of 5% CO_2 and 20% O_2 as previously described in (Hansen et al. 2010). CTMV-Software (Consulting Team Machine Vision, Pforzheim) was used to analyse the functional parameters.

5.5.3 EHT treatment and harvest

5.5.3.1 PSAM and PSAM4 cell lines

PSEM^{89S} (Tocris, 6426) and varenicline tartrate (Sigma Aldrich, PZ0004) were purchased in their powder form and were reconstituted to 100 mM with sterile DMSO and stored at -20. while varenicline stock concentration was (100 µM). Repeated freeze-thaw cycles didn’t affect the potency of the drugs. To inhibit contractionPSAM^{89S} (100 µM) or varenicline (100 nM) were added to the culture, and the drug was replenished with every medium change every 2 days. Final DMSO concentration in culture medium never exceeded 0.1%. For washout periods, the culture medium was exchanged with fresh medium without the drug. Collection of EHTs was done by placing the EHTs in Histofix® for 24 hours at 4 °C. EHTs were taken off the silicone posts and washed with dPBS, then kept in dPBS at 4 °C for further processing. EHTs used for RNA sequencing or mass spectrometry were snap frozen with liquid nitrogen and kept at -80 °C till the time of the analysis.

5.5.3.2 Mavacamten treatment

Mavacamten (Biomol, Cay19216) was purchased as a powder and constituted to 10 mM with sterile DMSO. Repeated freeze-thaw cycles didn’t affect the potency of the drug. A serial dilution of mavacamten concentrations were prepared as follows: 0.3 µM, 0.7 µM, and 10 µM. When the volume needed was < 0.5 µL (e.g. 0.3 µM), the drug was further diluted with PBS (1:100), and DMSO concentration in culture medium never exceeded 0.1%. Mavacamten was replenished with the medium change every 2 days. For washout periods, the culture medium was exchanged with fresh medium without the drug. EHTs were collected as previously mentioned.

5.6 Flow cytometry

5.6.1 SSEA3 staining

The hiPSC were permeabilized without fixation by resuspension in ice-cold 5% FBS in dPBS for 1 hour at 4 °C in FACS tubes. Cells were then centrifuged at 200 G for 2 minutes at 4 °C, and the supernatant was carefully decanted. Primary staining was performed using PE-conjugated rat anti-SSEA3 antibody (1:5 dilution in 5% FBS/dPBS), with a PE-conjugated rat isotype control (1:40 dilution) run in parallel. After 30 minutes of incubation at 4 °C, cells were washed twice with 5% FBS in dPBS and once with dPBS alone to remove unbound antibodies. Finally, cells were resuspended in dPBS (250 µL) and analysed on the Agilent Quanteon flow cytometer (FACS Core Facility, UKE).

5.6.2 Cardiac troponin T staining

The CM pellet was fixed for 10 minutes with Histofix or 4% PFA on ice in FACS tubes. Next, 2 washing steps with dPBS (1 mL/tube) were completed with decanting the supernatant and drying the tip of the tubes on tissue. For permeabilization, FACS buffer (0.5 mL/tube) was used for 60 minutes (cells were kept at this stage up to 3 days) at 4 °C.

Table 5.12 FACS buffer preparation

Component	Concentration	Supplier
dPBS	500 mL	Gibco, 10010-049
FBS	25 mL	Biochrom, S0615

Saponin	2.5 g	Sigma Aldrich, S7900
Sodium azide	0.25 g	Sigma Aldrich, S2002

Following permeabilization, samples were centrifuged (3 min, 200 G, 4 °C), and an APC-conjugated cTnT antibody (1:50) or corresponding isotype control was added. Incubation was performed for 1 hour up to 24 hours. Samples were washed twice with FACS buffer and once with dPBS, then resuspended in 250 µL dPBS. Samples were analysed on the Agilent Quanteon flow cytometer (FACS Core Facility, UKE). All centrifugation steps were carried out under the same settings.

5.6.3 Cell Cycle and DNA Content

Cell cycle activity and DNA content were assessed via flow cytometry. 5-Ethynyl-2`-deoxyuridine (EdU; 10 µM) was added to cultures 24 hours prior to harvesting. After permeabilization, click-IT reaction with was performed as per manufacturer protocol using a mastermix containing Alexa-Fluor azide and $CuSO_4$. Samples were stained with an APC cTnT antibody and Dapi/Hoechst (1:1000) for 1 hour, washed, and resuspended in dPBS (250 µL). Data acquisition was performed using the Agilent Quanteon cytometer. Centrifugation conditions remained consistent throughout (3 min, 200 G, 4 °C).

5.7 PSAM4-mediated modulation in human heart slices

These experiments were performed by Dr. Christine Maria Poch in the Department of Medicine and Regenerative Medicine at the Technical University in Munich (TUM). Ex vivo heart slices were prepared from explanted DCM hearts, following the protocol by Poch et al. (2021). Within 24 hours, the slices adapted to the biomimetic chambers, and they were transduced with an AAV6 vector encoding a cardiac-specific cTnT promoter-PSAM4 construct (rssAAV6-TnT-nls-TagRFP-2A-PSAM4-GlyR), produced by the Vector Core Facility, UKE. Transduction was confirmed microscopically after 24 hours. Treatment with varenicline (100 nM) was initiated on day 7 and continued for 7 days. Contractile force was recorded throughout the experiment. Post-experiment immunofluorescence analysis after samples were fixed and embedded in gelatine (Sigma Aldrich, G9382). Tissues were sectioned on vibratome (Leica Biosystems) to 1 cm × 2 cm × 300 µm. Slices were anchored in biomimetic cultivation chambers

(MyoDishes; InVitroSys) with tissue adhesive (histoacryl; B. Braun) according to fibre direction and subjected to physiological preload of 1 mN and stimulation at 1 Hz, as previously described (Fischer et al., 2019; Poch et al., 2022). The sections were blocked and permeabilized for 2 hours at room temperature in a solution containing Triton X-100 (Sigma-Aldrich, 93422; 0.1%), Tween 20 (Sigma-Aldrich, P6585, 0.05%), and FBS (Biochrom, S0615, 10%). Primary antibodies were diluted in 0.1% Triton X-100, and 10% FBS (according to Table 5.13) and incubated overnight at 4°C. Following incubation, sections were washed with a 0.05% Tween 20 solution. Secondary antibodies were then applied and incubated for 2 hours at room temperature. After several washing steps, nuclei were stained with Hoechst 33258. Slides were mounted with Anti-Fade Fluorescence Mounting Medium (Abcam, AB104135) and sealed with a coverslip. Images were acquired with two separate systems: a Leica DMI8 Thunder microscope and a Leica TCS SP8 confocal microscope. Image acquisition was performed using the LAS X software (Leica Microsystems). Image analysis was conducted with Fiji software.

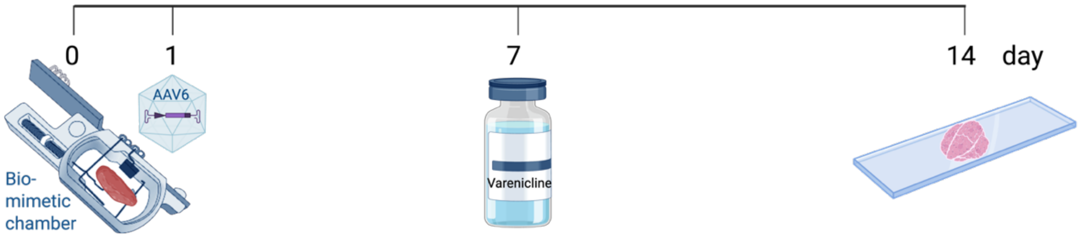

Figure 5.2 Heart slices transduction with AAV6-PSAM4-GlyR timeline

Table 5.13 Heart slices immunostaining antibodies

Target	**Host**	**Reference**	**Titer**
Anti-Mouse IgG Alexa Fluor 488	Goat	Invitrogen A11001	1:500
Anti-Mouse IgG Alexa Fluor Plus 647	Goat	Invitrogen A32787	1:500
Anti-Rabbit IgG Alexa Fluor 647	Goat	Invitrogen A31573	1:500
Cardiac Troponin T	Mouse	Invitrogen MA5-12960	1:300
Hoechst 33258		Sigma-Aldrich 94403	1:500
Phospho-Histone H3 Alexa Fluor 647	Rabbit	Cell Signaling 9716S	1:100
RFP Booster ATTO594	Alpaca	Proteintech rba594	1:100

5.8 Histology and Immunofluorescence

EHTs were embedded in 4% agarose and sectioned (70 µm) with a vibratome. Sections were blocked in 1% bovine serum albumin (BSA; Sigma Aldrich, A9418) and 0.3% Triton X-100 in PBS for 60–90 minutes at room temperature, then incubated overnight at 4 °C with primary antibodies (dilutions as listed in Table (5.14). Following three PBS washes, samples were incubated with fluorescent secondary antibodies for 1 hour at room temperature. Stained sections were washed again, mounted with Fluoromount, and topped with coverslips. Slides were air-dried overnight and imaged using a Zeiss 700 confocal microscope.

Table 5.14 Immunofluorescence antibodies

Antigen	**Titer**	**Supplier**
Ki67	1:1000	ThermoFisher, 14-5698-82
α-Actinin	1:800	Sigma, A7811
Titin-9	1:100	Myomedix
Phalloidin	1:250	ThermoFisher, A22284
PH3	1:1000	Cell signaling, 9701L
YAP1	1:100	Abcam, ab56701
Dapi	1:1000	

5.9 Live-Cell Imaging of PSAM4 Cardiomyocytes

PSAM4 CM were cultured on Ibidi µ-Dish 35 mm Quad or black 96-well glass-bottom plates. Cells underwent 3 weeks of maturation, followed by treatment on day 21 with varenicline (100 nM), HEPES (20 mM), and SiR-Tubulin (Spirochrome, CY-SC002, 100 nM) for ≥ 6 hours. Imaging was performed using a Nikon Ti2-E microscope under normoxic conditions. Images were acquired every 15 minutes over 3 days using 40x magnification with an 11 nm^2 ROI.

5.10 Bottom-up proteomics

5.10.1 Sample preparation

The following experiment was done by Paula Nissen and Bente Siebels from the Core Facility Mass Spectrometric Proteomics (UKE). EHTs and CM were lysed in 0.1 M triethylammonium bicarbonate (TEAB, ThermoFisher) with 1% (w/w) sodium deoxycholate (SDC, Sigma-Aldrich). EHTs were homogenized with a TissueLyser II (Qiagen), heated at 95 °C for 5 min, and sonicated (10 pulses, 30% power). CM were heated at 95 °C for 10 minutes prior to identical sonication. Protein concentrations were measured with the Pierce™ BCA Assay (ThermoFisher). For digestion, 10 µg (EHTs) or 20 µg (CM) of protein were reduced with 10 mM DTT (30 minutes at 56-60 °C), then alkylated with 20 mM IAA (30 minutes at 37 °C, dark).

Protein clean-up and digestion followed the SP3 protocol (Hughes et al., 2019) using carboxylate-modified magnetic E3/E7 SpeedBeads (Cytiva) at a 10:1 bead-to-protein ratio. Binding occurred in 50–70% ACN while shaking (10–18 minutes at 600–1400 rpm). Beads were washed twice with 100% ACN and twice with 80% ethanol (EHTs) or 70% ethanol (CM). Beads were resuspended in 100 mM (EHTs) or 50 mM (CM) ammonium bicarbonate and digested overnight at 37 °C with sequencing-grade trypsin (Promega, 1:100 ratio). Trypsin was inactivated with 1% TFA (EHTs only). For CM, peptides were rebound to beads with 95% ACN, washed (2x 100% ACN), eluted in 2% DMSO/1% formic acid, dried, and stored at –20 °C. Peptides (EHTs) were transferred to LoBind plates for LC-MS/MS analysis.

5.10.2 Proteomics differential quantitative in (DDA) Mode

Proteomic analysis was performed using a Dionex Ultimate 3000 UPLC system (ThermoFisher) coupled to high-resolution mass spectrometers: a Q Exactive Orbitrap for EHTs and an Orbitrap Fusion for CM (both ThermoFisher). Peptides (1 µL) were injected via autosampler, purified on a C18 trap column (100 µm × 20 mm, 5 µm, 100 Å), and separated on an analytical column (75 µm × 250 mm, 1.7 µm, 130 Å, BEH C18, Waters). A binary solvent system (0.1% formic acid in water/ACN) was used with a linear gradient from 2% to 30% ACN over 60 minutes (total runtime: 80 min). Samples were ionized using nano-ESI at 1,800 V. Acquisition was performed in DDA mode, with MS1 scans in the Orbitrap across 400–1,200 m/z (Q Exactive) or 400–1,300 m/z (Fusion). Key differences in acquisition settings are summarized below:

Q Exactive (EHTs):
MS1: 70,000 resolution, AGC target 1e^6, max IT 240 ms
Top15 precursors (2+ to 5+, >5x10^3) isolated (2 m/z), HCD at 25%
MS2: 17,500 resolution, AGC 1x10^5, max IT 50 ms, dynamic exclusion 20 s

Orbitrap Fusion (Cardiomyocytes):

MS1: 120,000 resolution, AGC 2x10^5, max IT 120 ms

TopSpeed (3 s), precursors (2+ to 5+, >1,000), isolation 1.6 m/z, HCD at 30%

MS2: Ion trap, rapid scan, AGC 1x10^5, max IT 60 ms, dynamic exclusion 30 s

5.11 RNA sequencing

To uncover the transcriptional mechanisms underlying the observed increase in cardiomyocyte proliferation, we performed RNA sequencing on CM cultured in monolayer for 4 different conditions: control (28d), treated for 7 days (28d), wash-out for 7 days (35d) and time-matched control (35d). Total RNA was extracted from snap-frozen CM samples and assessed for integrity using the Agilent TapeStation system. High-quality RNA (RIN > 8) was poly(A) -enriched and used for directional library preparation (NEBNext Ultra II, NEB), followed by quantification and equimolar pooling. Libraries were sequenced on the Illumina NextSeq2000 platform (single-end, 72 cycles). Sequence reads were processed with fastp (v0.23.2) to remove sequences originating from sequencing adapters and sequences of low quality using the program's default parameters. Mismatched base pairs in overlapping regions with one base with high quality while the other was ultra-low quality were corrected with the --correction option (Chen et al., 2018). Reads were then aligned to the human reference assembly (GRCh38.110) using STAR (v2.7.10a) (Dobin et al., 2013). Differential expression was assessed using DESeq2 (Love et al., 2014). A gene was considered significantly differentially expressed if the corresponding absolute fold change was not less than 1.5 and the false discovery rate (FDR) did not exceed a value of 0.05. Overrepresentation (ORA) and gene set enrichment analysis (GSEA) was performed with clusterProfiler (T. Wu et al., 2021) in combination with a selection of the Molecular Signatures Database (MSigDB) subsets C2 and H, i.e. Biocarta (Nishimura, 2001), KEGG (Kanehisa & Goto, 2000), Reactome (Jassal et al., 2020), WikiPathways (Pico et al., 2008) and the Hallmark gene sets. The Gene Ontology (GO) resource (Ashburner et al., 2000) was analysed separately. Transcription factor activity predictions are based on DoRothEA (v1.6.0) (Garcia-Alonso et al., 2019).

5.12 Silencing small interfering RNA (siRNA)

In order to knockdown (KD) the gene of interest mRNA in 2D CMs, silencing siRNA approach was used. For the matured CMs, siRNA transfection mixture was prepared. OPTI-MEM media (ThermoFisher, 31985070, 75 µL) and RNAiMAX lipofectamine (ThermoFisher 13778030, 4.5 µL) were mixed and this tube was labelled tube A. In another tube OPTI-MEM media (75 µL) and YAP1 silencing siRNA (ThermoFisher, S536627, 1.5 µL) were mixed and this tube was labelled tube B. The content from tube B was pipetted carefully into tube A, mixed gently, and incubated for 5 minutes at room temperature. 125 µL/well of the mixture were added dropwise onto the CM with maturation media (1 mL) then incubated overnight at 37 °C. On the following day, the transfection medium was exchanged with fresh maturation media and the cells were incubated for another 48h. On day 3, varenicline (100 nM) and EdU (Invitrogen, C10338, 10 µM) were added to the CM for 24 hours then the cells were harvested for flow cytometry analysis and real time qPCR.

5.13 Real time quantitative poly chain reaction (RT-qPCR)

RNA from 2D CM samples were extracted with TRIzol™ (Invitrogen, 15596026) reagent according to the manufacturer protocol. In brief, TRIzol™ (0.5 mL) were added per well and collected in 1.5-mL tubes. At this point, the cell suspension can be kept in -20 °C for up to 12 months or processed directly. Chloroform (AtomScientific, GWN9009-D, 0.1 mL) was added to the cell suspension and mixed by shaking. After incubation for 2–3 minutes, the samples were centrifuged (15 minutes, 12,000 G, 4 °C). Only the upper aqueous transparent phase was collected with a P100 pipette in a fresh 1.5-mL tube, followed by the addition of isopropanol (Sigma-Aldrich, 1.13350, 0.25 mL) and mixing by inversion. The samples were incubated for 10 minutes at room temperature then centrifuged (10 minutes, 12,000 G, 4 °C). Total RNA precipitated formed a small pellet at the bottom of the tube and the supernatant was discarded by decanting. The pellet was resuspended in ethanol (75%, 0.5 mL) and vortexed shortly, then centrifuged (5 minutes, 7500 G, 4 °C). A critical step was to get rid of all the ethanol-containing supernatant by decanting and gently tapping on a tissue. The remaining supernatant was left to eavporate for 10-20 minutes. The samples were resuspended in RNase-free water (25 µL) and incubated in a water bath or heat block set at 55–60 °C for 10–15 minutes. Nanodrop was utilized to measure the RNA concentration. RNA samples were stored at -80 °C.

Complementary DNA (cDNA) was prepared according to the SuperScript® III First-Strand Synthesis System for RT-PCR Kit (Invitrogen, 18080051) protocol. Briefly, RNA (200 ng) was used to synthesize cDNA, as well as samples without the reverse transcriptase (SuperScript® III RT) serving as a negative control to the cDNA synthesis procedure. Primers (Table 5.15) were designed using Primer Blast NCBI and tested with AmpliTaq Gold DNA Polymerases kit (Applied Biosystems, 4311806) against cDNA samples, -RT sample and a water sample. Using a pre-dilution of the primers and cDNA to 1:10, quantitative PCR (qPCR) was performed in triplicate 10 µL-reactions containing SYBR Green (Roche, 4913850001, 5 µL), RNase free water (3.4 µL), forward primer (0.3 µL), reverser primer (0.3 µL) and diluted cDNA (1 µL). GUSP was used as a housekeeping gene.

Table 5.15 qPCR primers list

Primer name	Sequence
MKI67 forward	GAGCGGTGGTTCGACAAGTG
MKI67 reverse	AGGGGAAGGCCAGAAGCAAA
GUSb forward	ACGATTGCAGGGTTTCACCA
GUSb reverse	CACTCTCGTCGGTGACTGTT
YAP1 forward	AGGTGAGGCCACAGGCAATG
YAP1 reverse	GAGTCCCACCATCCTGCTCC

5.14 G-/F-Actin Western blot

To quantify the ratio of globular (G-) to filamentous (F-) actin, cells were lysed using a G-Actin/F-Actin In Vivo Assay Kit® (Cytoskeleton, BK037) following the manufacturer’s protocol. Briefly, cells were gently lysed in a stabilization buffer to preserve actin polymerization states, followed by ultracentrifugation at 100 000 G for 1 hour to separate G-Actin (supernatant) from F-Actin (pellet). The F-Actin pellet was depolymerized on ice in equal-volume dissociation buffer, and both fractions were separated by SDS-PAGE along with the controls. Proteins were transformed to a PVDF membrane (BioRad, 4561086), probed with an anti-Actin primary antibody (supplied by the kit), and detected using anti-mouse-HRP secondary antibody (Promega, W4021) diluted according to the manufacturer recommendations. As a housekeeping protein, anti-S6 ribosomal protein rabbit antibody (Cell signalling, 2217) was used with the appropriate secondary antibody Alexa Fluro 647. Protein expression levels were quantified by densitometry and normalized to S6 using ImageJ/Fiji.

5.15 Image analysis

For quantitative image analysis, Fiji/ImageJ (Schindelin et al., 2012), an open source platform for biological image processing, along with the StarDist plugin (Weigert & Schmidt, 2022) for automated nucleus segmentation were used. StarDist employed a deep learning-based approach to detect and segment cell nuclei for robust quantification of nuclei. Following nuclear segmentation, sarcomere organization and structural features were analysed using the SarAsM (Sarcomere Analysis Multitool) (Stein et al., 2022), a specialized algorithm designed for high-precision sarcomere length and regularity assessment.

5.16 Statistical analysis

GraphPad Prism software 8.4.3 was used to perform statistical analysis. All data was depicted as mean ± SD unless otherwise stated. p-value lower than 0.05 was considered statistically significant. When applicable, data were analysed using unpaired Student’s t-test or one-way ANOVA to determine whether the difference between groups was statistically significant.

6. Results

6.1 Effects of inhibiting contraction in 2D culture

6.1.1 Characterization of cardiomyocytes during contraction inhibition

CM were cultured in 6- or 12-well plates for 21 days followed by a 7-day treatment period with varenicline (100 nM). The contraction of PSAM4 CM treated with varenicline stopped within a few seconds after drug application. 7 days of varenicline treatment led to reduced CM size as indicated by the forward scatter area and a slight decrease in cTnT expression when compared to control group. CTnT% dropped from 90.3% ± 1.1 in control to 82.4% ± 3.3 in treated group. These effects were fully reversible after washout. The size of CM was bigger and cTnT% increased to 88.4% ± 5.6 (Fig. 6.1).

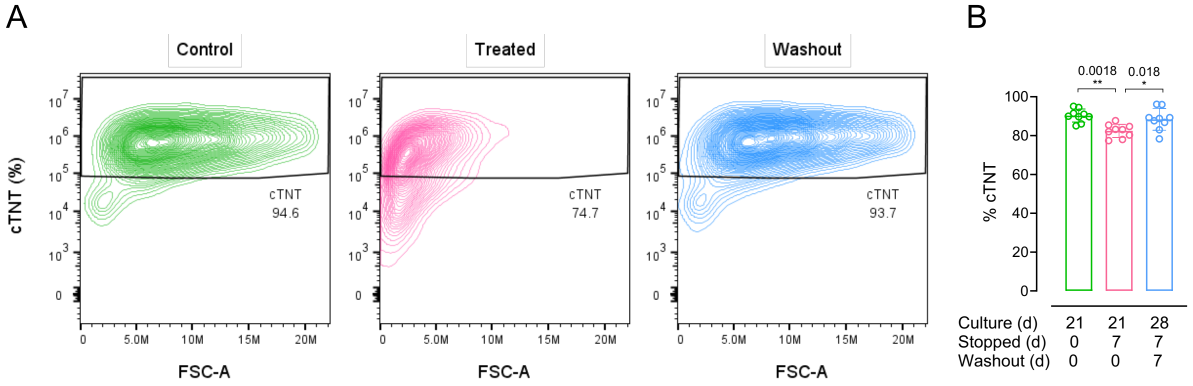

Figure 6.1 cTnT expression and CM size decreased upon the inhibition of contraction

(A) *Representative contour blot showing forward scatter area (FSC-A) on the x-axis and cTnT expression on the y-axis in CM cultured for 28 days. FSC-A distribution shifted towards the left in the treated group indicating reduction in cell size by ~1/2. Both control and washout groups showed similar results for cTnT expression and CM size.* ***(B)*** *Treatment with varenicline for 7 days led to a reduction of the percentage of cTnT$^+$ cells while washing the drug out led to recovery of cTnT values. Quantification was performed on n=3 wells per experiment, and N=3 experiments from different CM differentiation runs. Mean ± SD is depicted. Significance as indicated.*

6.1.2 CM apoptosis and cell death

On this note, we wanted to study the effect of contraction inhibition on CM cell death. Thus, the media collected from the cultures were tested for LDH concentration. Media from the varenicline-treated (i.e. stopped) CM did not show elevation in LDH when compared to beating control CM. In contrast, values were lower (0.11 ± 0.01 in stopped CM vs. 0.14 ± 0.02 in beating control; **Fig. 6.2**).

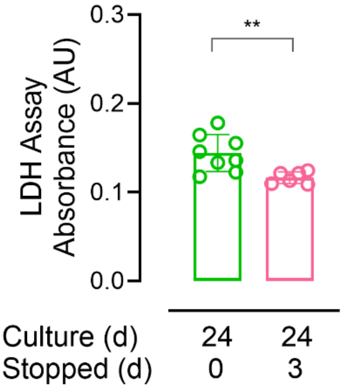

Figure 6.2 Inhibition of contraction did not lead to cell death

Inhibition of contraction using varenicline (100 nM) in 2D PSAM4 CM did not result in an elevation of LDH concentration in the culture medium, indicating the absence of treatment-related cell death. One data point represents one well. Significance levels were obtained using Student's t-test, p < 0.01 (**).

6.1.3 Assessment of cell cycle activity and proliferation upon contraction inhibition

EdU incorporation was used to study cell cycle activity in CM. EdU incorporation was specifically measured in the cTnT$^+$ population. Contraction inhibition resulted in a larger number of EdU$^+$ CM compared to control beating CM. The percentage of EdU$^+$ cells was significantly higher in the stopped CM from 3 different biological batches when compared to the beating control (control CM: 5.0% ± 2.8 vs stopped CM: 14.4% ± 1.7). EdU incorporation rate subsequently declined to 2.8% ± 1.3 after varenicline washout and re-initiation of contraction (**Fig 6.3**).

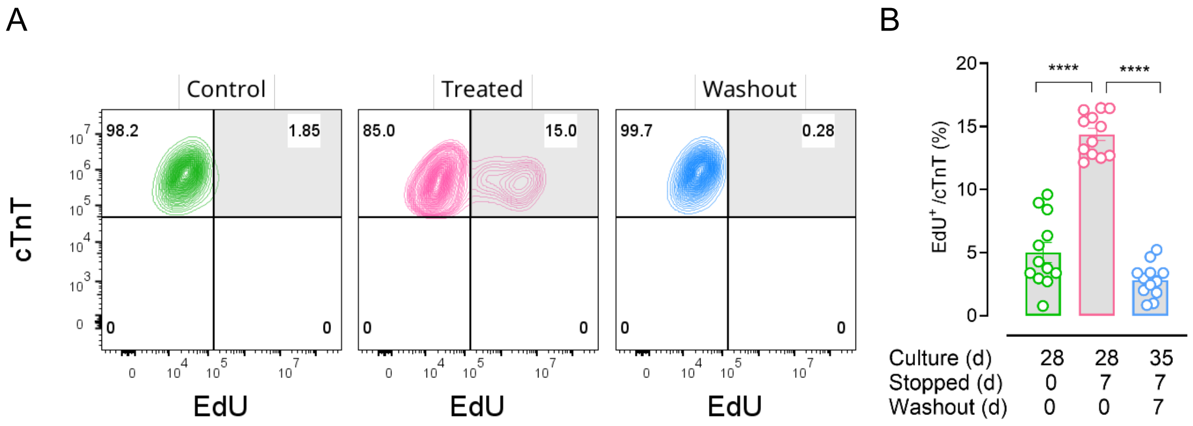

Figure 6.3 Elevated DNA synthesis after 7 days of contraction inhibition

(A)** Contour plots indicating the cell cycle activity in PSAM4 CM. Cardiac TnT displayed on the Y-axis and EdU on the x-axis. EdU incorporation increased in stopped CM compared to beating CM indicating* *higher cell cycle activity. The shaded gate represents EdU^+/ $cTnT^+$ cells.* ***(B) *Quantification of the percentage of EdU^+/ $cTnT^+$ across the different experimental conditions. Statistical significance was determined using one-way ANOVA. Significance levels were $p < 0.0001$ (****).*

The proportion of EdU^+ CM showed an increase across the ploidy states and nuclear configuration after treatment with varenicline, as indicated by Hoechst staining. The 2n nuclei fraction of EdU^+ CM was higher in treated samples (3.8% ± 0.5) than in control samples (1.5% ± 0.3), indicating newly formed diploid mononucleated CM. Varenicline treatment also increased the 4n nuclei fraction of EdU^+ CM (4.0% ± 2.9) compared to control (1.3% ± 0.6, mean ± SD). Higher ploidy states also showed a trend of increase; however, this did not reach significance **(Fig. 6.4).**

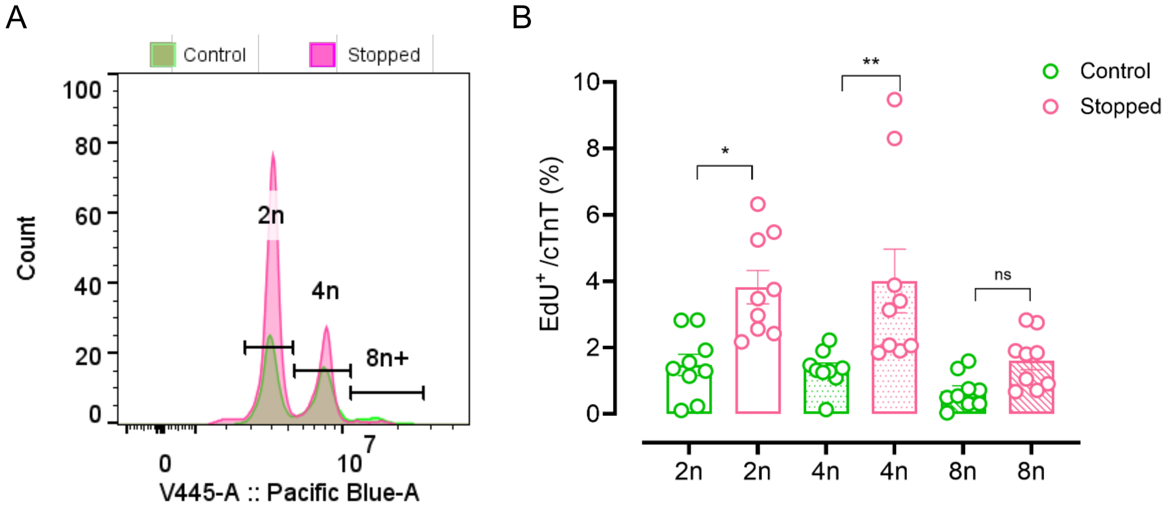

Figure 6.4 Higher percentage of cells within diploid and polyploid EdU^+ CM
(A) *Flow cytometry histograms of DNA content (Pacific blue-A) in control (green) and varenicline-treated (pink) PSAM4 CM, showing peaks corresponding to 2n, 4n, 8n+ nuclei.* ***(B)*** *Quantification of Hoechst intensity normalized to EdU^+ CMs for different ploidy states. Statistical significance was determined using one-way ANOVA. Significance levels were $p < 0.1$ (*), $p < 0.01$ (**), ns = not significant.*

6.1.4 Live cell imaging to evaluate CM proliferation

To investigate whether PSAM4 CM undergo complete cell division rather than only cell cycle re-entry, I performed time-lapse imaging over a period of 3 days. The cells were labeled with SirTubulin to visualize the microtubule network and monitor spindle formation in real time. Clear mitotic events and successful cell division in both control and treated conditions were observed, however in treated (i.e. stopped) CM the frequency was much higher. Importantly, I was able to track individual cycling cells and confirm the emergence of two distinct daughter cells **(Fig 6.5).**

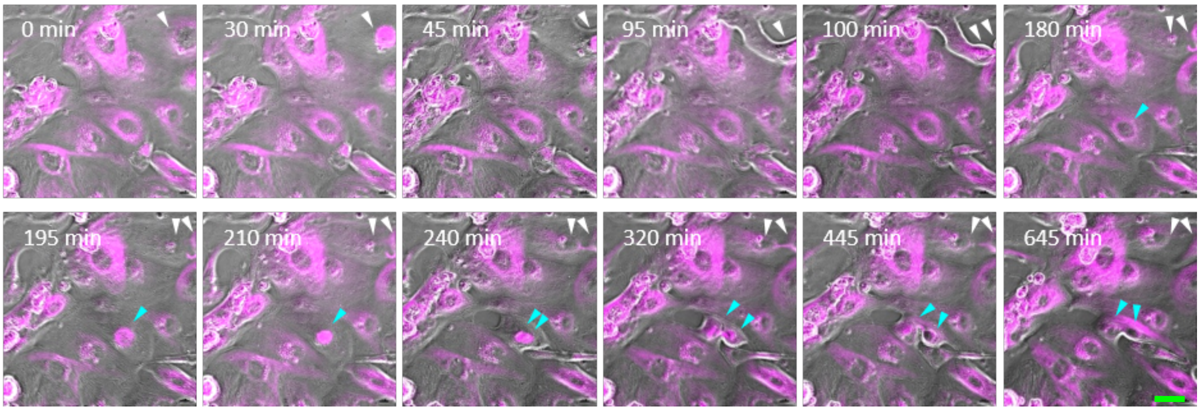

Figure 6.5 Time lapse images of varenicline-treated CM

Representative images of stopped CM stained with the tubulin marker SirTubulin (pink), acquired over 72 hours. White arrows indicate the first observed cell division event, while blue arrows mark another cell undergoing cell division. Scale bar is 20 µm. Time stamp as indicated.

6.2 Effects of inhibiting contraction in EHTs

6.2.1 Physiological EHT characterization

EHTs were used as a model as they provide a 3D environment that supports CM alignment under auxotonic contraction. To study EHTs contraction I employed optical-video recording systems described in (Hansen et al., 2010) which tracks the deflection of silicone posts during spontaneous beating. From these recordings, parameters including force, frequency, relaxation/contraction time and time to peak could be calculated. This approach allowed us to study the development and performance of the EHTs under different conditions.

I first conducted experiments using wild-type (WT) ERC1 EHTs to study whether PSEM^{89S} had any effect on WT EHTs. WT EHTs were cultured, and their contractile force was measured 2 hours after each medium change. Over time the contractile force gradually increased to ~ 0.2 mN. Comparative analysis via Student's t-test demonstrated no significant difference between treated and untreated ERC1 EHTs (control: 0.17 mN ± 0.03, treated: 0.17 mN ± 0.06; mean ± SD, $p < 0.05$). Next, the drug was washed out from the treated ERC1 EHT medium, without any observed effect **(Fig. 6.6).**

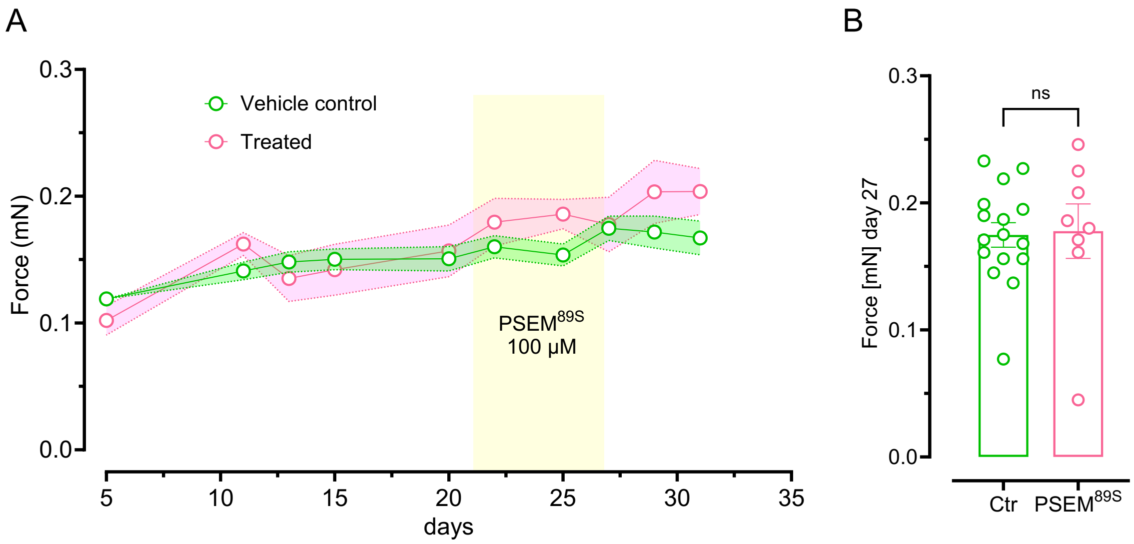

Figure 6.6 PSEM^{89S} did not affect the contractile force of ERC1 EHTs

***(A)** Time curse of contractile force developed in control (green) and PSEM^{89S}-treated EHTs (pink). The yellow box indicates the treatment period (days 21-28), with 100 µM PSEM^{89S}. No obvious difference in force generation was observed between groups during or after treatment. **(B)** Bar graph comparing mean contractile force on day 27 (endpoint of treatment). Control and treated EHTs had similar forces with no statistically significant difference using Student's t-test.*

Next, I used PSAM EHTs, in which contraction could be completely and reversibly silenced by PSEM^{89S}. To examine the effects of contraction inhibition, EHTs were cultured for 21 days allowing a short maturation period before treatment. Force measurements were recorded 2 hours after each medium change. On day 21, PSEM^{89S} (100 µM) was added for 1, 7 or 21 day(s), leading to complete contraction inhibition within minutes. After the assigned treatment period, the drug was washed out, allowing the EHTs to gradually regain contraction and generate force comparable to untreated controls (**Fig 6.7**).

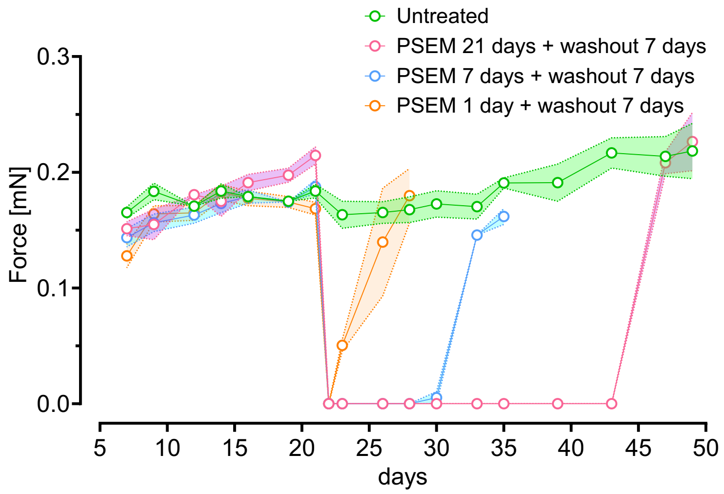

Figure 6.7 Reversible contraction inhibition of the PSAM EHTs after 21-day maturation period
Treatment with PSEM^{89S} (100 µM) completely abolished force generation by the PSAM EHTs at all time points. After drug removal the force recovered rapidly reaching the same force as time-matched controls within 7 days.

In the attempt of making the EHTs mature further, resembling human adult heart tissue more closely, I extended the cultivation period to 2 months before initiating treatment. The medium was then supplemented with PSEM^{89S} for 7 days followed by 7 days of washout. The force was recorded 2 hours after every medium change. Identical to the shorter maturation period, upon the application of the drug the EHTs stopped contracting. After the 7-day treatment period the drug was washed out, thus contraction restarted again and the EHTs recovered **(Fig. 6.8).**

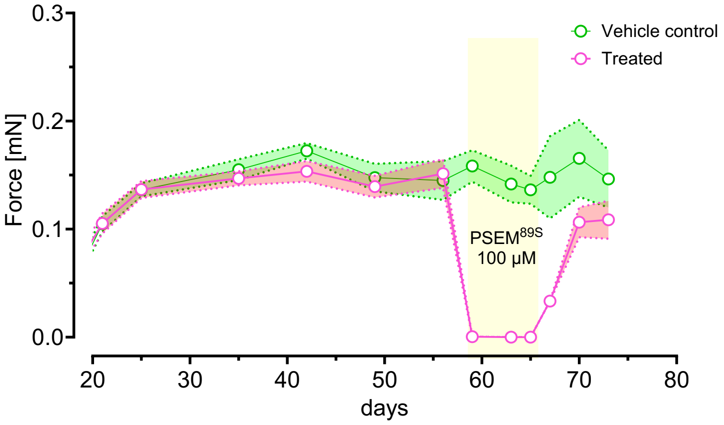

Figure 6.8 Prolonged maturation did not alter the PSEM^{89S} effect on the PSAM EHTs
After maturing the EHTs for 63 days, PSEM^{89S} was added, inhibiting the contraction. Washing out the drug led to re-initiation of contraction as observed in younger EHTs.

Second, EHTs were treated immediately after casting (day 0) without prior maturation and maintained in a non-contractile state for either 14, 21, or 42 days. Upon drug washout, all treatment groups started to beat and generate contractile force within few minutes as a syncytium. Surprisingly, they reached similar forces to that generated by the untreated EHTs within 7 days **(Fig 6.9).**

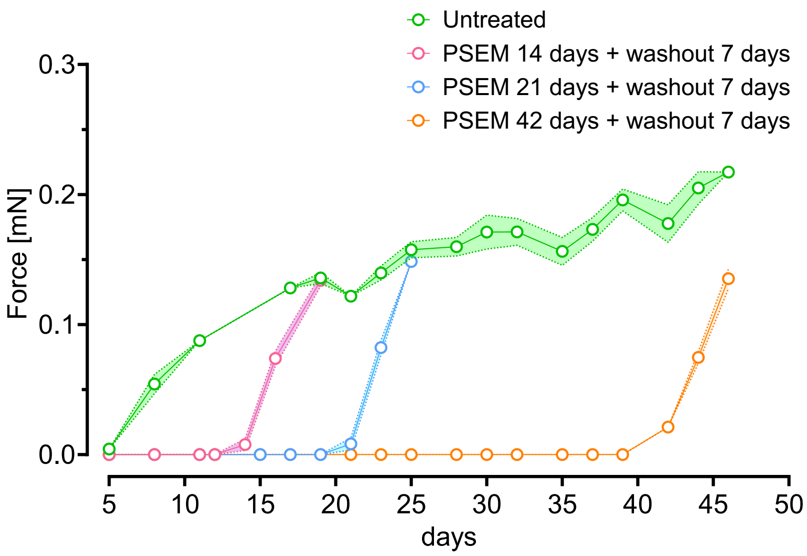

Figure 6.9 EHTs treated from d0 started beating after 7 days washout

Treatment with PSEM^{89S} (100 µM) completely abolished force generation by the PSAM EHTs at all time points. After drug removal the force rapidly started to generate force, reaching the control levels within 7 days, except for the 42-day treatment group, which was still in the process of recovery.

When the contractile activity was blocked for an extended period of 63 days, EHTs failed to recover even after 3-week washout period **(Fig. 6.10).**

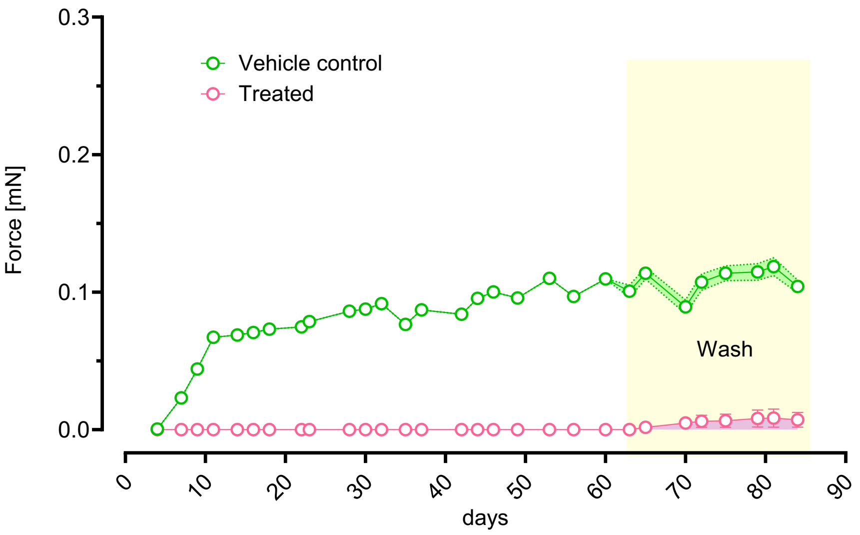

Figure 6.10 Prolonged force inhibition impaired EHT contraction

PSAM EHTs were subjected to continuous contraction inhibition from the day of casting (d0) for a duration of 63 days. Following withdrawal of PSEM^{89S} from the culture medium, the EHTs did not recover, with generated force below 0.02 mN compared to 0.1 mN force generated by the control EHTs.

To validate the observed contraction modulation in the PSAM EHTs, three independent CM batches were cast and tested with PSEM^{89S}. For subsequent analysis of contractile response and its effect on sarcomeres and cell cycle, I focused on two primary groups: EHTs treated for one week following either a short- or prolonged-maturation periods. Quantification of the force generation across all three batches showed only minor variability among control and wash groups, but consistently resulted in complete inhibition of contraction upon the PSAM-mediated channel activation **(Fig 6.11).**

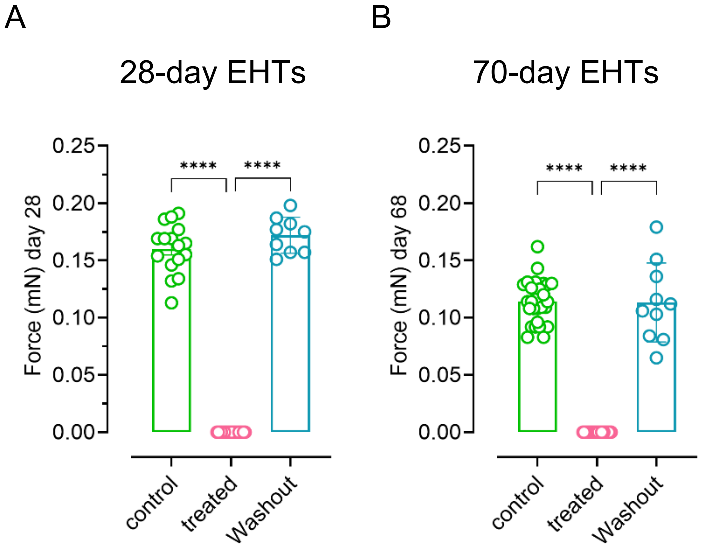

Figure 6.11 Complete abolishment of generated force upon treating PSAM EHTs with PSEM^{89S}
(A) EHTs cultured for 21 days then treated with PSEM89S (100 µM) for 7 days did not generate any force (0 mN ± 0, n = 20) compared to time-matched control (0.16 mN ± 0.02, n = 16). Drug washout for 7 days led to full recovery of the EHTs to generate force similar to the control group (0.17 mN ± 0.05, n = 9). (B) Similarly, EHTs cultured for 63 days and treated with PSEM89S (100 µM) for one week (control: 0.11 ± 0.01, n = 28, treated: 0 mN ± 0, n = 28, Washout 0.11 mN ± 0.03, n = 10). Statistical significance levels are indicated as p < 0.0001 (****).

6.2.2 Contraction inhibition altered the EHT morphology

To investigate the structural changes due to contraction inhibition, we analysed sarcomere organization in EHTs cultured for 28 or 70 days respectively. Following a 7-day treatment, immunostaining of phalloidin (I-band), titin (M-band), and α-actinin (Z-disc) revealed disorganized sarcomere structure. Quantitative analysis was performed using SarcAsM (Härtter et al., 2025) on alpha-actinin stained sections. The parameter Z-length (the length of the detected Z-bands by the tool) was chosen as it was the most sensitive parameter to quantify the changes in sarcomere structure (9-

12 EHTs from three independent CM batches). Notably, all sarcomere proteins were observed in all EHT sections, indicating that the proteins were not fully degraded. The beating EHTs (either control or washout) presented Z-lengths of ~1.3 µm, in both short-and prolonged-maturation groups. On the other hand, the Z-length of the treated EHTs in the short-maturation group was 0. 6 µm ± 0.09, while in the prolonged-maturation group it was 0.7 µm ± 0.1.

Furthermore, I studied nuclear shape. The nuclei in the treated EHTs were more circular than the nuclei of the beating EHTs (1 represents fully circular nuclei in the analysis). For the short-maturation EHTs, the circularity in the treated EHTs was 0.92 ± 0.01 compared to 0.89 ± 0.01 in the beating control and 0.9 ± 0.01 in the recovered EHTs. Similar results were found with the prolonged-maturation EHTs, where circularity was 0.91 ± 0.01 in stopped PSAM EHTs and 0.88 ± 0.01 for control and wash in the beating EHTs (**Fig. 6.12).**

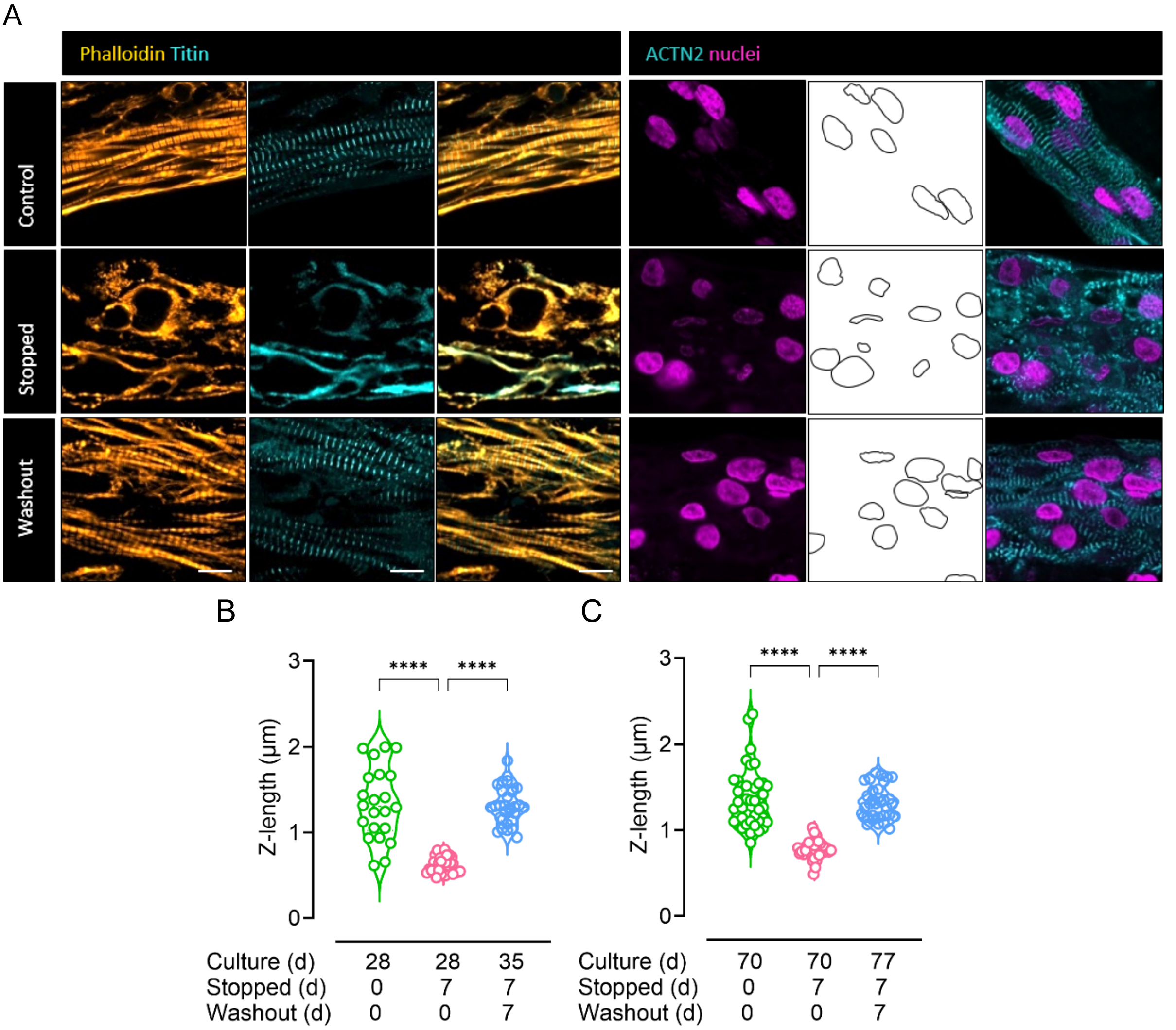

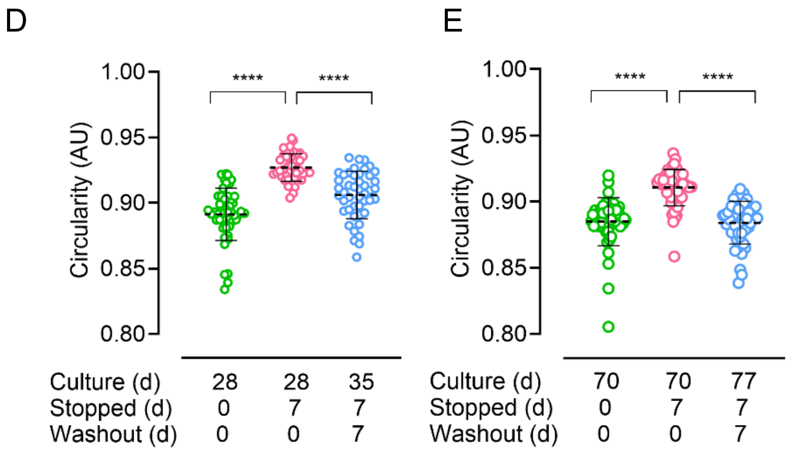

Figure 6.12 Disassembled sarcomeres and circular nuclei in treated PSAM EHT

(A) *Representative images from EHT sections for sarcomeric proteins and nuclear morphology in beating (control d70), treated (stopped d70), and recovered (washout d77) EHTs.* ***(B-C)*** *Violin plots of the sarcomere z-length analyzed in short- and prolonged-maturation EHTs.* ***(D-E)*** *Dot plots of nuclear circularity analyzed in short- and prolonged-maturation EHTs. Statistical significance levels are indicated as $p < 0.0001$ (****).*

6.2.3 Contraction inhibition did not lead to cell death

To verify that the loss of contraction in PSAM EHTs treated with PSEM^{89S} did not lead to cell death, we assessed DNA fragmentation using a TUNEL assay. The analysis revealed comparable levels of cell death in control and treated EHTs **(Fig. 6.13).**

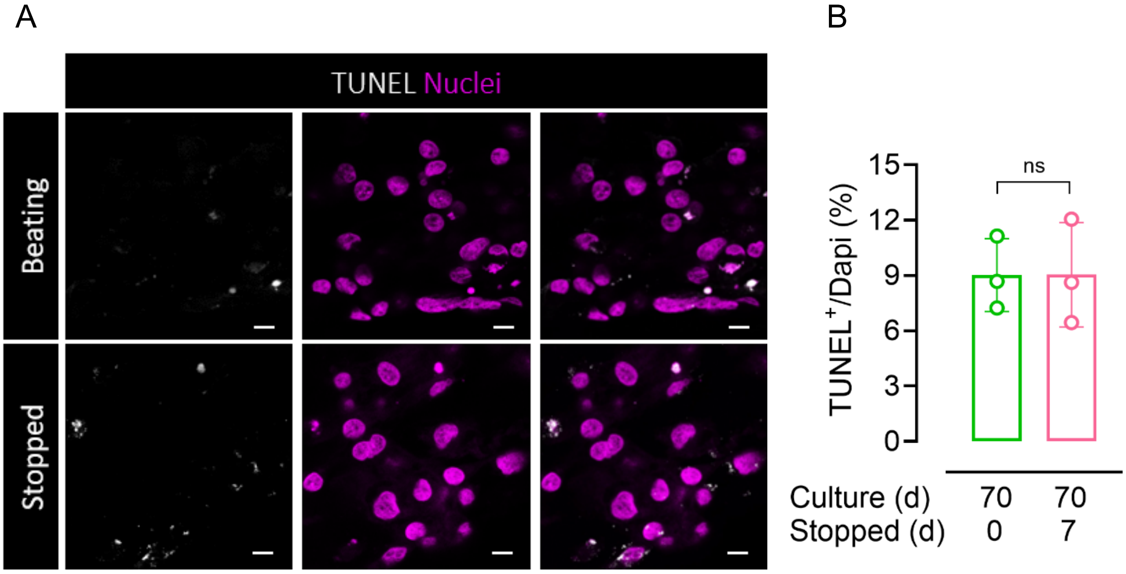

Figure 6.13 Cell death was not elevated in treated EHTs

(A) *Representative images from beating control and stopped EHTs after 63 days of maturation.* ***(B)*** *quantitative analysis showing comparable percentage of TUNEL$^+$ nuclei.*

6.2.4 Contraction inhibition stimulated CM cell cycle activity

Cell cycle activity in control EHTs was first assessed using Ki67 immunostaining at different time points. During this period, the percentage of Ki67$^+$ CMs declined progressively (5.8% ± 2.5 at day 14, and 1.2% ± 0.4 at day 88), consistent with literature reports that maturing CMs gradually lose their proliferative capacity **(Fig 6.14).**

Next, EHTs subjected to PSEM^{89S} after a short maturation period (21 days) were analysed. Treatment for 1, 7 or 21 days resulted in elevated Ki67 expression, indicating higher cell cycle activity. Only one day of contraction inhibition was sufficient to increase the percentage of Ki67$^+$ cells to 10.53% ± 2.5 compared to 4.5% ± 2.9 in beating control EHTs. Similar results were observed with a 7-day and 21-day treatment respectively. Contraction re-initiation resulted in a decline of cell cycle activity (5.5% ± 2.5).

Moreover, EHTs matured for prolonged period (63 days) which showed low baseline Ki67 expression (0.9% ± 1) revealed similar results. A 7-day contraction inhibition in this context induced significant increased Ki67 expression (4.5% ± 2.7), whereas the restoration of contraction led to a subsequent decrease (0.8% ± 0.3) **(Fig. 6.15).**

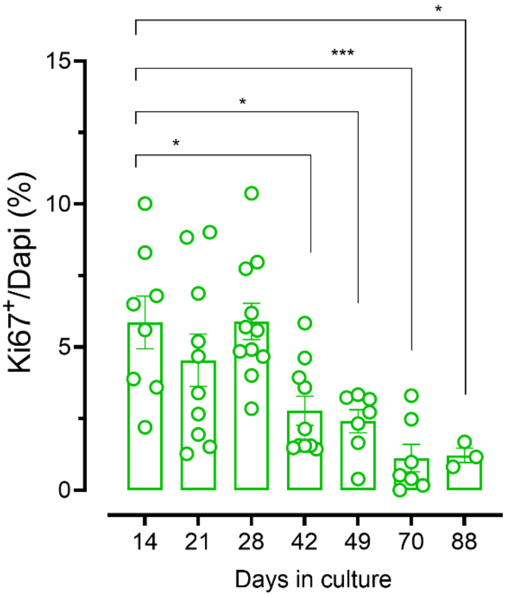

Figure 6.14 The percentage of Ki67$^+$ nuclei decreased over cultivation time in control EHTs

Bar graph representing the percentage of Ki67$^+$ nuclei in untreated PSAM EHTs cultured over time. A significant decline in Ki67 expression was first detected at the 42 days timepoint.

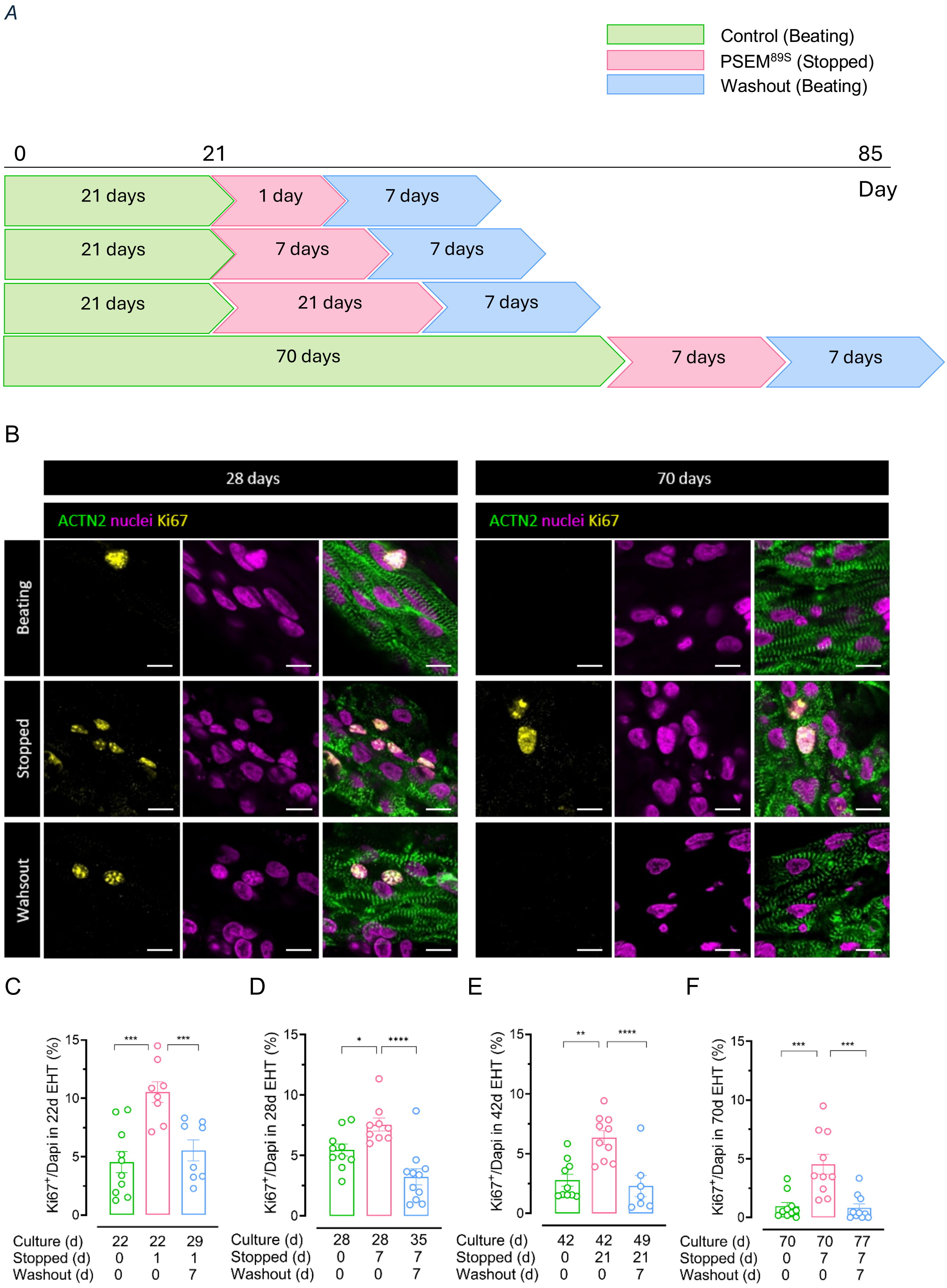

Figure 6.15 Increased cell cycle activity upon contraction inhibition with PSEM^{89S}

***(A)** Experimental timeline illustrating 1, 7 and 21 days of contraction inhibition in 21-day matured EHTs and 7 days of contraction inhibition in 63-day matured EHTs. For recovery, 7 days of drug washout was applied. **(B)** Representative images from 28d and 70d EHTs displaying the changes in cell cycle (Ki67) and sarcomeric assembly (α-actinin). Scale bar 20 µm. **(C-F)** Quantification of Ki67 was performed in 3 independent EHT batches. Statistical analysis was performed using one-way ANOVA. Significance levels: $p < 0.05$ (*), $p < 0.01$ (**), $p < 0.001$ (***), $p < 0.0001$ (****).*

Next, I was intrigued to evaluate the effect of contraction inhibition on EHTs from day 0, the day of casting the EHTs. Ki67 levels were elevated in EHTs treated with PSEM^{89S} for 14 days (treated: 8.93% ± 4 vs control: 5.86% ± 2.6), 21 days (treated: 8.7% ± 3.2 vs control: 4.5% ± 2.9), or 42 days (treated: 5.58% ± 1.5 vs control: 2.77% ± 1.6) compared to respective controls. Upon re-initiation of contraction, Ki67 expression returned to control levels or dropped even lower. Continuous inhibition for 63 days from day 0 was excluded from the analysis, as the EHTs did not survive under these conditions **(Fig. 6.16).**

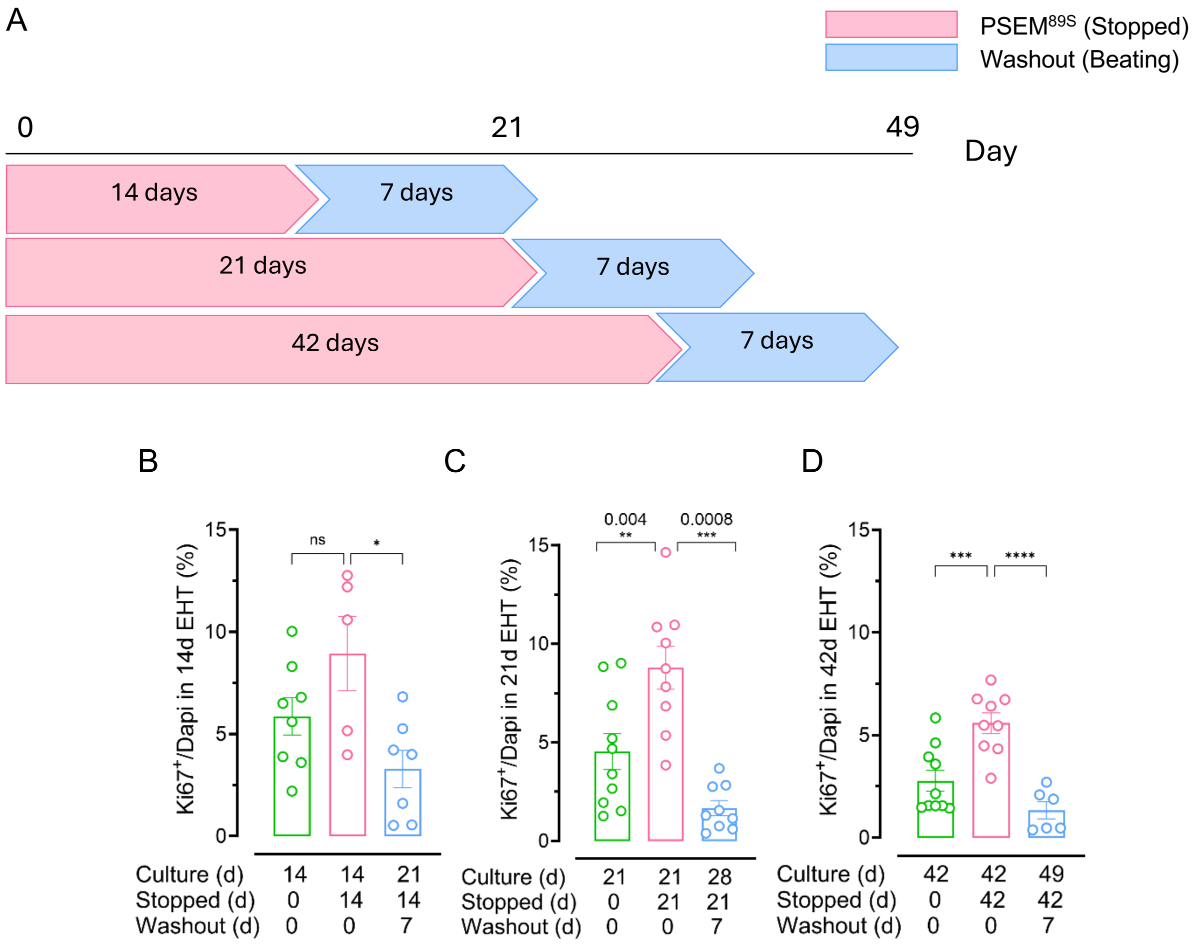

Figure 6.16 Early onset contraction inhibition with PSEM^{89S} (d0) led to higher cell cycle activity
***(A)** Experimental timeline illustrating contraction inhibition in EHTs treated from day 0 for 14, 21, or 42 days followed by 7 days washout period. **(B)** Higher percentage of Ki67^{+}nuclei in 14 days stopped EHTs*

from two independent biological batches compared to beating EHTs (control and washout), however non-significant. ***(C-D)*** *EHTs from 3 independent biological batches stopped for 21 or 42 days from day 0 revealed significant increase in Ki67*$^+$ *nuclei percentage compared to control and washout groups. Statistical analysis was performed using one-way ANOVA. Significance levels:* $p < 0.05$ *(*),* $p < 0.01$ *(**),* $p < 0.001$ *(***),* $p < 0.0001$ *(****).*

As Ki67 is a general marker of cell cycle activity rather than a direct indicator of proliferation, we also stained for PH3, which marks cells during G2-M transition, Similar results as for Ki67 were observed with PH3 staining. For PH3 quantification, 10 images were collected per section compared to 4-5 images per section for Ki67 analysis, as the number of PH3$^+$ nuclei was much lower. α-actinin was used as a counterstain, confirming sarcomere disassembly upon treatment. Data were obtained from three independent biological batches across two experimental groups: (i) 7 days of treatment after 21 days of maturation, and (ii) 7 days of treatment after 63 days of maturation. For the 21-day maturation group, the percentage of PH3$^+$ nuclei in treated EHTs were 0.25% ± 0.11 vs. 0.13% ± 0.03 in beating controls. Contraction re-initiation led to a decline to 0.12% ± 0.04. Similarly in the 63-day maturation group, contraction inhibition increased PH3 expression from 0.02% ± 0.02 in beating control EHTs to 0.3% ± 0.14 in stopped EHTs. Contraction-re-initiation subsequently resulted in a decline (0.05% ± 0.04 in washout; **Fig. 6.17**).

A

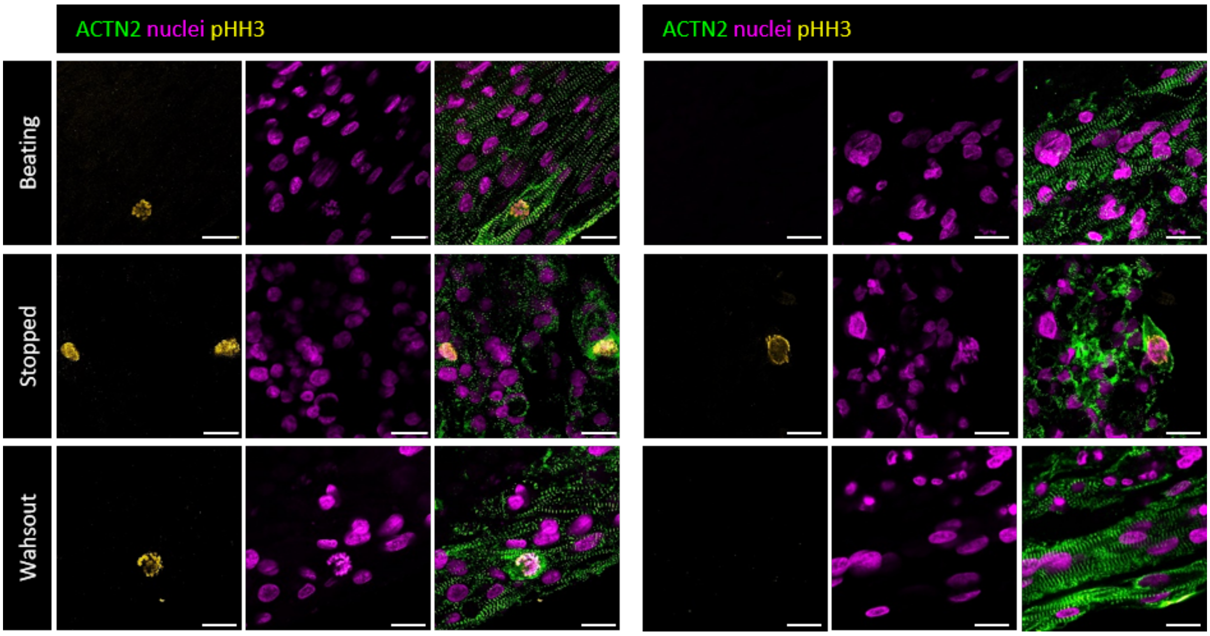

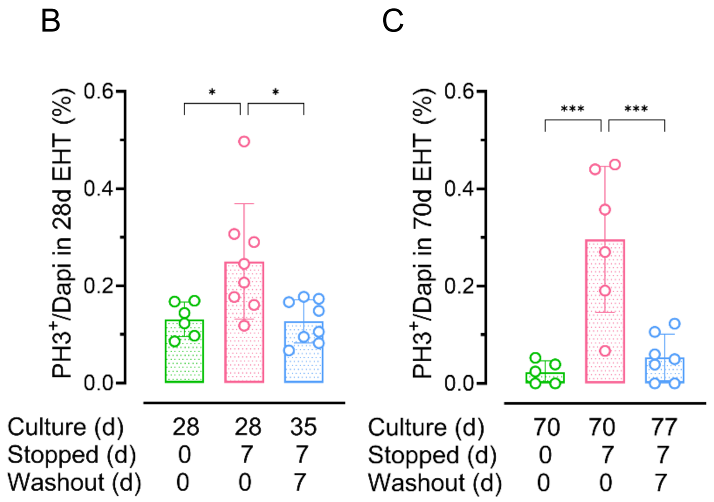

Figure 6.17 Increased PH3$^+$ nuclei in PSEM^{89S}-silenced EHTs

(A) *Representative images for PH3, α-actinin and Dapi in PSAM EHTs with either short or long maturation periods, that were treated for 7 days followed by a 7-day washout period.* ***(B-C)*** *Quantification of PH3$^+$ nuclei in short- and prolonged-maturation EHTs from three independent biological batches. Statistical analysis was performed using one-way ANOVA. Significance levels: $p < 0.05$ (*), $p < 0.001$ (***).*

6.3 Adult heart slices transduced with AAV expressing PSAM4

Building on the findings from the 2D CM experiments and the EHTs experiments, we next tested the response in a system with terminally differentiated myocytes – the adult human heart. For this, our collaborators at TUM, led by Dr. Poch, cultured human heart slices in a MyoDish system (InvitroSys) and transduced them with an AAV6 expressing TnT-nls-TagRFP-2A-PSAM4-GlyR construct to enable chemogenetic control of contraction. The construct contained RFP to allow the analysis of successful transduction. Contractile force was recorded continuously. After 7 days from the virus application, PSAM4 expression was confirmation using the RFP signal. Four slices were used per group. The transduced heart slices were treated with varenicline (100 nM) for 7 days, on the contrary, the control slices did not receive the virus nor the drug. During the 7 days of treatment, the force generated by the treated human slices was lower than the untreated controls reaching ~ 1 mN in treated slices vs. ~2 mN in control slices (**Fig. 6.18**). Following treatment, slices were cryo-sectioned and stained for cTnT, PH3, anti RFP and Dapi. The overall transduction efficiency (RFP-positive CM/total number of CM) was 7.3% ± 2, likely explaining why contraction did not stop entirely. PH3 expression was higher in the PSAM-treated samples. In details, PH3$^+$

nuclei in all analysed CMs (either transduced or not) were significantly higher in the treated slices (8.3% ± 4) compared to control (0.9% ± 0.7). When only the transduced CMs (which are absent in the control group) were evaluated, $PH3^+$ nuclei were 53% ± 16.3 of RFP^+ CMs. RFP^- (non-transduced) CM, expressed more $PH3^+$ in treated slices (4% ± 2.9) compared to control (0.9% ± 0.7) RFP^- CMs (**Fig. 6.19).**

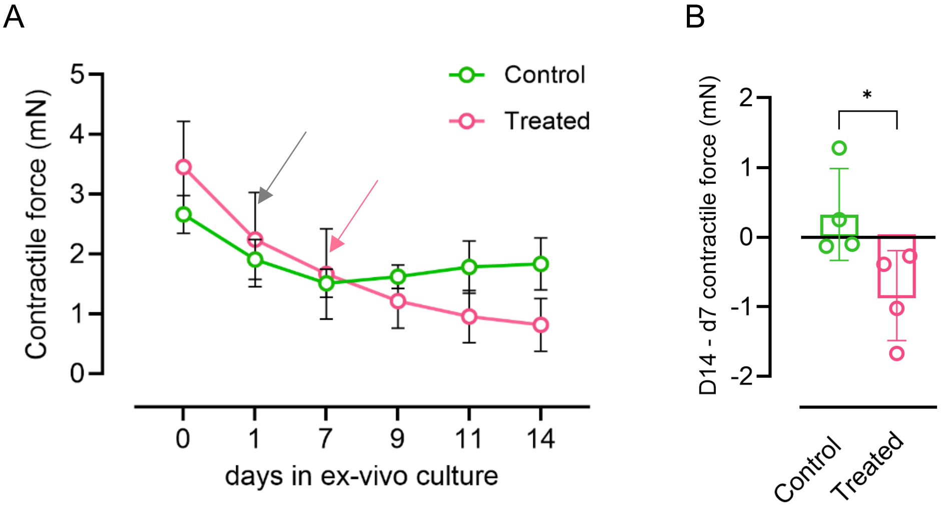

Figure 6.18 PSAM4-transduced heart slices showed a drop in force when treated with varenicline in comparison to control

(A) *Time course of contractile force (mN) in control (green) and transduced treated (pink) myocardial slices over 14 days in ex-vivo culture. Data are presented as mean ± SEM. Grey arrow represents onset of transduction, and pink arrow represents onset of treatment with varenicline.* ***(B)*** *Difference in force between day 7 and 14. Treated slices showed a significant reduction in force (-0.83 mN ± 0.6) compared to controls (+0.32 mN ± 0.65), mean ± SD. Statistical analysis was done using Student's t-test. Significance level:* $p < 0.05$ *(*).*

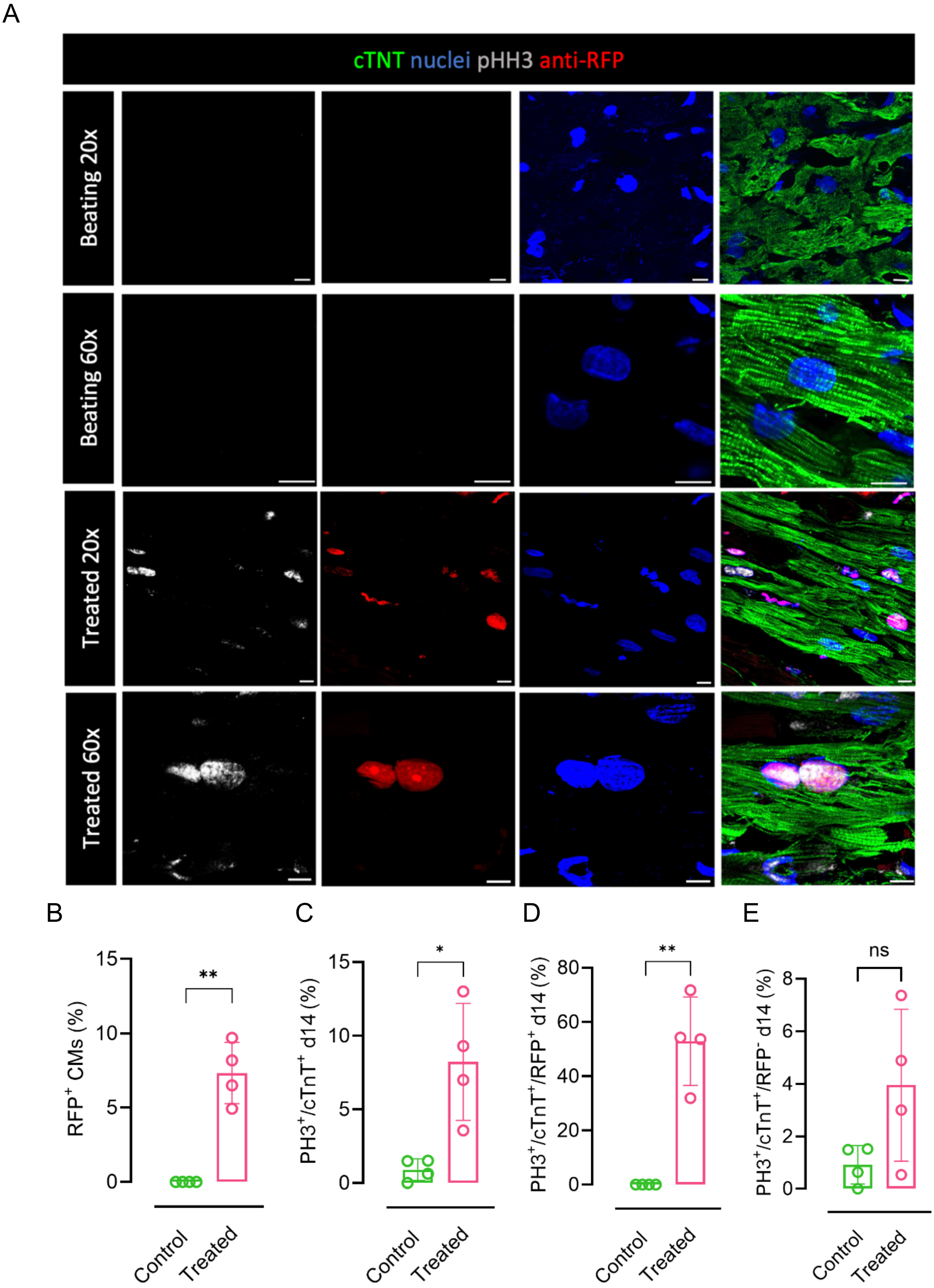

Figure 6.19 Higher cell cycle activity in the treated PSAM4-heart slices

(A) *Representative images showing elevation in PH3⁺ nuclei at a high and low magnifications.* ***(B)*** *Transduction efficiency indicated by RFP⁺ nuclei%.* ***(C-E)*** *PH3⁺ CM in PSAM4-transduced and non-*

transduced CM. Statistical analysis was done using Student's t-test. Significance level: $p < 0.05$ (*) and $p < 0.01$ (**).

6.4 Pharmacological inhibition of wild type EHTs

To this point, I have been testing the "all work, no repair" hypothesis with PSAM-expressing models, including PSAM EHTs, PSAM4 IPSC-CM and PSAM4-expression in adult human heart slices. To evaluate whether the observed effects were particularly due to inhibition of contraction rather than the inhibition of excitability via the depolarization block, I pharmacologically inhibited contraction in wild-type EHTs with the myosin inhibitor mavacamten. A supratherapeutic concentration (10 µM) completely abolished contraction. It took up to 30 minutes for contraction to fully cease at this concentration, and after 7 days of inhibition, drug removal did not trigger rapid recovery, but it required more than 22 hours for the EHTs to regain any contractile activity. Analysis of the non-contracting EHTs revealed a higher percentage of Ki67$^+$ nuclei (5.9% ± 1.9 vs 2.8% ± 2.2 in control), and of PH3$^+$ nuclei (1.0% ± 0.2 vs 0.2% ± 0.1 in control), indicating increased cell cycle activity. Sarcomere alignment was also assessed and found to be disassembled (0.6 µm ± 0.1 vs 1.3 µm ± 0.2 in control). Nuclei quantification was performed using StarDist and sarcomere analysis with SarcAsM, across three independent biological batches. Importantly, clinically relevant concentrations of mavacamten (0.3 µM and 0.7 µM) were also tested. While these concentrations did not abolish contractions, they reduced the generated force. Ki67 analysis and sarcomere assembly analysis were performed on two independent biological batches and revealed that as the contraction decreased, the sarcomere assembly concomitantly decreased, and the cell cycle activity increased **(Fig. 6.20)**.

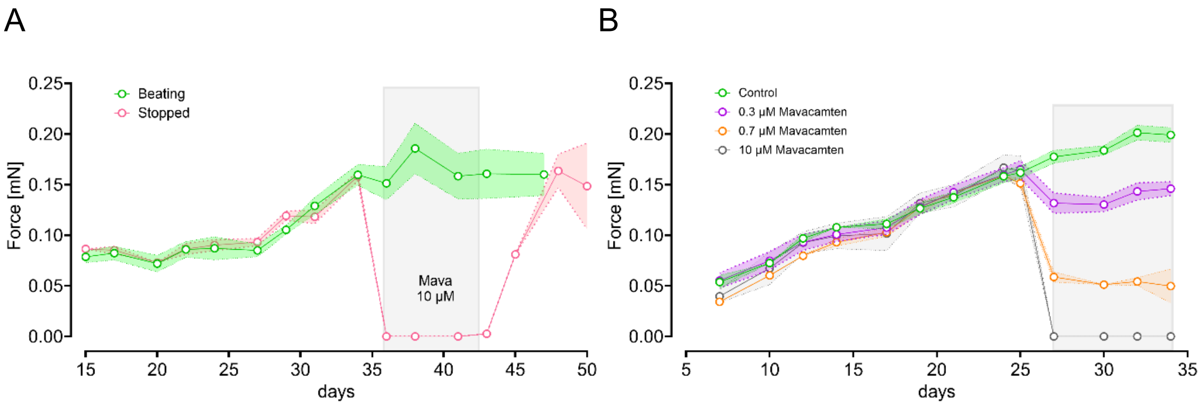

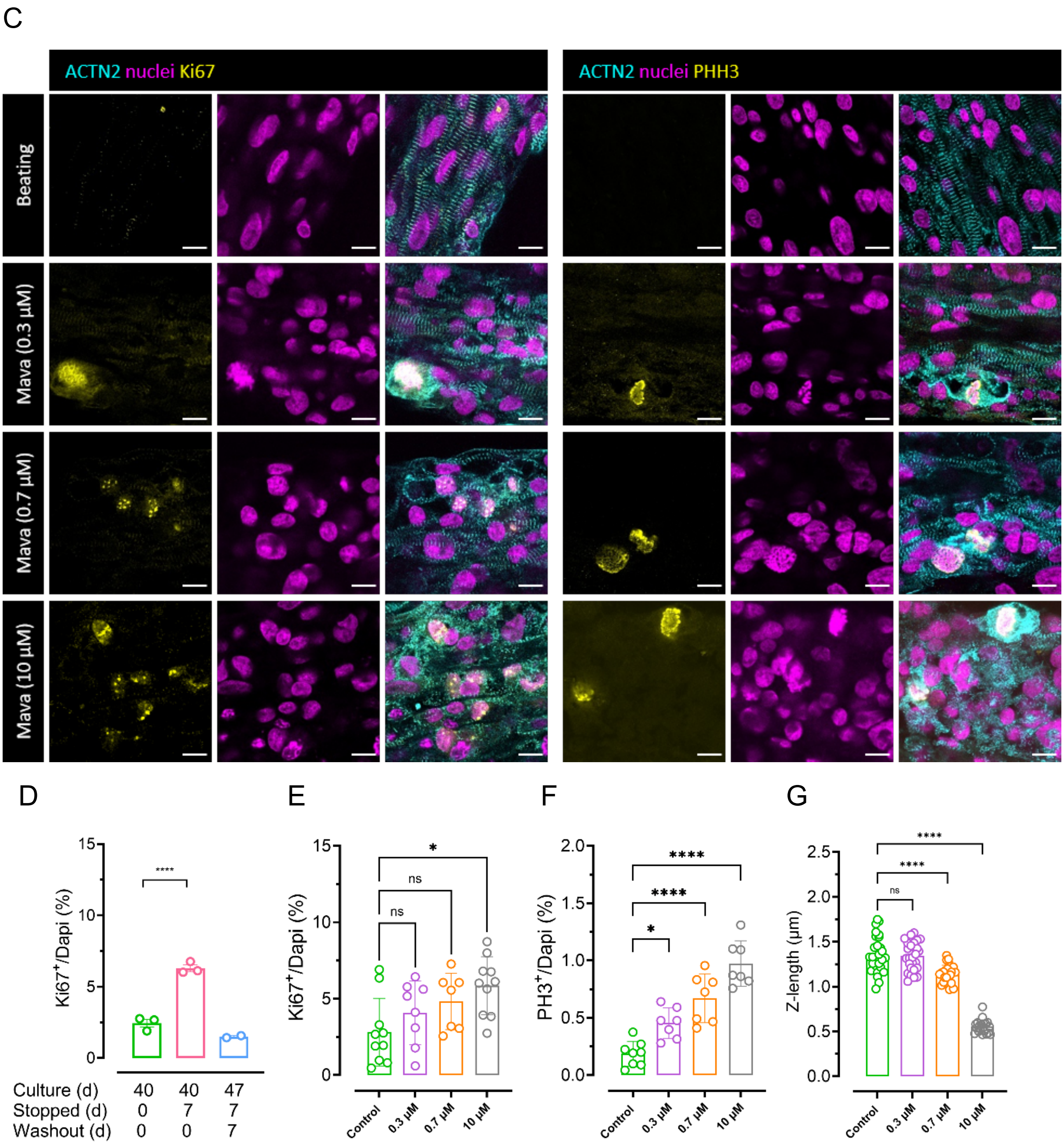

Figure 6.20 Pharmacological inhibition of contraction led to higher Ki67 and PH3 expression in a concentration-dependent manner

(A) *Force measurements in wild type EHTs (ERC001) treated with mavacamten (10 µM) showing complete force inhibition, with the ability to recover after drug removal.* ***(B)*** *Concentration-response curve including therapeutic concentrations of mavacamten.* ***(C)*** *Representative images of ERC1 EHTs treated with different concentration of mavacamten stained for Ki67, α-actinin, and Dapi. Scale bars 20 µm.* ***(D-G)*** *Quantification of cell cycle markers and sarcomere structure using one-way ANOVA. Significance level: $p < 0.05$ (*), $p < 0.001$ (***) and $p < 0.0001$ (****).*

6.5 Dissection of the underlying mechanism

6.5.1 Proteomics analysis

Having consistently observed an increase in cell cycle activity upon contraction inhibition across all experimental models, it became essential to investigate the underlying mechanism(s). To this end, we first employed omics-based approaches, including proteomic profiling of EHTs and 2D CM, as well as bulk RNA sequencing in 2D CMs.

Proteomic analysis revealed a global decrease in sarcomeric proteins abundance. Subsequent gene set enrichment analysis (GSEA) of the proteomics data identified in the KEGG (Kyoto Encyclopaedia of Genes and Genomes) database an upregulation in cell cycle related pathways, while pathways associated with cardiac function, glycolysis, OxPhos, and cell-cell contact were significantly downregulated. The Gene Ontology (GO) biological processes analysis further indicated elevation in DNA replication proteins in the treated EHTs and CM, in agreement with our previous observations. However, no single candidate pathway to be the main driver of the observed phenotype stood out, encouraging further investigation through transcriptomic profiling **(Fig. 6.21, Fig. 6.22).**

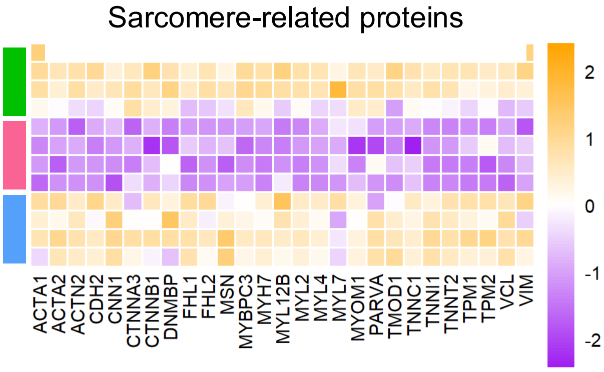

Figure 6.21 Differentially expressed sarcomeric proteins in treated PSAM EHTs were significantly lower compared to beating EHTs

Normalized sarcomeric proteins expression levels in control (green), treated (pink), and washout PSAM EHTs. EHTs were matured for 21 days, followed by 7 days treatment and 7 days washout. All sarcomeric proteins in treated stopped EHTs were down regulated compared to beating EHTs as represented by the heatmap.

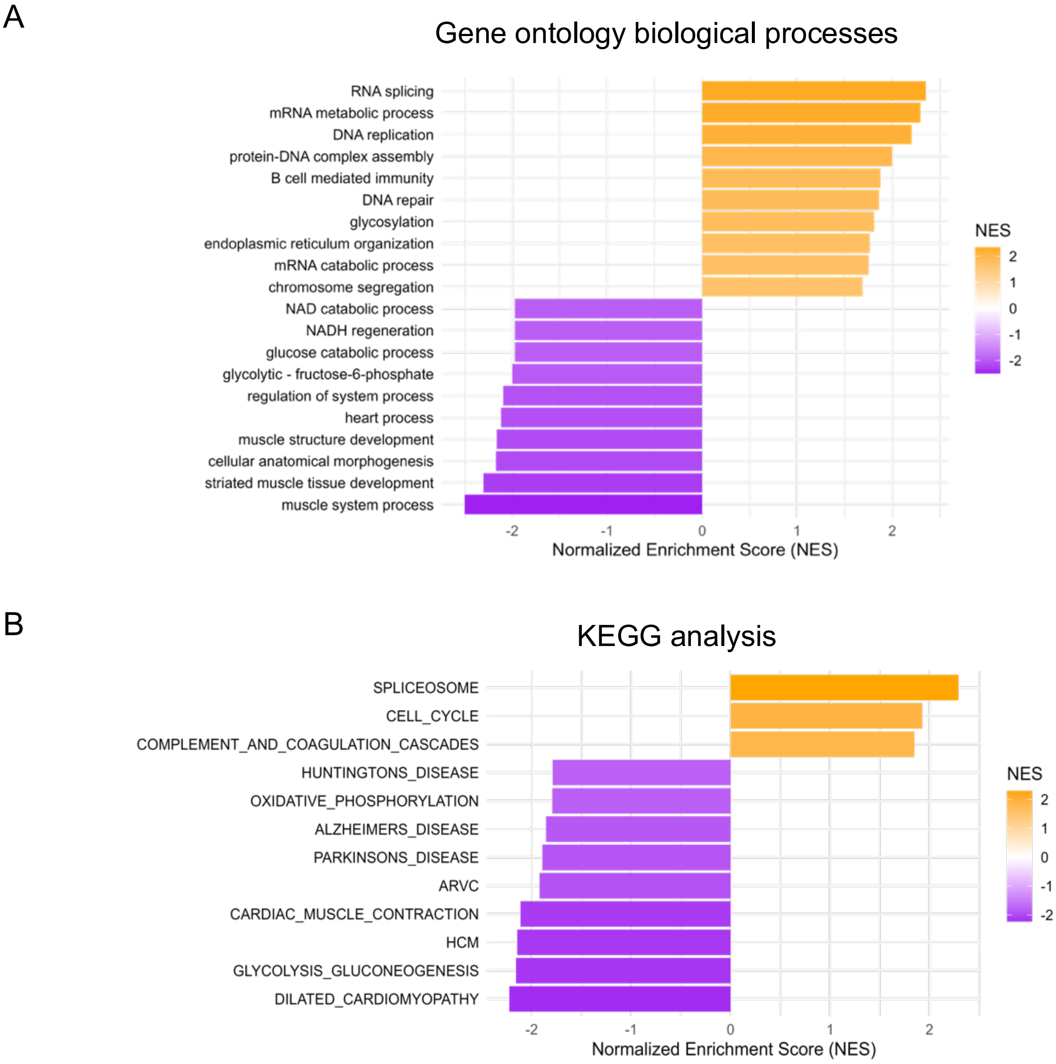

Figure 6.22 GSEA outcome in treated cardiomyocytes compared to control

(A) *The upregulated biological processes included DNA replication and chromosome segregation (i.e. signs of cell division).* ***(B)*** *KEGG analysis showed cell cycle pathways to be upregulated (orange) and heart related pathways and OxPhos to be down regulated in stopped PSAM4 CMs proteomics analysis.*

6.5.2 Bulk RNA sequencing

RNA sequencing results largely mirrored the proteomic findings in terms of the main patterns, yet provided additional layers of information that allowed for a more refined mechanistic interpretation. Differential expressed genes (DEG) of treated CMs (maturation for 21 days and treated for 7 days) revealed downregulation of (i) sarcomeric genes, (ii) oxidative phosphorylation / electron transport chain genes and (iii) glycolysis genes. As for the up regulated genes, it included cell cycle, cell division, nuclear division and notably, cell-cell contact genes **(Fig 6.23).**

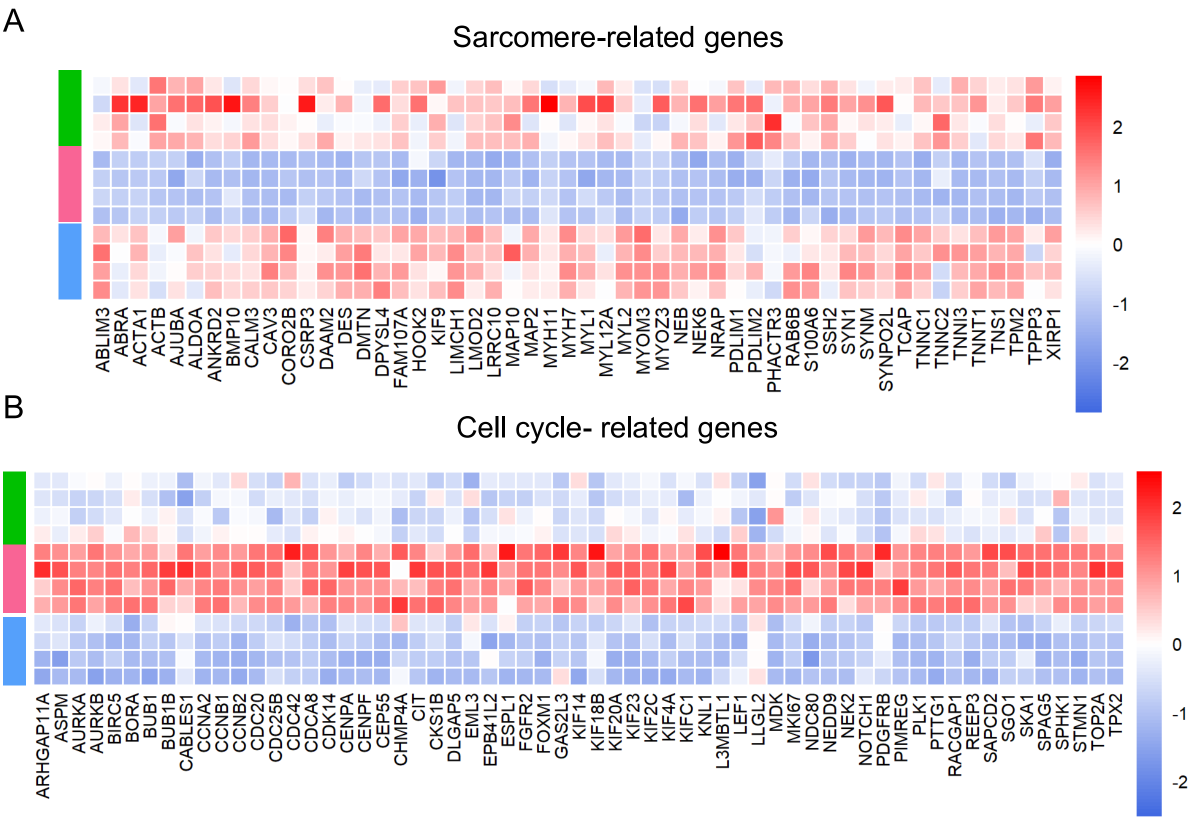

Figure 6.23 Sarcomere- and cell cycle- related genes based on the GSEA displayed opposing expression patterns

*(**A**) The normalized gene expression of sarcomere related genes was reduced, and (**B**) the gene expression of cell cycle related genes was elevated in treated (pink) cardiomyocytes compared to beating control (green) and re-initiated washed group (blue).*

Interestingly from the transcriptomic data, CMs maturation markers were analysed to inspect the maturation state of treated CMs. Four gene expression ratios were examined: MYH7/MYH6, TNNI3/TNNI1, MYL2/MYL7, and MYL3/MYL4. Although the individual genes were all down regulated, the ratio analysis revealed that as contraction was inhibited, CMs shifted towards a more immature state **(Fig. 6.25)**.

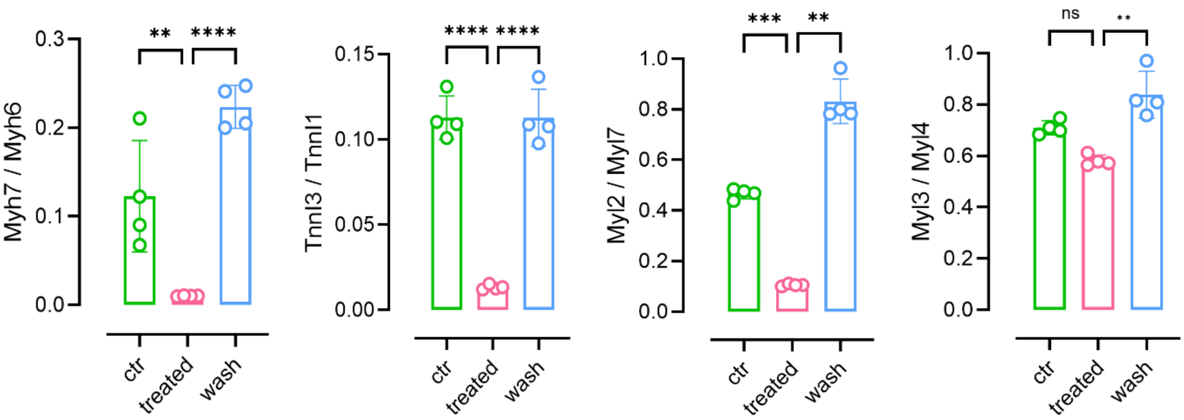

Figure 6.24 Stopped CMs shifted to an immature state

Maturation markers were downregulated in treated CMs when compared to beating CMs. Statistical significance was obtained using one-way ANOVA. Statistical levels: p < 0.01 (**), p < 0.001 (***), p < 0.0001 (****).

To further interpret the transcriptomic changes, GSEA was applied, which suggested an overall downregulation in sarcomere-related genes and upregulation in cell cycle related genes among other changes. Gene ontology analysis of biological processes highlighted two dominant patterns. First, there was a strong downregulation linked to contractile and metabolic functions. In parallel, there was an enrichment of processes associated with cell division and tissue remodeling, such as nuclear division, mitotic chromatid segregation and mesenchyme development. Complementary pathway analysis using Wiki-Pathway revealed Hippo signalling pathway, raising the possibility of a Hippo-YAP-mediated effect. Finally, transcription regulator analysis (TRA) identified distinct target genes (regulators) within the differentially expressed gene sets. These regulators represented candidates for knockdown or overexpression experiments to directly test their involvement in the observed increase in CM proliferation. Among these candidates were E2F1 (cell cycle activator) revealed by its upregulated target genes, while E2F6 (cell cycle inhibitor) and SRF, with their related target genes were downregulated. FOXM1 was as well detected among the transcription regulators whose related genes were upregulated **(Fig. 6.24).**

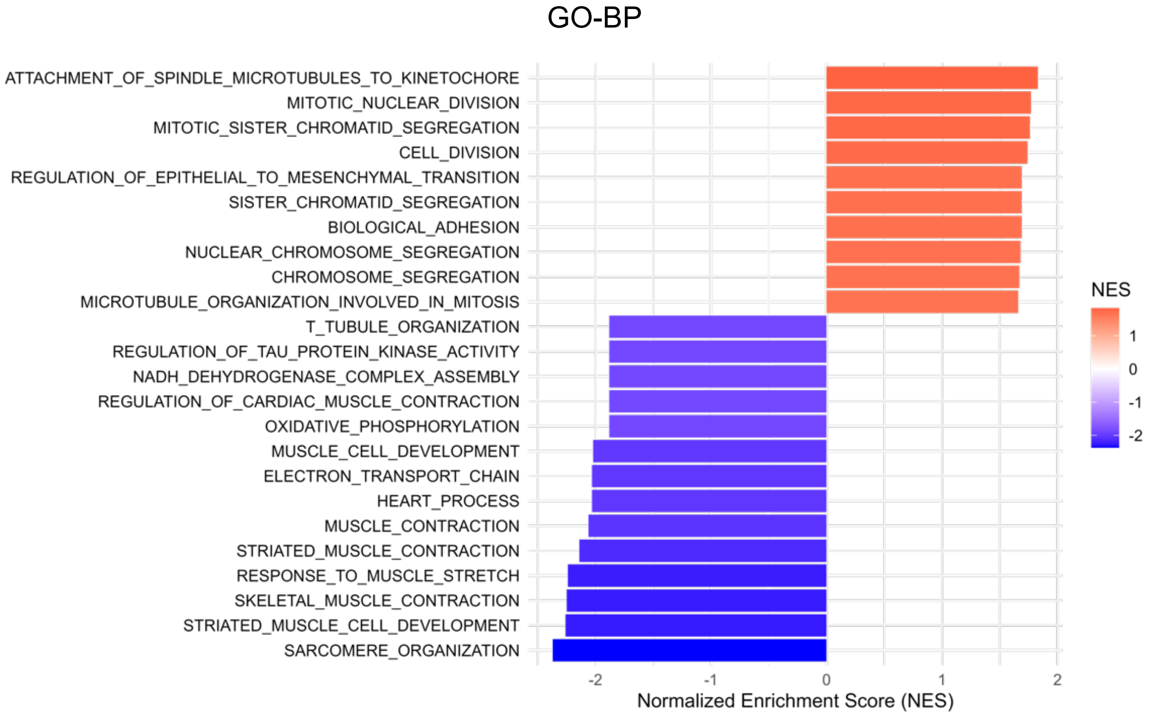

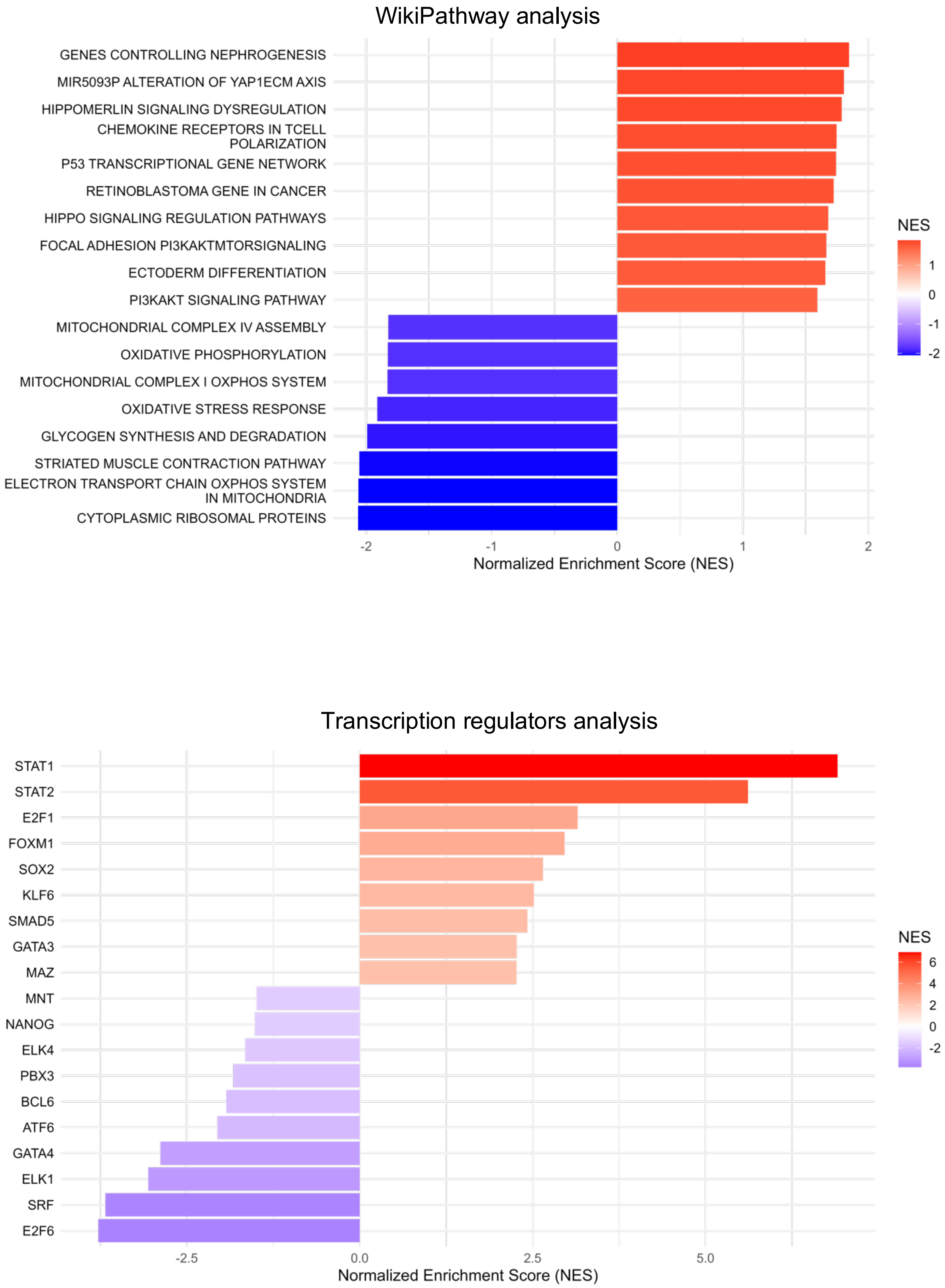

Figure 6.25 GSEA GO-BP, Wikipathways, and transcription regulators analysis confirm elevation in cell cycle-related processes and suppression in sarcomere-related processes.

6.5.3 G-actin/F-actin quantification

In addition to assessing sarcomeric protein abundance and gene expression, it was essential to examine actin dynamics. This analysis was particularly relevant because G-actin acts as a regulatory molecule, interacting with transcriptional cofactors and influencing signaling pathways, such as the SRF-MRTF axis. To address this, I separated G-actin from F-actin by ultracentrifugation (100,000 G) of the cell suspension for an hour to precipitate most of the proteins, keeping only the soluble ones (including G-actin) in the supernatant. The G-actin/F-actin ratio were quantified using western blot, with S6 ribosomal protein as a housekeeping protein for normalization. The results demonstrated that the G-actin/F-actin ratio was higher in treated PSAM4 CMs (0.67/0.33) than the control CMs (0.34/0.66; **Fig. 6.26**).

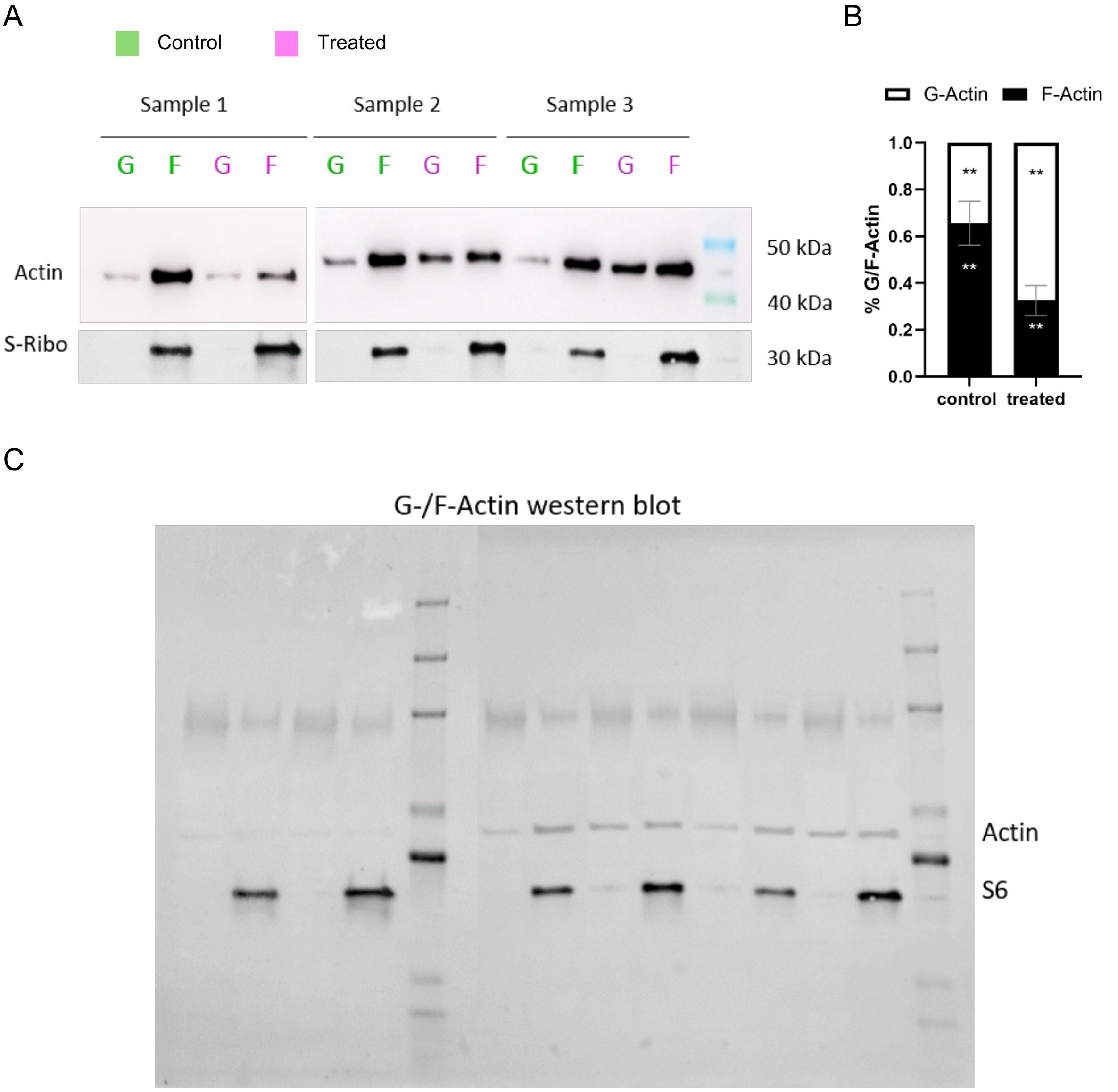

Figure 6.26 G-/F-actin ratio was elevated in treated PSAM4 CMs

***(A)** Representative WB showing G- and F- actin proteins at 43 kDa and ribosomal protein S6 at 29 kDa in control and treated PSAM4 samples. **(B)** Percentage of normalized actin fractions. Statistical significance using 2-way ANOVA, $p < 0.01$ (**). **(C)** Uncropped western blot membrane.*

6.5.4 YAP1 knockdown

YAP signalling is among the best-established pathways driving proliferation in CMs, and it was identified in our treated samples through WikiPathway analysis. I first targeted YAP1 with silencing siRNA in CMs and evaluated EdU incorporation in those samples using flow cytometry. To quantify the extent of YAP KD, qPCR was completed using cDNA from the test samples. Each experiment had 4 conditions; not exposed to anything (-/-), exposed to siRNA only (si/-), exposed to varenicline only (-/v), and exposed to both siRNA and varenicline (si/v).

In the first experimental run, varenicline treatment increased the EdU incorporation as expected, independent of the presence of the siRNA, which itself had no clear effect (Fig. 6.27). In details, si/v was 6.4% ± 0.5 and -/v was 5.8% ± 1, with no significant differences between them. In -/- samples, EdU incorporation was 3.4% ± 0.5, and in si/- samples, it was 2.5% ± 0.3. Unfortunately, RNA extraction was unsuccessful as the RNA was lost during isolation, preventing the assessment of YAP1 expression.

In the second experimental run, siRNA treatment in both si/- and si/v lowered EdU incorporation and abolished the stimulatory effect of varenicline. So, as anticipated, EdU% in control -/- was 4.8% ± 1.3 and increased to 6.7% ± 1.7 in -/v group. Exposure to siRNA showed that EdU incorporation in si/- group was 2.5% ± 0.4 and was 2.6% ± 0.6 in si/v group. RNA was successfully isolated, and cDNA was prepared for qPCR.

In the third experimental run, varenicline only stimulated EdU incorporation in the presence of the siRNA. EdU incorporation in si/- was in the same range to -/- and surprisingly to -/v groups (si/- was 2.3% ± 0.2, -/- was 2.4% ± 0.6, and -/v was 2.8% ± 0.2). CMs treated with both varenicline and siRNA (si/v) demonstrated significantly higher EdU incorporation; 3.7% ± 0.4. RNA was successfully isolated, and cDNA was prepared for qPCR.

For the qPCR results, cycle threshold (Ct) values were normalized to the reference gene GUSb (ΔCt). $\Delta\Delta$Ct from intervention samples (YAP1-siRNA treated, varenicline treated, or both) was calculated in relation to the control samples (-/-). Fold changes

(FC) was expressed as log2 (ΔΔCt). I included negative control (C_{Neg}) samples, RNA samples without exposure to reverse transcriptase (-RT), to check for genomic DNA contamination.

From batch 2, the -/v samples relative quantification revealed a high (>1) YAP1 expression. In the siRNA exposed groups, (si/v and si/-), there was relatively lower YAP1 expression. However, Unfortunately, Ct values from the C_{Neg} samples were close to the experimental samples Ct, suggesting genomic DNA contamination. Thus, the qPCR analysis was repeated by Grit Höppner (TA), who observed the same finding with the C_{Neg} Ct values, namely they were in the same range as the test samples. FC quantification revealed relative YAP1 knockdown in siRNA-treated (si/-) CMs, while the siRNA and varenicline-treated (si/v) CMs showed only a slight reduction in YAP1 expression when compared to varenicline only treated CMs (-/v).

From batch 3, qPCR analysis did not reveal YAP1 knockdown in my hands, However, when repeated by Grit, it yielded the opposite outcome; samples treated with YAP1-siRNA showed relatively lower YAP1 expression **(Fig. 6.27).** Overall, these experiments did not provide a clear result and need to be repeated with a more reliable method.

To further evaluate the role of YAP1 in our model, immunostaining for YAP was performed in 2D PSAM4 CM. During cardiac cell cycle arrest, YAP is phosphorylated and retained in the cytoplasm. Upon activation, it becomes dephosphorylated and translocates into the nucleus, regulating transcriptional programs, including those associated with cell proliferation. Accordingly, nuclear localization of YAP was assessed by colocalization analysis of anti-YAP staining with Dapi nuclear labeling, using Coloc2 plugin in Fiji. α-actinin was used as a counterstain. From one experimental batch (n = 3), the analysis revealed that contraction inhibition did not result in increased YAP nuclear translocalization. Colocalization was quantified with two parameters provided by Coloc2: Kendall's Tau-b rank correlation coefficient and Li's intensity correlation (ICQ) quotient **(Fig. 6.28)**.

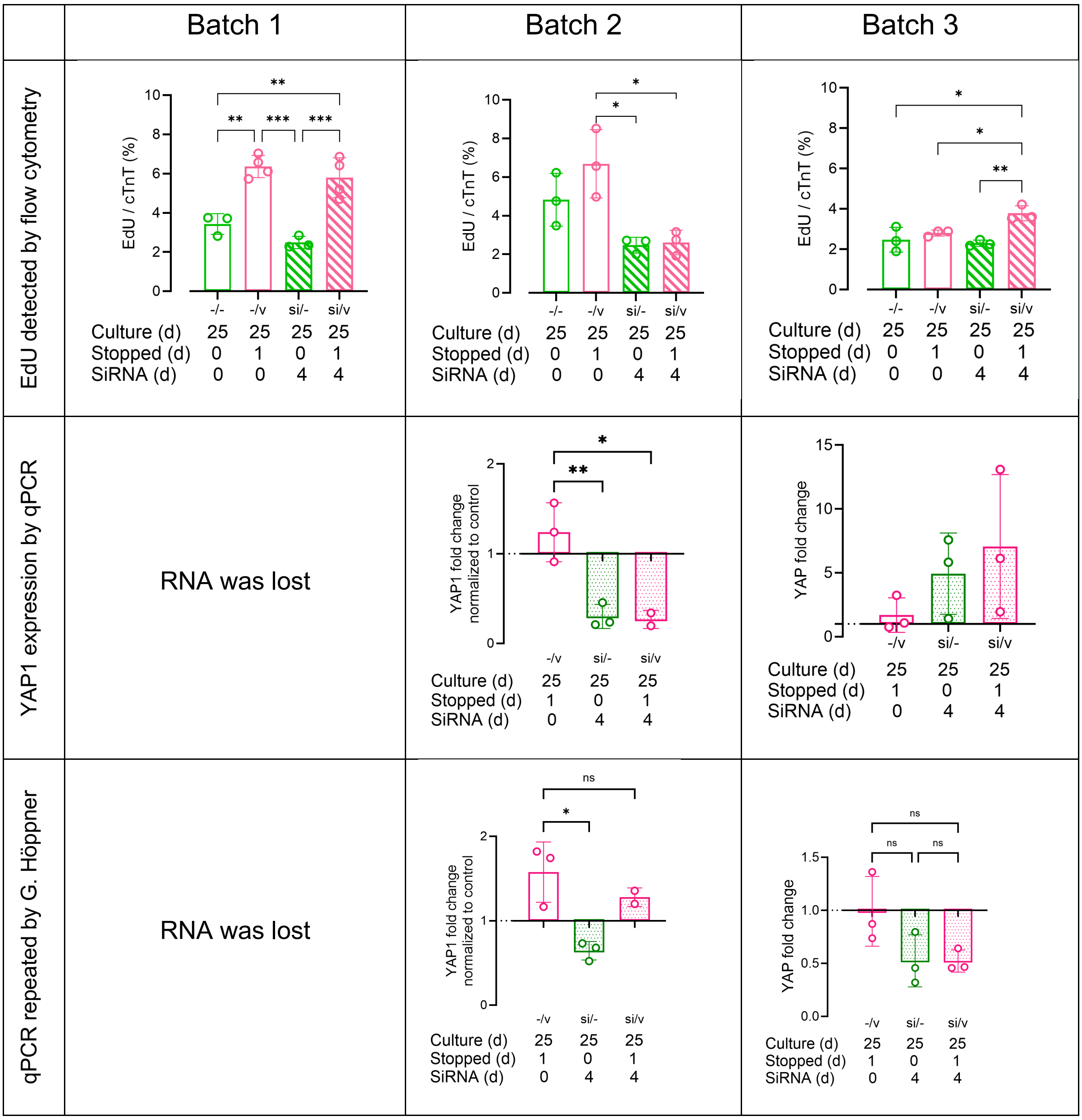

Figure 6.27 SiRNA YAP1 knockdown revealed inconsistent results

Statistical analysis was calculated using one-way ANOVA. Only significant results are displayed.

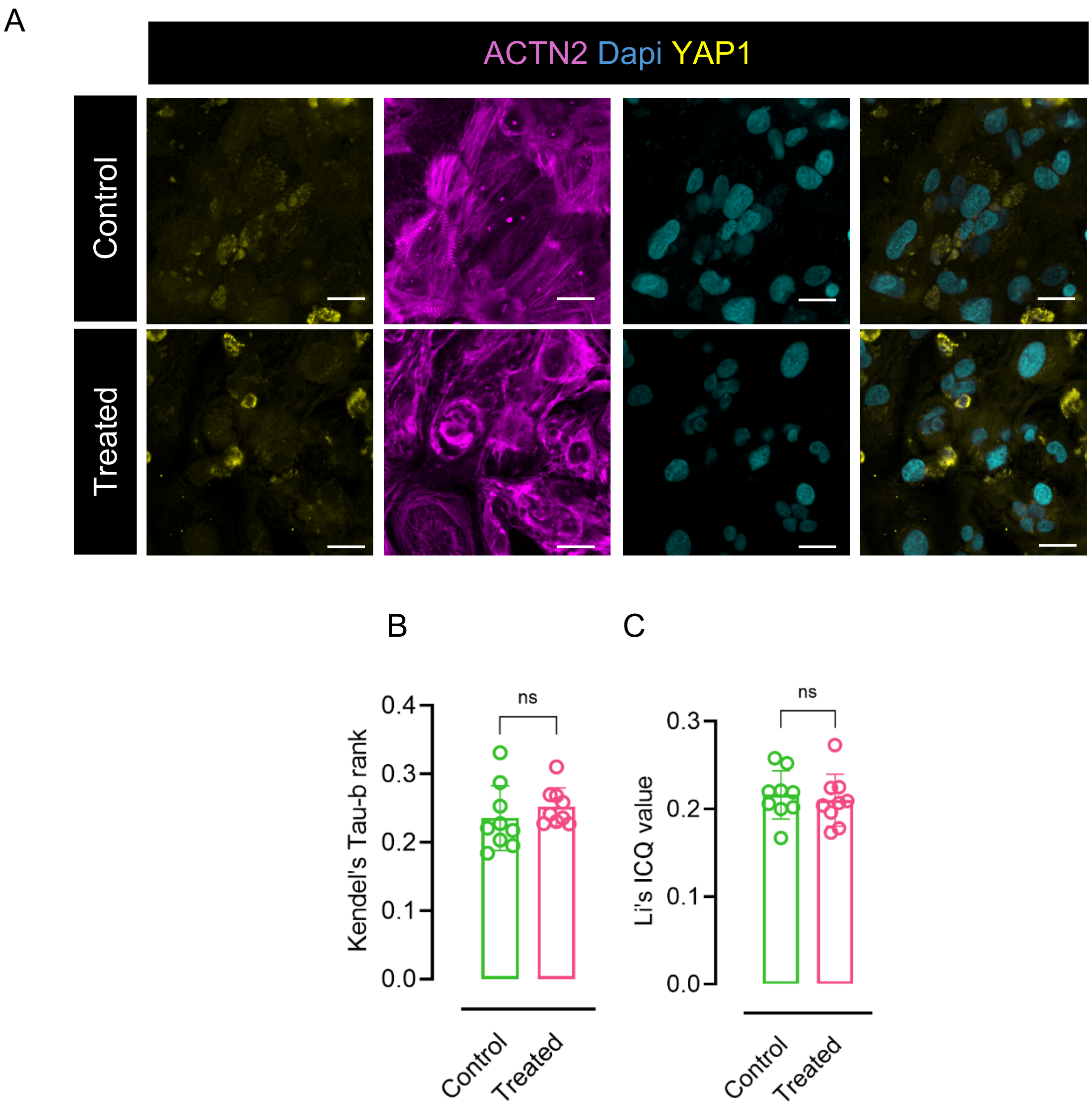

Figure 6.28 Anti-YAP1 staining did not reveal clear significant nuclear-translocalized YAP signal in treated and control PSAM4 CMs

(A) *2D PSAM4 CMs treated with varenicline for 7 days and control did not differ in YAP and Dapi colocalization signals. Scale bar: 20 µm.* ***(B-C)*** *Quantification of colocalization using Coloc2 parameters, Kendall's Tau-b rank correlation coefficient and Li's intensity correlation quotient (ICQ). Statistical significance was obtained using Student's t-test.*

6.6 Kinetics analysis for sarcomere disassembly and cell cycle activity

The temporal relationship between sarcomere disassembly and cardiomyocyte proliferation was evaluated to determine the sequence of events: whether proliferation initiates sarcomere disassembly or if sarcomere disassembly preceded and facilitated proliferation. With the help of Malena Zafra Castellano and Lucia Zamancona Gomez, we deployed PSAM4 CMs and cultured them for 21 days, then the medium was supplemented with varenicline for 1, 3, 6, 12 and 24 hours. Sarcomere organization was analyzed using SarcAsM and the nuclei were assessed using StarDist. The results revealed that sarcomere disassembly occurred several hours prior to a significant increase in Ki67 expression. Sarcomeres started to disassemble as early as 1 hour after the initiation of treatment while Ki67 increased only after 24 hours of treatment.

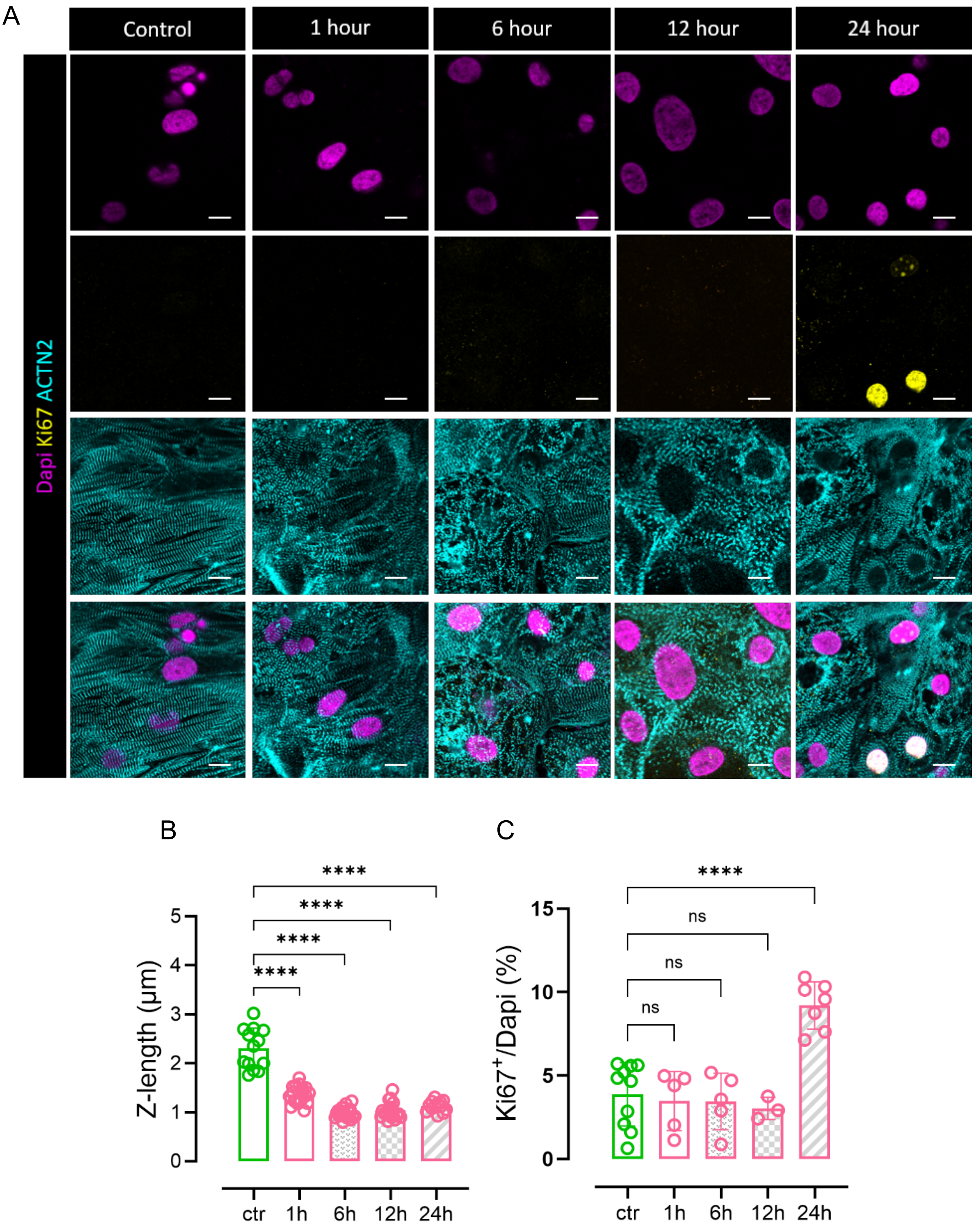

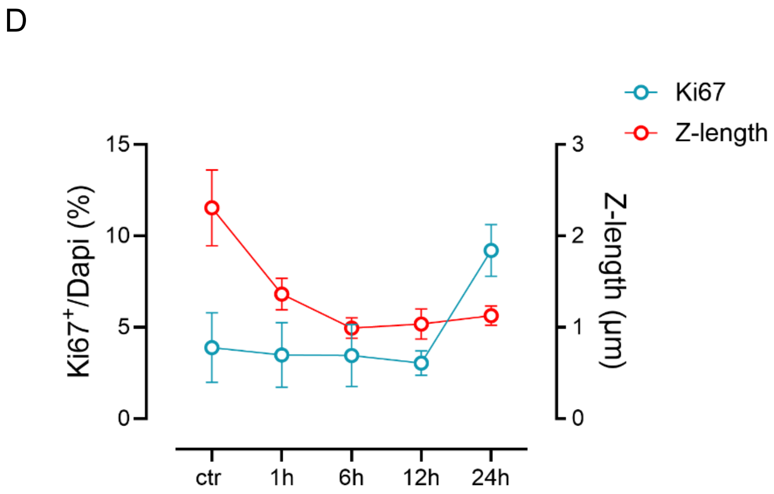

Figure 6.29 Sarcomere disassembly preceded CM proliferation

(A) *Representative images of PSAM4 CMs at 1, 3, 6, 12, and 24 hours stained with α-actinin for sarcomere visualization, Ki67 for cell cycle activity and Dapi as a counterstaining.* ***(B-C)*** *Quantification of sarcomere organization (using z-length parameter) and cell cycle activity over time.* ***(D)*** *Sarcomere disassembly, reflected by a decrease in Z-length, preceded the increase in Ki67 expression. Scale bars: 20 µm.*

7. Discussion

The adult heart contracts continuously (Siegel, 1968) and exhibits a very limited proliferative capacity (Bergmann et al., 2009; Senyo et al., 2013). A study by Ahuja et al., demonstrated that the few CMs that do undergo proliferation lacked organized sarcomeres (Ahuja et al., 2004). From these observations, we and other have inferred that cardiomyocyte proliferation is associated with sarcomere disassembly. However, this presents a physiological paradox: while sarcomere disassembly may permit proliferation, it simultaneously compromises the heart’s essential function of continuous contraction and systematic perfusion, thereby creating a fundamental barrier to regeneration. (Kennedy-Lydon & Rosenthal, 2017).

Building on this reasoning, **we hypothesized that transient cessation of contractile activity might enable CM to re-enter cell cycle**. To test this hypothesis, a model of transient CM contraction inhibition without inducing cell death was required. The absence of such a model was potentially contributing to the limited exploration of this hypothesis. Moreover, an opposing argument was the embryonic and early postnatal heart`s (up to 7 days) capability to regenerate and grow despite contracting. However, the embryonic heart differs markedly from the adult heart as depicted in the following table:

	Fetal heart/CM	Adult heart/CM
Hemodynamic Load and Circulatory Environment	Operates in a low-pressure, low-resistance circulation, as oxygen and nutrient exchange occur via the placenta rather than the lungs. The fetal systemic vascular resistance is low, and pulmonary vascular resistance is high (due to fluid-filled lungs).	Functions in a high-pressure, loss of placental perfusion thus high-resistance systemic circulation, with the left ventricle working against much higher afterload to sustain systemic perfusion (Heymann et al., 1981).
Oxygenation and Metabolic Demand	Receives oxygenated blood directly from the placenta with relatively low oxygen tension (20–30 mmHg). Fetal CMs rely more on glycolytic metabolism	Operates under higher oxygen tension (~100 mmHg in arterial blood) and relies predominantly on fatty acid oxidation for ATP production,

	and less on oxidative phosphorylation (Smolich et al., 1992).	supporting continuous high-energy demand.
Sarcomere Structure and Cytoskeletal Organization	Have immature, less organized sarcomeres, with more plastic cytoskeletal structures and fewer mature intercalated discs, enabling cell cycle activity and remodelling (Pettinato et al., 2022).	Possess highly organized, rigid sarcomeres, dense cytoskeletal networks, and strong mechanical coupling, which stabilizes structure but restricts remodelling and proliferation.
Extracellular Matrix (ECM) Composition and Stiffness	ECM is less stiff, more compliant, and highly dynamic, allowing structural plasticity (Notari et al., 2018; C.-C. Wu et al., 2020).	ECM becomes stiffer and more cross-linked, with increased collagen deposition, limiting cell division and migration.
Contractile Demand	Beats at a high rate but with lower force generation, as it operates under less demanding hemodynamic conditions (de Haan et al., 1971; Racca et al., 2016).	Requires high force and contractile output, which structurally reinforces sarcomere stability.

Together these factors indicate that the embryonic and early postnatal hearts have low workload, which may explain why embryonic/neonatal CMs can proliferate despite continuous beating, while the adult hearts remain largely incapable of regeneration. In this context, the iPSC lines expressing the chemogenetic tools, PSAM and PSAM4 developed by Tim Stüdemann provided an innovative means to modulate CM contraction in a fast and fully reversible manner.

Using PSAM- and PSAM4-expressing CM, we systematically tested our hypothesis in three experimental platforms: (i) 2D-CMs, (ii) 3D-EHT, and (iii) human adult ex vivo heart slices transduced with the chemogenetic channel. These experiments involved transiently arresting contraction for defined durations at various time points, followed by drug washout to restore beating.

7.1 2D PSAM4 CM

The first experimental platform employed was the 2D culture of PSAM4 CMs. Flow cytometry served as the primary analytical tool, enabling the quantification of cTnT levels in PSAM4 control, varenicline-treated, and treated then washed samples. It also enabled the quantification of EdU that was incorporated for the last 24 hours of culture and the assessment of DNA content via Hoechst staining. Three key findings emerged from this analysis. First, cTnT levels remained comparable between control, treated and washout groups, indicating that sarcomeric proteins were not degraded upon contractile arrest, but are preserved despite disassembly of the sarcomere structures. Second, EdU incorporation was significantly higher in treated (stopped) CMs compared to both control and washout (beating) conditions, suggesting higher DNA synthesis during arrest phase. Third, analysis of DNA content among the EdU^+ CM revealed an increase in the absolute proportion of ploidy states (more 2n, 4n, and 8n+ CMs in the treated samples). The higher mononuclear diploid (2n) CMs implies true proliferation rather than mere DNA synthesis without cytokinesis. This was confirmed by a 3-day live cell imaging of PSAM4 CMs under treated and control conditions with tubulin staining that confirmed formation of two new daughter cells in treated samples.

While these findings provided a promising initial validation of the hypothesis that transient contractile arrest facilitated proliferation, several limitations must be acknowledged. IPSC-CMs cultured in 2D are well known to exhibit an immature phenotype, lacking the structural, metabolic and electrophysiological characteristics of adult human CMs, even after maturation for 2 weeks in fatty acid-rich medium. Moreover, unlike adult CMs, these CMs retain a relatively higher cell cycle activity, regardless of the maturation method or period (Yang et al., 2014).

7.2 PSAM EHTs

The transition to EHTs was a logical next step, as they provide a 3D environment that supports further maturation of iPSC-CMs, thereby more closely recapitulating the structural and functional properties of adult CMs. Within this system, we investigated both early- and late-onset treatment regimen, as well as varying durations of contractile arrest (Hirt, Boeddinghaus, et al., 2014).

In this system, inhibition of contraction in PSAM-EHTs induced several structural changes. Nuclei shape analysis revealed an increase in CMs rounding of the treated PSAM EHTs, and α-actinin staining showed pronounced sarcomere disassembly, with sarcomeric structures redistributed towards the cell periphery. These findings align with the findings from several studies on different species. In a recent YAP-induced proliferation study in which proliferation was induced by the expression of a constitutive active YAP (YAP5SA) in mice, proliferating CMs exhibited significant mitotic rounding and sarcomere disassembly (Morikawa et al., 2025). Moreover, in mice, ERBB2 activation with a doxycycline-inducible system led to CMs dedifferentiation, disassembled sarcomeres and proliferation accompanied with dilated cardiomyopathy (D’Uva et al., 2015). Another study using live cell imaging on zebrafish showed that adult proliferating CMs exhibited round shaped morphology and disassembled sarcomeres, and the detected α-actinin signal was at the cell periphery (Uribe et al., 2018). Additionally a study analysing embryonic rat cardiomyocytes proliferation, found that there was a sarcomere disassembly during CMs cell division and reassembly after cytokinesis (Ahuja et al., 2004). Furthermore, during expanding iPSC-CMs, disassembled sarcomeres and clear rounding were observed in CMs cultures (Yuan et al., 2022). Altogether, the data indicate a link between sarcomere structure/integrity and cell cycle.

The robust sarcomere disassembly observed was not linked to cell death. PSAM EHTs were assessed using TUNEL staining. The percentage of TUNEL$^+$ CMs was not elevated in treated EHTs compared to control, indicating the absence of increased apoptosis. These findings were confirmed by LDH cytotoxicity assay, and they aligned with the results from the flow cytometry experiments.

Having established that contraction inhibition in PSAM EHTs led to structural changes, I next examined the force and cell cycle activity in these EHTs. Starting with early onset treatment EHTs. These EHTs never initiated spontaneous contractions and were maintained under contractile arrest for either 14, 21, or 42 days. Only a slight macroscopic remodelling (thinning of the EHTs) was observed compared to the untreated controls. Next, the cell cycle analysis using Ki67 revealed a significant increase in Ki67$^+$ CMs in the 21- and 42-day treatment groups relative to their time-matched controls. In the 14-day treatment group, Ki67 levels showed a clear trend of increase, however the difference did not reach statistical significance. This is likely due to a high Ki67 expression in the 14-day controls, which still exhibit relatively immature phenotype. Higher EdU and Ki67 levels in EHTs on day 8 compared to day 20 have been indicated earlier (Ciucci et al., 2023). It also fits my own analysis demonstrating the decline in Ki67$^+$ nuclei in EHTs over time. Importantly, upon drug washout, they resumed spontaneous beating within hours and rapidly - within seven days - generated contractile force comparable to that of untreated beating EHTs. Interestingly, this regain of normal force development was much faster than the developmental trajectory of control EHTs. The observation was surprising, because previous studies demonstrated that contraction drives iPSC-CM maturation (Leonard et al., 2018; Ulmer et al., 2018). In contrast, our data indicate that sustained contraction inhibition does not compromise the tissue's intrinsic capacity to develop force-generating capabilities. Washout EHTs had markedly lower Ki67 positivity, showed well-arranged sarcomeres and elongated nuclei when compared to stopped EHTs, comparable to the beating control.

In contrast to the early-onset approach, we next examined whether contraction inhibition could induce cell cycle re-entry once CMs had already matured and progressed towards cell cycle exit. To this end, cells were allowed to undergo a 21-day maturation period prior to initiation of treatment, aiming to establish a phenotype more comparable to adult CMs. Following contractile maturation, contractile arrest was applied for 1, 7 and 21 days. Remarkably, even a single day of force inhibition was sufficient to induce an increase in Ki67 expression, a marker of cell cycle activity. Similar elevations were observed following 7 and 21 days of treatment. However, it is important to note that the basal Ki67 levels in untreated beating controls remained relatively high, reflecting the immature phenotype typically observed in standard iPSC-derived-CM EHTs at this stage of culture. To address this, we pursued a more stringent maturation protocol, extending the pre-treatment culture period to approximately two months (63 days). Under these conditions, basal Ki67 expression declined markedly, indicating a more quiescent and mature CM state. After 7 days of contractile arrest, these mature EHTs demonstrated a significant increase in Ki67$^+$ nuclei compared to controls. Upon washout and re-initiation of contractile activity, Ki67 levels returned to baseline within 7 days, highlighting the reversible nature of this model.

These findings were consistent with those observed in the 2D culture system, reinforcing the notion that inhibition of contraction facilitated cell cycle activity. However, Ki67 does not differentiate between DNA synthesis and true proliferative events. Therefore, we also assessed PH3, a mitosis marker, in EHTs treated for 7 days in both 21-day and 63-day maturation conditions. PH3 analysis mirrored the results obtained with EdU and Ki67, although the magnitude was approximately one-tenth of that seen with Ki67, consistent with the brief expression window of PH3 during cell division (J.-Y. Kim et al., 2017).

7.3 Ex-vivo heart slices

While the findings in 2D and 3D hiPSC-CM models were highly encouraging, it was important to recognize that hiPSC-CM do not fully recapitulate the structural and metabolic properties of the adult human myocardium, even under optimized maturation protocols (P. Wu et al., 2021). To address this limitation, we collaborated with Dr. Poch, who established an ex-vivo culture system for human adult heart tissue slices. We used AAV6 with a cTnT promoter to express PSAM4 and modulate contraction in the adult heart slices. In order to minimize secondary effects of completely stopped slice contractions, we chose a relatively low multiplicity of infection that achieved transduction of only ~8% of the CM. Under this condition, treatment with varenicline was expected to affect only the few transduced cells and not the entire slice. In accordance with this reasoning, varenicline resulted in a small, but significant reduction of the force. Such sensitivity is consistent with other studies that used myocardial slices with different pharmacological and electrophysiological interventions (Miller et al., 2020; Watson et al., 2019).

Subsequent analysis revealed a significant increase in PH3$^+$ nuclei in varenicline-treated and transduced slices, indicative of enhanced mitotic activity. Notably the relative elevation in PH3$^+$ nuclei was much higher than that observed in EHTs but was consistent with previous reports of ex-vivo heart slices models, indicating that this model is sensitive for pro-proliferative interventions (Ou et al., 2019). Interestingly, non-transduced CMs also showed an elevation in PH3$^+$ nuclei in response to varenicline. This has not been investigated in ex-vivo heart slices studies before. Two factors might explain this finding: 1) the overall decrease in contraction might have triggered an increase in cell cycle activity even in the non-transduced CM and 2) paracrine factors secreted from the transduced, varenicline-silenced and cell cycling CM might have induced CM proliferation in the non-transduced CM. The latter has been suggested in a study in pigs with an ischemia/reperfusion injury. The hearts were injected with iPSC-CMs spheroids that had overexpressed cyclin D2 and knocked out leukocyte antigen class I and II. There was significant improvement in cardiac function and reduced infarct size in the pigs hearts. The author suggested it was due to follistatin (protein that interacts with Hippo-YAP pathway), since the author treated wildtype iPSC-CMs spheroids with follistatin and detected higher proliferation. Accordingly, a hypothesis was made that the secreted follistatin induced proliferation in the endogenous pig CMs (Wei et al., 2025).

7.4 Inhibition of contraction via mavacamten

Although the three previous results provided strong evidence for the association between transient contractile arrest and cell cycle re-entry, they were derived exclusively from PSAM-based chemogenetic tools. To further validate these results using an independent approach, we employed pharmacological contraction inhibition in wild-type EHTs with mavacamten. One week of treatment with a high concentration resulted in complete suppression of contractile activity, and subsequent washout over seven days allowed recovery of force, albeit with a slower kinetic than the PSAM4 system. Analysis of these EHTs revealed a consistent phenotype: increased Ki67 and PH3 expression and pronounced sarcomere disassembly, as visualized by α-actinin. It is important to note that the initial concentration of mavacamten used (10 µM) was substantially higher than clinically relevant therapeutic concentrations. Therefore, we next investigated concentrations corresponding to those used in clinical practice (0.3 and 0.7 µM; Bello & Pellegrini, 2025). Interestingly, a concentration-dependent effect on contractile inhibition and subsequent cell cycle activation was observed, indicating that the higher the concentration, the lower the force, the higher proliferation. Former concentration-response analyses of mavacamten have primarily focused on sarcomeric organisation. For instance, Hayes and Burnette examined relative MYH6 and MYH7 (MYH6/MYH7) expression in hiPSC-CM at mavacamten concentrations of 0.1 and 0.5 µM in relation to sarcomere assembly (Hayes & Burnette, 2025). However, to date, no studies established a concentration-response curve assessing the effect of mavacamten on CM proliferation. Our work represents the first attempt to establish the effect of mavacamten on the cell cycle activity in relation to different concentrations of mavacamten.

7.5 Mechanistic insights

Having established robust evidence that inhibition of contraction promotes cell cycle activity across multiple platforms, we next sought to investigate the underlying mechanism. Specifically, we aimed to elucidate the link between reduced contractile workload and the observed re-entry into the cell cycle.

We first performed proteomics analyses to obtain a global overview of the affected pathways. These data provided confirmatory evidence of less expressed sarcomeric proteins, alongside modest upregulation of cell cycle-related pathways and a reduction in oxidative phosphorylation and glycolytic activity. However, no single pathway emerged as a dominant candidate to explain the observed phenotype.

To gain deeper insight, we proceeded with bulk RNA sequencing. Consistent with the proteomics findings, transcriptomic analysis revealed downregulation of sarcomere-associated genes and upregulation of cell cycle and cell division pathway, accompanied by a downshift of all metabolic pathways. The latter is rather unexpected, since the change from mature to immature CM is often accompanied by a metabolic shift from oxidative phosphorylation to glycolysis, and not downregulation of both. Another noteworthy primary finding was the ratios of specific isoforms (MYH7/MYH6, TNNI3/TNNI1, MYL2/MYL7, and MYL3/MYL4) that are well established markers for CMs maturity (Aballo et al., 2025). This analysis revealed an immature cardiac phenotype in treated stopped CMs, which aligns with literature (Meng et al., 2025). Together, the data indicate that the prolonged stop of contraction induces an immature CM phenotype with low global metabolic activity.

RNA sequencing data yielded a richer set of potential leads for further mechanistic exploration, highlighting several pathways potentially involved in the coupling between contractile inhibition and proliferative reactivation. An early lead from WikiPathway analysis implicated involvement of the Hippo signaling pathway, which has been widely associated with cardiac proliferation (Heallen et al., 2013; Moya & Halder, 2018;

Rausch & Hansen, 2020; von Gise et al., 2012; Xin et al., 2013). We, therefore, attempted to inhibit YAP activity with silencing siRNA. Additionally, we examined YAP localization by immunostaining. The preliminary results exhibited large variability and did not substantiate a clear role of YAP and CM proliferation under our conditions, indicating the need for better tools to investigate pathways in the future.

Another intriguing parameter examined in our model was the ratio of G-/F-actin. This was motivated by the work by Dr. Giacca and colleagues (Torrini et al., 2019) who reported that some pro-proliferative miRNAs inhibited filamentous actin depolymerization by targeting cofilin2, resulting in a decreased G-/F-actin ratio (more F-actin). However, in our system we observed the opposite trend. Contractile arrest that promoted CM proliferation was associated with an increase in G-/F-actin ratio (more G-actin). While this result does not align with the findings from Torrini et al., it is not wholly unprecedented. Other demonstrated that transient cytoskeletal remodeling in postnatal mice CMs that was observed when inducing CM proliferation with various factors resulted in an early rise in G-actin prior to cell cycle activation (Fu et al., 2024). Although Fu et al. used a different experimental setup, their findings are in line with our results and argue that high or low G-actin/F-actin ratio is not the sole determinant of cell cycle activation in CMs.

7.6 Physiological pathway

Although a definitive molecular pathway linking contraction inhibition to cell cycle activation has not yet been established, we pursued parallel investigations into the temporal relationship between sarcomere disassembly and cell cycle re-entry. To this end, a kinetic study was conducted, aimed at determining which event occurs first: does cell-cycle trigger sarcomere disassembly or does sarcomere disassembly precede/permit cell cycle activation? The results provided a clear answer - sarcomere disassembly occurred hours before the activation of cell cycle - indicating that structural remodeling of the contractile apparatus is an early and potentially permissive event rather than a downstream consequence of proliferation.

There are multiple ways in which sarcomere disassembly could permit or trigger cell cycle re-entry. First, sarcomeres are not inert machines but host signaling scaffolds. The titin kinase (TK) region forms a mechano-sensitive complex for autophagy adaptor proteins (such as Nbr1 and p62) and muscle RING-finger (MURF) E3 ubiquitin ligases. This complex could couple the sarcomeric state to nuclear transcriptional regulators such as SRF. Disruption of this complex or release of MURF family members has been shown to alter gene regulatory programs and facilitate nucleo-cytoplasmic signaling (Lange et al., 2005).

Second, loss of cytoskeletal tension was associated with sarcomere disassembly changes, nucleo-cytoskeletal force transmission, and nuclear mechanics. These forces are transmitted primarily through the LINC (linker of nucleo-skeleton and cytoskeleton) complex which spans the nuclear envelope via SUN- and Nesprin-family proteins. Reduced mechanical load on the LINC complex alters nuclear shape and stiffness, and modulates the permeability of the nuclear pores, in turn regulating mechanosensitive transcriptional cofactor such as YAP/TAZ (Lityagina & Dobreva, 2021; Versaevel et al., 2014). Disruption of the LINC-complex has been shown to directly impact nuclear mechanotransduction and downstream transcriptional programs including proliferation (S. Wang et al., 2018).

Third, sarcomere disassembly reshapes actin dynamics. Shifts in the G-actin/F-actin balance control MRTF localization and SRF activity as described earlier (Gualdrini et al., 2016; Vartiainen et al., 2007).

Fourth, sarcomere disassembly is typically accompanied by remodeling of cell-cell junctions, that mechanically link neighboring CMs such as N-cadherin. These junctions are not only structural but also signaling hubs. When junctional architecture is altered, β-catenin can be released from the membrane and translocate into the nucleus, where it functions as a transcriptional co-activator in the canonical Wnt/β-catenin pathway (Nelson & Nusse, 2004). Nuclear β-catenin accumulation is strongly associated with activation of pro-mitotic gene programs (Tsai et al., 2025).

Importantly, these mechanisms are not mutually exclusive and could act in parallel or in series. They also help explain why sarcomere disassembly maybe be necessary but not alone sufficient for proliferation. A recent study discussing titin cleavage showed that mechanically induced sarcomere disassembly by cleaving titin, though it did not inhibit CM contraction, does not automatically produce an increase in CM proliferation (Pricolo et al., 2025).

On the other hand, there is a clear down regulation in metabolic pathways in treated CMs compared to the beating ones. This could be a plausible cause for increased proliferation, as the less ATP production leads to less ROS production. ROS production is a leading cause for cell cycle arrest in postnatal CMs (Puente et al., 2014). Thus, the absence of ROS may lead to cell cycle re-entry.

7.7 Conclusion

The hypothesis underlying this project - that CM contractile activity and workload restrict its proliferative potential (All work, no repair) - was well recognized in the literature but has never been directly addressed. A major challenge has been the lack of tools to transiently suppress CM contraction without inducing irreversible damage. In this work, the PSAM models provided such a tool, enabling reversible inhibition of contraction and thereby allowing a direct assessment of workload on cell cycle activity.

Using this system, I demonstrated that transient inhibition of contraction reproducibly promoted cell cycle re-entry in CMs across multiple experimental settings; 2D CM, 3D EHTs, and heart slices. The recovery of contractile function confirmed that the intervention did not compromise cell viability. Although the extent of proliferation was insufficient to enhance contractile force of EHTs or CM cultured in 2D format, it was clearly detectable and consistent. The effect was linked specifically to inhibition of contraction rather than loss of excitability as indicated by the mavacamten experiments.

To explore the underlying mechanisms, I employed proteomic and transcriptomic analyses. These approaches confirmed increased expression of cell cycle-related proteins and genes, and reduced expression of sarcomere-related proteins and genes. They also identified several candidate transcription factors and regulators that may potentially mediate this response. The mechanistic exploration remains at an early stage, with preliminary results. Finally, temporal analysis revealed that sarcomere disassembly preceded induction of cell cycle marker Ki67, establishing a physiological sequence of events and the need for sarcomere disassembly for CM to proliferate.

7.8 Future perspective

While this work establishes a solid link between CM contraction and proliferative capacity, several important questions remain open for future exploration.
First, a deeper dissection of the underlying mechanism(s) will require more comprehensive approaches. Transcriptomic profiling at single-nucleus level could uncover cell-to-cell heterogeneity in the proliferative response, while bulk RNA sequencing across early time points (1 - 24 hours after contraction inhibition) would provide temporal resolution of gene expression changes. Complementing these, phospho-proteomic analysis of these early time point samples could capture upstream signalling events and dynamic kinase activity that precede transcriptional remodelling. Together, these approaches would help to reconstruct the regulatory cascade linking sarcomere disassembly to cell cycle re-entry.

Second, the preliminary leads identified from transcriptomic and proteomic screens need to be functionally validated. Since siRNA approaches are often unreliable in CMs, progress will require either collaboration with groups that already maintain relevant knockdown or over-expression models, or the establishment of precise gene editing strategies in-house. Such targeted approaches will be essential to confirm casual roles for specific transcription factors or signalling pathways.

Third, the dynamics of repeated cycles of contraction inhibition remain unexplored. Iterative treatment-washout experiments, coupled with analysis of different cell cycle markers at each cycle, e.g. EdU, Ki67 and 5-Bromdesoxyuridin (BrdU), could reveal whether CMs accumulate proliferative capacity or follow divergent fates with repeated unloading. This may also shed light on why only a fraction of cells respond despite global inhibition of contraction.

Another question is to which extent the observed increase in CM proliferation led to an increase in total CM numbers. Current assays in our project such as FACS proved technically challenging, with significant cell loss during staining and washing steps, and the magnitude of observed proliferation was not large, thus difficult to quantify reliably. Developing other methods of quantification will therefore be critical.

Finally, the translation of these findings into therapeutically relevant applications deserves attention. Human heart slices experiments demonstrated a generalized increase in CM proliferation despite partial transduction. This observation is of particular translational relevance, because gene delivery to the heart in clinical setups is inherently inefficient and heterogenous, with only a fraction of the myocardium effectively modified (Cannatà et al., 2020; Lyon et al., 2008). This suggests generating mixed EHTs with WT and PSAM4 CMs to mimic the therapeutic scenarios. Such models would allow further investigation into how partial inhibition of contraction influences proliferation, cell-cell contact, electrophysiological properties, and the underlying mechanism. Moreover, it would be valuable to assess this effect through targeted PSAM4 channel transduction in animal models and transplantation/cells injection approaches, ultimately advancing the concept of a biological LVAD-like strategy. Overall, this chemogenetic tool provides a versatile experimental platform to dissect the relationship between contraction, sarcomere organization and workload, while also serving as a translationally relevant model to explore novel biological strategies for cardiac regeneration.

8. References

Aballo, T. J., Bae, J., Paltzer, W. G., Chapman, E. A., Perciaccante, A. J., Pergande, M. R., Salamon, R. J., Nuttall, D. J., Mann, M. W., Ge, Y., & Mahmoud, A. I. (2025). Integrated proteomics identifies troponin I isoform switch as a regulator of a sarcomere-metabolism axis during cardiac regeneration. *Cardiovascular Research*, *121*(8), 1240–1253. https://doi.org/10.1093/cvr/cvaf069

Ahuja, P., Perriard, E., Perriard, J. C., & Ehler, E. (2004). Sequential myofibrillar breakdown accompanies mitotic division of mammalian cardiomyocytes. *Journal of Cell Science*, *117*(15), 3295–3306. https://doi.org/10.1242/JCS.01159,

Ahuja, P., Sdek, P., & MacLellan, W. R. (2007). Cardiac Myocyte Cell Cycle Control in Development, Disease, and Regeneration. *Physiological Reviews*, *87*(2), 521–544. https://doi.org/10.1152/physrev.00032.2006

Ali, H., Braga, L., & Giacca, M. (2020). Cardiac regeneration and remodelling of the cardiomyocyte cytoarchitecture. *The FEBS Journal*, *287*(3), 417–438. https://doi.org/10.1111/febs.15146

Ashburner, M., Ball, C. A., Blake, J. A., Botstein, D., Butler, H., Cherry, J. M., Davis, A. P., Dolinski, K., Dwight, S. S., Eppig, J. T., Harris, M. A., Hill, D. P., Issel-Tarver, L., Kasarskis, A., Lewis, S., Matese, J. C., Richardson, J. E., Ringwald, M., Rubin, G. M., & Sherlock, G. (2000). Gene ontology: Tool for the unification of biology. The Gene Ontology Consortium. *Nature Genetics*, *25*(1), 25–29. https://doi.org/10.1038/75556

Balza, R. O., & Misra, R. P. (2006). Role of the Serum Response Factor in Regulating Contractile Apparatus Gene Expression and Sarcomeric Integrity in Cardiomyocytes*. *Journal of Biological Chemistry*, *281*(10), 6498–6510. https://doi.org/10.1074/jbc.M509487200

Bárány, M. (1967). ATPase Activity of Myosin Correlated with Speed of Muscle Shortening. *Journal of General Physiology*, *50*(6), 197–218. https://doi.org/10.1085/jgp.50.6.197

Bassat, E., Mutlak, Y. E., Genzelinakh, A., Shadrin, I. Y., Baruch Umansky, K., Yifa, O., Kain, D., Rajchman, D., Leach, J., Riabov Bassat, D., Udi, Y., Sarig, R., Sagi, I., Martin, J. F., Bursac, N., Cohen, S., & Tzahor, E. (2017). The extracellular matrix protein agrin promotes heart regeneration in mice. *Nature*, *547*(7662), 179–184. https://doi.org/10.1038/nature22978

Bello, J., & Pellegrini, M. V. (2025). Mavacamten. In *StatPearls*. StatPearls Publishing. http://www.ncbi.nlm.nih.gov/books/NBK582152/

Bergmann, O., Bhardwaj, R. D., Bernard, S., Zdunek, S., Barnabé-Heide, F., Walsh, S., Zupicich, J., Alkass, K., Buchholz, B. A., Druid, H., Jovinge, S., & Frisén, J. (2009). Evidence for cardiomyocyte renewal in humans. *Science (New York, N.Y.)*, *324*(5923), 98–102. https://doi.org/10.1126/SCIENCE.1164680

Bers, D. M. (2002). Cardiac excitation–contraction coupling. *Nature*, *415*(6868), 198–205. https://doi.org/10.1038/415198a

Black, B. L., & Olson, E. N. (1998). TRANSCRIPTIONAL CONTROL OF MUSCLE DEVELOPMENT BY MYOCYTE ENHANCER FACTOR-2 (MEF2) PROTEINS. *Annual Review of Cell and Developmental Biology*, *14*(Volume 14, 1998), 167–196. https://doi.org/10.1146/annurev.cellbio.14.1.167

Blomen, V. A., & Boonstra, J. (2007). Cell fate determination during G1 phase progression. *Cellular and Molecular Life Sciences*, *64*(23), 3084–3104. https://doi.org/10.1007/s00018-007-7271-z

Borg, T. K., Rubin, K., Lundgren, E., Borg, K., & Öbrink, B. (1984). Recognition of extracellular matrix components by neonatal and adult cardiac myocytes. *Developmental Biology*, *104*(1), 86–96. https://doi.org/10.1016/0012-1606(84)90038-1

Boron, W. F., & Boulpaep, E. L. (2020). *Boron & Boulpaep Concise Medical Physiology E-Book: Boron & Boulpaep Concise Medical Physiology E-Book*. Elsevier Health Sciences.

Busk, P. K., Hinrichsen, R., Bartkova, J., Hansen, A. H., Christoffersen, T. E. H., Bartek, J., & Haunsø, S. (2005). Cyclin D2 induces proliferation of cardiac myocytes and represses hypertrophy. *Experimental Cell Research*, *304*(1), 149–161. https://doi.org/10.1016/j.yexcr.2004.10.022

Cannatà, A., Ali, H., Sinagra, G., & Giacca, M. (2020). Gene Therapy for the Heart Lessons Learned and Future Perspectives. *Circulation Research*. https://doi.org/10.1161/CIRCRESAHA.120.315855

Canseco, D. C., Kimura, W., Garg, S., Mukherjee, S., Bhattacharya, S., Abdisalaam, S., Das, S., Asaithamby, A., Mammen, P. P. A., & Sadek, H. A. (2015). Human

Ventricular Unloading Induces Cardiomyocyte Proliferation. *JACC*, *65*(9), 892–900. https://doi.org/10.1016/j.jacc.2014.12.027

Chaudhry, H. W., Dashoush, N. H., Tang, H., Zhang, L., Wang, X., Wu, E. X., & Wolgemuth, D. J. (2004). Cyclin A2 mediates cardiomyocyte mitosis in the postmitotic myocardium. *The Journal of Biological Chemistry*, *279*(34), 35858–35866. https://doi.org/10.1074/jbc.M404975200

Chen, S., Zhou, Y., Chen, Y., & Gu, J. (2018). fastp: An ultra-fast all-in-one FASTQ preprocessor. *Bioinformatics (Oxford, England)*, *34*(17), i884–i890. https://doi.org/10.1093/bioinformatics/bty560

Citri, A., & Yarden, Y. (2006). EGF–ERBB signalling: Towards the systems level. *Nature Reviews Molecular Cell Biology*, *7*(7), 505–516. https://doi.org/10.1038/nrm1962

Ciucci, G., Rahhali, K., Cimmino, G., Natale, F., Golino, P., Sinagra, G., Collesi, C., & Loffredo, F. S. (2023). Engineered heart tissue maturation inhibits cardiomyocyte proliferative response to cryoinjury. *Journal of Tissue Engineering*, *14*, 20417314231190147. https://doi.org/10.1177/20417314231190147

Cluzeaut, F., & Maurer-Schultze, B. (1986). Proliferation of Cardiomyocytes and Interstitial Cells In the Cardiac Muscle of the Mouse During Pre- and Postnatal Development. *Cell Proliferation*, *19*(3), 267–274. https://doi.org/10.1111/j.1365-2184.1986.tb00679.x

Cooper, G. M. (2000). The Eukaryotic Cell Cycle. In *The Cell: A Molecular Approach. 2nd edition*. Sinauer Associates. https://www.ncbi.nlm.nih.gov/books/NBK9876/

Crescenzi, M. (2002). *Reactivation of the Cell Cycle in Terminally Differentiated Cells*. Springer Science & Business Media.

Cui, M., Wang, Z., Bassel-Duby, R., & Olson, E. N. (2018). Genetic and epigenetic regulation of cardiomyocytes in development, regeneration and disease. *Development*, *145*(24), dev171983. https://doi.org/10.1242/dev.171983

de Haan, J., van Bemmel, J. H., Stolte, L. A. M., Janssens, J., Eskes, T. K. A. B., Versteeg, B., Veth, A. F. L., & Braaksma, J. T. (1971). Quantitative evaluation of fetal heart rate patterns: II. The significance of the fixed heart rate during pregnancy and labor. *European Journal of Obstetrics & Gynecology*, *1*(3), 103–110. https://doi.org/10.1016/0028-2243(71)90057-8

Denning, C., Borgdorff, V., Crutchley, J., Firth, K. S. A., George, V., Kalra, S., Kondrashov, A., Hoang, M. D., Mosqueira, D., Patel, A., Prodanov, L., Rajamohan, D., Skarnes, W. C., Smith, J. G. W., & Young, L. E. (2015). Cardiomyocytes from human pluripotent stem cells: From laboratory curiosity to industrial biomedical platform. *BBA - Biochimica et Biophysica Acta*, *1863*(7). https://doi.org/10.1016/j.bbamcr.2015.10.014

Derks, W., & Bergmann, O. (2020). Polyploidy in Cardiomyocytes. *Circulation Research*, *126*(4), 552–565. https://doi.org/10.1161/CIRCRESAHA.119.315408

Derks, W., Rode, J., Collin, S., Rost, F., Heinke, P., Hariharan, A., Pickel, L., Simonova, I., Lázár, E., Graham, E., Jashari, R., Andrä, M., Jeppsson, A., Salehpour, M., Alkass, K., Druid, H., Kyriakopoulos, C. P., Taleb, I., Shankar, T. S., … Bergmann, O. (2025). A Latent Cardiomyocyte Regeneration Potential in Human Heart Disease. *Circulation*, *151*(3), 245–256. https://doi.org/10.1161/CIRCULATIONAHA.123.067156

Dhahri, W., Sadikov Valdman, T., Wilkinson, D., Pereira, E., Ceylan, E., Andharia, N., Qiang, B., Masoudpour, H., Wulkan, F., Quesnel, E., Jiang, W., Funakoshi, S., Mazine, A., Gomez-Garcia, M. J., Latifi, N., Jiang, Y., Huszti, E., Simmons, C. A., Keller, G., & Laflamme, M. A. (2022). In Vitro Matured Human Pluripotent Stem Cell–Derived Cardiomyocytes Form Grafts With Enhanced Structure and Function in Injured Hearts. *Circulation*, *145*(18), 1412–1426. https://doi.org/10.1161/CIRCULATIONAHA.121.053563

Ding, D., & Braun, T. (2023). A Tedious Journey: Cardiomyocyte Proliferation Requires More Than S-Phase Entry and Loss of Polyploidization. *Circulation*, *147*(2), 154–157. https://doi.org/10.1161/CIRCULATIONAHA.122.062784

Dobin, A., Davis, C. A., Schlesinger, F., Drenkow, J., Zaleski, C., Jha, S., Batut, P., Chaisson, M., & Gingeras, T. R. (2013). STAR: Ultrafast universal RNA-seq aligner. *Bioinformatics (Oxford, England)*, *29*(1), 15–21. https://doi.org/10.1093/bioinformatics/bts635

Doudna, J. A., & Charpentier, E. (2014). The new frontier of genome engineering with CRISPR-Cas9. *Science*, *346*(6213), 1258096. https://doi.org/10.1126/science.1258096

Dunbar, C. E., High, K. A., Joung, J. K., Kohn, D. B., Ozawa, K., & Sadelain, M. (2018). Gene therapy comes of age. *Science*, *359*(6372), eaan4672. https://doi.org/10.1126/science.aan4672

D'Uva, G., Aharonov, A., Lauriola, M., Kain, D., Yahalom-Ronen, Y., Carvalho, S., Weisinger, K., Bassat, E., Rajchman, D., Yifa, O., Lysenko, M., Konfino, T., Hegesh, J., Brenner, O., Neeman, M., Yarden, Y., Leor, J., Sarig, R., Harvey, R. P., & Tzahor, E. (2015). ERBB2 triggers mammalian heart regeneration by promoting cardiomyocyte dedifferentiation and proliferation. *Nature Cell Biology*, *17*(5), 627–638. https://doi.org/10.1038/ncb3149

DZHK study: BioVAT-HF-DZHK20: DZHK study. (n.d.). Retrieved July 4, 2025, from https://biovat.dzhk.de/

Ebelt, H., Zhang, Y., Kampke, A., Xu, J., Schlitt, A., Buerke, M., Müller-Werdan, U., Werdan, K., & Braun, T. (2008). E2F2 expression induces proliferation of terminally differentiated cardiomyocytes in vivo. *Cardiovascular Research*, *80*(2), 219–226. https://doi.org/10.1093/cvr/cvn194

Eschenhagen, T., Fink, C., Remmers, U., Scholz, H., Wattchow, J., Weil, J., Zimmermann, W., Dohmen, H. H., Schäfer, H., Bishopric, N., Wakatsuki, T., & Elson, E. L. (1997). Three-dimensional reconstitution of embryonic cardiomyocytes in a collagen matrix: A new heart muscle model system. *FASEB Journal: Official Publication of the Federation of American Societies for Experimental Biology*, *11*(8), 683–694. https://doi.org/10.1096/fasebj.11.8.9240969

Fan, X., Hughes, B. G., Ali, M. A. M., Cho, W. J., Lopez, W., & Schulz, R. (2015). Dynamic Alterations to α-Actinin Accompanying Sarcomere Disassembly and Reassembly during Cardiomyocyte Mitosis. *PloS One*, *10*(6), e0129176. https://doi.org/10.1371/journal.pone.0129176

Feyen, D. A. M., McKeithan, W. L., Bruyneel, A. A. N., Spiering, S., Hörmann, L., Ulmer, B., Zhang, H., Briganti, F., Schweizer, M., Hegyi, B., Liao, Z., Pölönen, R. P., Ginsburg, K. S., Lam, C. K., Serrano, R., Wahlquist, C., Kreymerman, A., Vu, M., Amatya, P. L., … Mercola, M. (2020). Metabolic Maturation Media Improve Physiological Function of Human iPSC-Derived Cardiomyocytes. *Cell Reports*, *32*(3). https://doi.org/10.1016/j.celrep.2020.107925

Fischer, C., Milting, H., Fein, E., Reiser, E., Lu, K., Seidel, T., Schinner, C., Schwarzmayr, T., Schramm, R., Tomasi, R., Husse, B., Cao-Ehlker, X., Pohl, U., & Dendorfer, A. (2019). Publisher Correction: Long-term functional and structural preservation of precision-cut human myocardium under continuous electromechanical stimulation in vitro. *Nature Communications*, *10*(1), 532. https://doi.org/10.1038/s41467-019-08510-9

Fisher, D. J., Heymann, M. A., & Rudolph, A. M. (1980). Myocardial oxygen and carbohydrate consumption in fetal lambs in utero and in adult sheep. *American Journal of Physiology-Heart and Circulatory Physiology*, *238*(3), H399–H405. https://doi.org/10.1152/ajpheart.1980.238.3.H399

Fu, W., Liao, Q., Shi, Y., Liu, W., Ren, H., Xu, C., & Zeng, C. (2024). Transient induction of actin cytoskeletal remodeling associated with dedifferentiation, proliferation, and redifferentiation stimulates cardiac regeneration. *Acta Pharmaceutica Sinica. B*, *14*(6), 2537–2553. https://doi.org/10.1016/j.apsb.2024.01.021

Garcia-Alonso, L., Holland, C. H., Ibrahim, M. M., Turei, D., & Saez-Rodriguez, J. (2019). Benchmark and integration of resources for the estimation of human transcription factor activities. *Genome Research*, *29*(8), 1363–1375. https://doi.org/10.1101/gr.240663.118

Gérard, C., & Goldbeter, A. (2012). From quiescence to proliferation: Cdk oscillations drive the mammalian cell cycle. *Frontiers in Physiology*, *3*. https://doi.org/10.3389/fphys.2012.00413

González-Rosa, J. M., Sharpe, M., Field, D., Soonpaa, M. H., Field, L. J., Burns, C. E., & Burns, C. G. (2018). Myocardial Polyploidization Creates a Barrier to Heart Regeneration in Zebrafish. *Developmental Cell*, *44*(4), 433-446.e7. https://doi.org/10.1016/j.devcel.2018.01.021

Gordon, A. M., Homsher, E., & Regnier, M. (2000). Regulation of contraction in striated muscle. *Physiological Reviews*, *80*(2), 853–924. https://doi.org/10.1152/physrev.2000.80.2.853

Gualdrini, F., Esnault, C., Horswell, S., Stewart, A., Matthews, N., & Treisman, R. (2016). SRF Co-factors Control the Balance between Cell Proliferation and Contractility. *Molecular Cell*, *64*(6), 1048–1061. https://doi.org/10.1016/j.molcel.2016.10.016

Guo, Y., Cao, Y., Jardin, B. D., Sethi, I., Ma, Q., Moghadaszadeh, B., Troiano, E. C., Mazumdar, N., Trembley, M. A., Small, E. M., Yuan, G.-C., Beggs, A. H., & Pu, W. T. (2021). Sarcomeres regulate murine cardiomyocyte maturation through

MRTF-SRF signaling. *Proceedings of the National Academy of Sciences of the United States of America*, *118*(2), e2008861118. https://doi.org/10.1073/pnas.2008861118

Guo, Y., & Pu, W. T. (2020). Cardiomyocyte Maturation. *Circulation Research*, *126*(8), 1086–1106. https://doi.org/10.1161/CIRCRESAHA.119.315862

Gur, J., Devanagondi, R., Pratt, R., Smith, F., Mandell, J., Martin, S., & Porter, G. A. (2025). A Case of Complete Functional Myocardial Regeneration in a Human Neonate. *JACC: Case Reports*, *30*(14), 103622. https://doi.org/10.1016/j.jaccas.2025.103622

Hansen, A., Eder, A., Bönstrup, M., Flato, M., Mewe, M., Schaaf, S., Aksehirlioglu, B., Schwörer, A., Uebeler, J., & Eschenhagen, T. (2010). Development of a Drug Screening Platform Based on Engineered Heart Tissue. *Circulation Research*, *107*(1), 35–44. https://doi.org/10.1161/CIRCRESAHA.109.211458

Härtter, D., Hauke, L., Driehorst, T., Long, Y., Bao, G., Primeßnig, A., Berečić, B., Cyganek, L., Tiburcy, M., Schmidt, C. F., & Zimmermann, W.-H. (2025). *SarcAsM: AI-based multiscale analysis of sarcomere organization and contractility in cardiomyocytes* (p. 2025.04.29.650605). bioRxiv. https://doi.org/10.1101/2025.04.29.650605

Harvey, R. P. (2002). Patterning the vertebrate heart. *Nature Reviews Genetics*, *3*(7), 544–556. https://doi.org/10.1038/nrg843

Haubner, B. J., Schneider, J., Schweigmann, U., Schuetz, T., Dichtl, W., Velik-Salchner, C., Stein, J.-I., & Penninger, J. M. (2016). Functional Recovery of a Human Neonatal Heart After Severe Myocardial Infarction. *Circulation Research*, *118*(2), 216–221. https://doi.org/10.1161/CIRCRESAHA.115.307017

Hayes, J. B., & Burnette, D. T. (2025). Pharmacological Inhibition of β Myosin II Disrupts Sarcomere Assembly in Human iPSC-Derived Cardiac Myocytes. *Cytoskeleton*, *0*, 1–9. https://doi.org/10.1002/CM.22006;PAGEGROUP:STRING:PUBLICATION

Heallen, T., Morikawa, Y., Leach, J., Tao, G., Willerson, J. T., Johnson, R. L., & Martin, J. F. (2013). Hippo signaling impedes adult heart regeneration. *Development*, *140*(23), 4683–4690. https://doi.org/10.1242/dev.102798

Hesse, M., Welz, A., & Fleischmann, B. K. (2018). Heart regeneration and the cardiomyocyte cell cycle. *Pflügers Archiv - European Journal of Physiology*, *470*(2), 241–248. https://doi.org/10.1007/s00424-017-2061-4

Heymann, M. A., Iwamoto, H. S., & Rudolph, A. M. (1981). Factors affecting changes in the neonatal systemic circulation. *Annual Review of Physiology*, *43*, 371–383. https://doi.org/10.1146/annurev.ph.43.030181.002103

Hirose, K., Payumo, A. Y., Cutie, S., Hoang, A., Zhang, H., Guyot, R., Lunn, D., Bigley, R. B., Yu, H., Wang, J., Smith, M., Gillett, E., Muroy, S. E., Schmid, T., Wilson, E., Field, K. A., Reeder, D. M., Maden, M., Yartsev, M. M., … Huang, G. N. (2019). Evidence for hormonal control of heart regenerative capacity during endothermy acquisition. *Science*, *364*(6436), 184–188. https://doi.org/10.1126/science.aar2038

Hirt, M. N., Boeddinghaus, J., Mitchell, A., Schaaf, S., Börnchen, C., Müller, C., Schulz, H., Hubner, N., Stenzig, J., Stoehr, A., Neuber, C., Eder, A., Luther, P. K., Hansen, A., & Eschenhagen, T. (2014). Functional improvement and maturation of rat and human engineered heart tissue by chronic electrical stimulation. *Journal of Molecular and Cellular Cardiology*, *74*, 151–161. https://doi.org/10.1016/j.yjmcc.2014.05.009

Hirt, M. N., Hansen, A., & Eschenhagen, T. (2014). Cardiac Tissue Engineering: State of the Art. *Circulation Research*, *114*(2), 354–367. https://doi.org/10.1161/CIRCRESAHA.114.300522

Hockemeyer, D., & Jaenisch, R. (2016). Induced pluripotent stem cells meet genome editing. *Cell Stem Cell*, *18*(5), 573–586. https://doi.org/10.1016/j.stem.2016.04.013

Holbro, T., Beerli, R. R., Maurer, F., Koziczak, M., Barbas, C. F., & Hynes, N. E. (2003). The ErbB2/ErbB3 heterodimer functions as an oncogenic unit: ErbB2 requires ErbB3 to drive breast tumor cell proliferation. *Proceedings of the National Academy of Sciences*, *100*(15), 8933–8938. https://doi.org/10.1073/pnas.1537685100

Hom, J. R., Quintanilla, R. A., Hoffman, D. L., de Mesy Bentley, K. L., Molkentin, J. D., Sheu, S.-S., & Porter, G. A. (2011). The Permeability Transition Pore Controls Cardiac Mitochondrial Maturation and Myocyte Differentiation. *Developmental Cell*, *21*(3), 469–478. https://doi.org/10.1016/j.devcel.2011.08.008

Hughes, C. S., Moggridge, S., Müller, T., Sorensen, P. H., Morin, G. B., & Krijgsveld, J. (2019). Single-pot, solid-phase-enhanced sample preparation for proteomics experiments. *Nature Protocols*, *14*(1), 68–85. https://doi.org/10.1038/s41596-018-0082-x

Hussein, S. M., Batada, N. N., Vuoristo, S., Ching, R. W., Autio, R., Närvä, E., Ng, S., Sourour, M., Hämäläinen, R., Olsson, C., Lundin, K., Mikkola, M., Trokovic, R., Peitz, M., Brüstle, O., Bazett-Jones, D. P., Alitalo, K., Lahesmaa, R., Nagy, A., & Otonkoski, T. (2011). Copy number variation and selection during reprogramming to pluripotency. *Nature*, *471*(7336), 58–62. https://doi.org/10.1038/nature09871

Jassal, B., Matthews, L., Viteri, G., Gong, C., Lorente, P., Fabregat, A., Sidiropoulos, K., Cook, J., Gillespie, M., Haw, R., Loney, F., May, B., Milacic, M., Rothfels, K., Sevilla, C., Shamovsky, V., Shorser, S., Varusai, T., Weiser, J., … D'Eustachio, P. (2020). The reactome pathway knowledgebase. *Nucleic Acids Research*, *48*(D1), D498–D503. https://doi.org/10.1093/nar/gkz1031

Jebran, A.-F., Seidler, T., Tiburcy, M., Daskalaki, M., Kutschka, I., Fujita, B., Ensminger, S., Bremmer, F., Moussavi, A., Yang, H., Qin, X., Mißbach, S., Drummer, C., Baraki, H., Boretius, S., Hasenauer, C., Nette, T., Kowallick, J., Ritter, C. O., … Zimmermann, W.-H. (2025). Engineered heart muscle allografts for heart repair in primates and humans. *Nature*, *639*(8054), 503–511. https://doi.org/10.1038/s41586-024-08463-0

Jopling, C., Sleep, E., Raya, M., Martí, M., Raya, A., & Belmonte, J. C. I. (2010). Zebrafish heart regeneration occurs by cardiomyocyte dedifferentiation and proliferation. *Nature*, *464*(7288), 606–609. https://doi.org/10.1038/nature08899

Kanehisa, M., & Goto, S. (2000). KEGG: Kyoto encyclopedia of genes and genomes. *Nucleic Acids Research*, *28*(1), 27–30. https://doi.org/10.1093/nar/28.1.27

Karbassi, E., Fenix, A., Marchiano, S., Muraoka, N., Nakamura, K., Yang, X., & Murry, C. E. (2020). Cardiomyocyte maturation: Advances in knowledge and implications for regenerative medicine. *Nature Reviews. Cardiology*, *17*(6), 341–359. https://doi.org/10.1038/s41569-019-0331-x

Kastan, M. B., & Bartek, J. (2004). Cell-cycle checkpoints and cancer. *Nature*, *432*(7015), 316–323. https://doi.org/10.1038/nature03097

Kayali, F., Tahhan, O., Vecchio, G., Jubouri, M., Noubani, J. M., Bailey, D. M., Williams, I. M., Awad, W. I., & Bashir, M. (2024). Left ventricular unloading to facilitate ventricular remodelling in heart failure: A narrative review of mechanical circulatory support. *Experimental Physiology*, *109*(11), 1826–1836. https://doi.org/10.1113/EP091796

Kennedy-Lydon, T., & Rosenthal, N. (2017). Cardiac regeneration: All work and no repair? *Science Translational Medicine*, *9*(383), eaad9019. https://doi.org/10.1126/scitranslmed.aad9019

Kim, J.-Y., Jeong, H. S., Chung, T., Kim, M., Lee, J. H., Jung, W. H., & Koo, J. S. (2017). The value of phosphohistone H3 as a proliferation marker for evaluating invasive breast cancers: A comparative study with Ki67. *Oncotarget*, *8*(39), 65064–65076. https://doi.org/10.18632/oncotarget.17775

Kim, K., Doi, A., Wen, B., Ng, K., Zhao, R., Cahan, P., Kim, J., Aryee, M. J., Ji, H., Ehrlich, L. I. R., Yabuuchi, A., Takeuchi, A., Cunniff, K. C., Hongguang, H., McKinney-Freeman, S., Naveiras, O., Yoon, T. J., Irizarry, R. A., Jung, N., … Daley, G. Q. (2010). Epigenetic memory in induced pluripotent stem cells. *Nature*, *467*(7313), 285–290. https://doi.org/10.1038/nature09342

Kim, N.-G., & Gumbiner, B. M. (2015). Adhesion to fibronectin regulates Hippo signaling via the FAK–Src–PI3K pathway. *Journal of Cell Biology*, *210*(3), 503–515. https://doi.org/10.1083/jcb.201501025

Kirillova, A., Han, L., Liu, H., & Kühn, B. (2021). Polyploid cardiomyocytes: Implications for heart regeneration. *Development*, *148*(14), dev199401. https://doi.org/10.1242/dev.199401

Kubin, T., Pöling, J., Kostin, S., Gajawada, P., Hein, S., Rees, W., Wietelmann, A., Tanaka, M., Lörchner, H., Schimanski, S., Szibor, M., Warnecke, H., & Braun, T. (2011). Oncostatin M Is a Major Mediator of Cardiomyocyte Dedifferentiation and Remodeling. *Cell Stem Cell*, *9*(5), 420–432. https://doi.org/10.1016/j.stem.2011.08.013

Laflamme, M. A., & Murry, C. E. (2005). Regenerating the heart. *Nature Biotechnology*, *23*(7), 845–856. https://doi.org/10.1038/nbt1117

Lam, N. T., & Sadek, H. A. (2018). Neonatal Heart Regeneration. *Circulation*, *138*(4), 412–423. https://doi.org/10.1161/CIRCULATIONAHA.118.033648

Lange, S., Xiang, F., Yakovenko, A., Vihola, A., Hackman, P., Rostkova, E., Kristensen, J., Brandmeier, B., Franzen, G., Hedberg, B., Gunnarsson, L. G., Hughes, S. M., Marchand, S., Sejersen, T., Richard, I., Edström, L., Ehler, E., Udd, B., & Gautel, M. (2005). The Kinase Domain of Titin Controls Muscle Gene

Expression and Protein Turnover. *Science*, *308*(5728), 1599–1603. https://doi.org/10.1126/science.1110463

Laoukili, J., Kooistra, M. R. H., Brás, A., Kauw, J., Kerkhoven, R. M., Morrison, A., Clevers, H., & Medema, R. H. (2005). FoxM1 is required for execution of the mitotic programme and chromosome stability. *Nature Cell Biology*, *7*(2), 126–136. https://doi.org/10.1038/ncb1217

Laskey, R. A., Fairman, M. P., & Blow, J. J. (1989). S Phase of the Cell Cycle. *Science*, *246*(4930), 609–614. https://doi.org/10.1126/science.2683076

Leonard, A., Bertero, A., Powers, J. D., Beussman, K. M., Bhandari, S., Regnier, M., Murry, C. E., & Sniadecki, N. J. (2018). Afterload Promotes Maturation of Human Induced Pluripotent Stem Cell Derived Cardiomyocytes in Engineered Heart Tissues. *Journal of Molecular and Cellular Cardiology*, *118*, 147–158. https://doi.org/10.1016/j.yjmcc.2018.03.016

Li, F., Wang, X., Capasso, J. M., & Gerdes, A. M. (1996). Rapid transition of cardiac myocytes from hyperplasia to hypertrophy during postnatal development. *Journal of Molecular and Cellular Cardiology*, *28*(8), 1737–1746. https://doi.org/10.1006/jmcc.1996.0163

Li, X., McLain, C., Samuel, M. S., Olson, M. F., & Radice, G. L. (2023). Actomyosin-mediated cellular tension promotes Yap nuclear translocation and myocardial proliferation through α5 integrin signaling. *Development (Cambridge, England)*, *150*(2), dev201013. https://doi.org/10.1242/dev.201013

Lian, X., Hsiao, C., Wilson, G., Zhu, K., Hazeltine, L. B., Azarin, S. M., Raval, K. K., Zhang, J., Kamp, T. J., & Palecek, S. P. (2012). Robust cardiomyocyte differentiation from human pluripotent stem cells via temporal modulation of canonical Wnt signaling. *Proceedings of the National Academy of Sciences of the United States of America*, *109*(27), E1848-57. https://doi.org/10.1073/pnas.1200250109

Lim, S., & Kaldis, P. (2013). Cdks, cyclins and CKIs: Roles beyond cell cycle regulation. *Development*, *140*(15), 3079–3093. https://doi.org/10.1242/dev.091744

Lityagina, O., & Dobreva, G. (2021). The LINC Between Mechanical Forces and Chromatin. *Frontiers in Physiology*, *12*. https://doi.org/10.3389/fphys.2021.710809

Liu, J. J., Peng, L., Bradley, C. J., Zulli, A., Shen, J., & Buxton, B. F. (2000). Increased apoptosis in the heart of genetic hypertension, associated with increased fibroblasts. *Cardiovascular Research*, *45*(3), 729–735. https://doi.org/10.1016/s0008-6363(99)00382-x

Lopaschuk, G. D., Collins-Nakai, R. L., & Itoi, T. (1992). Developmental changes in energy substrate use by the heart. *Cardiovascular Research*, *26*(12), 1172–1180. https://doi.org/10.1093/cvr/26.12.1172

Lopaschuk, G. D., Ussher, J. R., Folmes, C. D. L., Jaswal, J. S., & Stanley, W. C. (2010). Myocardial Fatty Acid Metabolism in Health and Disease. *Physiological Reviews*, *90*(1), 207–258. https://doi.org/10.1152/physrev.00015.2009

Louch, W. E., Sejersted, O. M., & Swift, F. (2010). There Goes the Neighborhood: Pathological Alterations in T-Tubule Morphology and Consequences for Cardiomyocyte Ca2+ Handling. *BioMed Research International*, *2010*(1), 503906. https://doi.org/10.1155/2010/503906

Love, M. I., Huber, W., & Anders, S. (2014). Moderated estimation of fold change and dispersion for RNA-seq data with DESeq2. *Genome Biology*, *15*(12), 550. https://doi.org/10.1186/s13059-014-0550-8

Lundy, S. D., Zhu, W.-Z., Regnier, M., & Laflamme, M. A. (2013). Structural and Functional Maturation of Cardiomyocytes Derived from Human Pluripotent Stem Cells. *Stem Cells and Development*, *22*(14), 1991–2002. https://doi.org/10.1089/scd.2012.0490

Lyon, A. R., Sato, M., Hajjar, R. J., Samulski, R. J., & Harding, S. E. (2008). *Gene therapy: Targeting the myocardium*. https://doi.org/10.1136/hrt.2007.116483

Magnus, C. J., Lee, P. H., Atasoy, D., Su, H. H., Looger, L. L., & Sternson, S. M. (2011). Chemical and genetic engineering of selective ion channel-ligand interactions. *Science (New York, N.Y.)*, *333*(6047), 1292–1296. https://doi.org/10.1126/science.1206606

Magnus, C. J., Lee, P. H., Bonaventura, J., Zemla, R., Gomez, J. L., Ramirez, M. H., Hu, X., Galvan, A., Basu, J., Michaelides, M., & Sternson, S. M. (2019). Ultrapotent chemogenetics for research and potential clinical applications. *Science*, *364*(6436), eaav5282. https://doi.org/10.1126/science.aav5282

Malumbres, M., & Barbacid, M. (2009). Cell cycle, CDKs and cancer: A changing paradigm. *Nature Reviews Cancer*, *9*(3), 153–166. https://doi.org/10.1038/nrc2602

Marijianowski, M. M., van der Loos, C. M., Mohrschladt, M. F., & Becker, A. E. (1994). The neonatal heart has a relatively high content of total collagen and type I collagen, a condition that may explain the less compliant state. *Journal of the American College of Cardiology*, *23*(5), 1204–1208. https://doi.org/10.1016/0735-1097(94)90612-2

Martino, F., Perestrelo, A. R., Vinarský, V., Pagliari, S., & Forte, G. (2018). Cellular Mechanotransduction: From Tension to Function. *Frontiers in Physiology*, *9*, 824. https://doi.org/10.3389/fphys.2018.00824

Mehdipour, M., Park, S., & Huang, G. N. (2023). Unlocking cardiomyocyte renewal potential for myocardial regeneration therapy. *Journal of Molecular and Cellular Cardiology*, *177*, 9–20. https://doi.org/10.1016/j.yjmcc.2023.02.002

Meng, F., Kwok, M., Hui, Y. C., Wei, R., Hidalgo-Gonzalez, A., Walentinsson, A., Andersson, H., Bjerre, F. A., Wang, Q.-D., Andersen, D. C., Poon, E. N.-Y., Später, D., & Zebrowski, D. C. (2025). Matured hiPSC-derived cardiomyocytes possess dematuration plasticity. *Journal of Molecular and Cellular Cardiology Plus*, *12*, 100295. https://doi.org/10.1016/j.jmccpl.2025.100295

Miller, J. M., Meki, M. H., Ou, Q., George, S. A., Gams, A., Abouleisa, R. R. E., Tang, X.-L., Ahern, B. M., Giridharan, G. A., El-Baz, A., Hill, B. G., Satin, J., Conklin, D. J., Moslehi, J., Bolli, R., Ribeiro, A. J. S., Efimov, I. R., & Mohamed, T. M. A. (2020). Heart Slice Culture System Reliably Demonstrates Clinical Drug-Related Cardiotoxicity. *Toxicology and Applied Pharmacology*, *406*, 115213. https://doi.org/10.1016/j.taap.2020.115213

Mizzi, A., Tran, T., Mangar, D., & Camporesi, E. M. (2011). Amiodarone Supplants Lidocaine in ACLS and CPR Protocols. *Anesthesiology Clinics*, *29*(3), 535–545. https://doi.org/10.1016/j.anclin.2011.05.001

Moasser, M. M. (2007). The oncogene HER2: Its signaling and transforming functions and its role in human cancer pathogenesis. *Oncogene*, *26*(45), 6469–6487. https://doi.org/10.1038/sj.onc.1210477

Mollova, M., Bersell, K., Walsh, S., Savla, J., Das, L. T., Park, S.-Y., Silberstein, L. E., dos Remedios, C. G., Graham, D., Colan, S., & Kühn, B. (2013). Cardiomyocyte proliferation contributes to heart growth in young humans. *Proceedings of the National Academy of Sciences*, *110*(4), 1446–1451. https://doi.org/10.1073/pnas.1214608110

Monroe, T. O., Hill, M. C., Morikawa, Y., Leach, J. P., Heallen, T., Cao, S., Krijger, P. H. L., Laat, W. de, Wehrens, X. H. T., Rodney, G. G., & Martin, J. F. (2019). YAP Partially Reprograms Chromatin Accessibility to Directly Induce Adult Cardiogenesis In Vivo. *Developmental Cell*, *48*(6), 765-779.e7. https://doi.org/10.1016/j.devcel.2019.01.017

Morgan, D. (2007). *The cell cycle: Principles of control*. Oxford University Press.

Morikawa, Y., Heallen, T., Leach, J., Xiao, Y., & Martin, J. F. (2017). Dystrophin–glycoprotein complex sequesters Yap to inhibit cardiomyocyte proliferation. *Nature*, *547*(7662), 227–231. https://doi.org/10.1038/nature22979

Morikawa, Y., Kim, J. H., Li, R. G., Liu, L., Liu, S., Deshmukh, V., Hill, M. C., & Martin, J. F. (2025). YAP Overcomes Mechanical Barriers to Induce Mitotic Rounding and Adult Cardiomyocyte Division. *Circulation*, *151*(1), 76–93. https://doi.org/10.1161/CIRCULATIONAHA.123.066004

Morikawa, Y., Zhang, M., Heallen, T., Leach, J., Tao, G., Xiao, Y., Bai, Y., Li, W., Willerson, J. T., & Martin, J. F. (2015). Actin cytoskeletal remodeling with protrusion formation is essential for heart regeneration in Hippo-deficient mice. *Science Signaling*, *8*(375), ra41–ra41. https://doi.org/10.1126/scisignal.2005781

Moya, I. M., & Halder, G. (2018). Hippo–YAP/TAZ signalling in organ regeneration and regenerative medicine. *Nature Reviews Molecular Cell Biology 2018 20:4*, *20*(4), 211–226. https://doi.org/10.1038/s41580-018-0086-y

Nakano, H., Minami, I., Braas, D., Pappoe, H., Wu, X., Sagadevan, A., Vergnes, L., Fu, K., Morselli, M., Dunham, C., Ding, X., Stieg, A. Z., Gimzewski, J. K., Pellegrini, M., Clark, P. M., Reue, K., Lusis, A. J., Ribalet, B., Kurdistani, S. K., … Nakano, A. (2017). Glucose inhibits cardiac muscle maturation through nucleotide biosynthesis. *eLife*, *6*, e29330. https://doi.org/10.7554/eLife.29330

Nasmyth, K. (1996). Viewpoint: Putting the Cell Cycle in Order. *Science*, *274*(5293), 1643–1645. https://doi.org/10.1126/science.274.5293.1643

Nelson, W. J., & Nusse, R. (2004). Convergence of Wnt, beta-catenin, and cadherin pathways. *Science (New York, N.Y.)*, *303*(5663), 1483–1487. https://doi.org/10.1126/science.1094291

Nishimura, D. (2001). BioCarta. *Biotech Software & Internet Report*, *2*(3), 117–120. https://doi.org/10.1089/152791601750294344

Notari, M., Ventura-Rubio, A., Bedford-Guaus, S. J., Jorba, I., Mulero, L., Navajas, D., Martí, M., & Raya, Á. (2018). The local microenvironment limits the regenerative potential of the mouse neonatal heart. *Science Advances*, *4*(5), eaao5553. https://doi.org/10.1126/sciadv.aao5553

Nurse, P. (2000). A Long Twentieth Century of the Cell Cycle and Beyond. *Cell*, *100*(1), 71–78. https://doi.org/10.1016/S0092-8674(00)81684-0

Okita, K., Ichisaka, T., & Yamanaka, S. (2007). Generation of germline-competent induced pluripotent stem cells. *Nature*, *448*(7151), 313–317. https://doi.org/10.1038/nature05934

Olivetti, G., Melissari, M., Capasso, J. M., & Anversa, P. (1991). Cardiomyopathy of the aging human heart. Myocyte loss and reactive cellular hypertrophy. *Circulation Research*, *68*(6), 1560–1568. https://doi.org/10.1161/01.res.68.6.1560

Ou, Q., Jacobson, Z., Abouleisa, R. R. E., Tang, X.-L., Hindi, S. M., Kumar, A., Ivey, K. N., Giridharan, G., El-Baz, A., Brittian, K., Rood, B., Lin, Y.-H., Watson, S. A., Perbellini, F., McKinsey, T. A., Hill, B. G., Jones, S. P., Terracciano, C. M., Bolli, R., & Mohamed, T. M. A. (2019). Physiological Biomimetic Culture System for Pig and Human Heart Slices. *Circulation Research*, *125*(6), 628–642. https://doi.org/10.1161/CIRCRESAHA.119.314996

Padula, S. L., Velayutham, N., & Yutzey, K. E. (2021). Transcriptional Regulation of Postnatal Cardiomyocyte Maturation and Regeneration. *International Journal of Molecular Sciences*, *22*(6), Article 6. https://doi.org/10.3390/ijms22063288

Patterson, M., Barske, L., Van Handel, B., Rau, C. D., Gan, P., Sharma, A., Parikh, S., Denholtz, M., Huang, Y., Yamaguchi, Y., Shen, H., Allayee, H., Crump, J. G., Force, T. I., Lien, C.-L., Makita, T., Lusis, A. J., Kumar, S. R., & Sucov, H. M. (2017). Frequency of mononuclear diploid cardiomyocytes underlies natural variation in heart regeneration. *Nature Genetics*, *49*(9), 1346–1353. https://doi.org/10.1038/ng.3929

Pellarin, I., Dall'Acqua, A., Favero, A., Segatto, I., Rossi, V., Crestan, N., Karimbayli, J., Belletti, B., & Baldassarre, G. (2025). Cyclin-dependent protein kinases and cell cycle regulation in biology and disease. *Signal Transduction and Targeted Therapy*, *10*(1), 11. https://doi.org/10.1038/s41392-024-02080-z

Pettinato, A. M., Ladha, F. A., & Hinson, J. T. (2022). The Cardiac Sarcomere and Cell Cycle. *Current Cardiology Reports*, *24*(6), 623–630. https://doi.org/10.1007/s11886-022-01682-9

Pico, A. R., Kelder, T., van Iersel, M. P., Hanspers, K., Conklin, B. R., & Evelo, C. (2008). WikiPathways: Pathway editing for the people. *PLoS Biology*, *6*(7), e184. https://doi.org/10.1371/journal.pbio.0060184

Pinkas-Kramarski, R., Soussan, L., Waterman, H., Levkowitz, G., Alroy, I., Klapper, L., Lavi, S., Seger, R., Ratzkin, B. J., Sela, M., & Yarden, Y. (1996). Diversification of Neu differentiation factor and epidermal growth factor signaling by combinatorial receptor interactions. *The EMBO Journal*, *15*(10), 2452–2467.

Piquereau, J., & Ventura-Clapier, R. (2018). Maturation of Cardiac Energy Metabolism During Perinatal Development. *Frontiers in Physiology*, *9*. https://doi.org/10.3389/fphys.2018.00959

Poch, C. M., Foo, K. S., De Angelis, M. T., Jennbacken, K., Santamaria, G., Bähr, A., Wang, Q.-D., Reiter, F., Hornaschewitz, N., Zawada, D., Bozoglu, T., My, I., Meier, A., Dorn, T., Hege, S., Lehtinen, M. L., Tsoi, Y. L., Hovdal, D., Hyllner, J., … Laugwitz, K.-L. (2022). Migratory and anti-fibrotic programmes define the regenerative potential of human cardiac progenitors. *Nature Cell Biology*, *24*(5), 659–671. https://doi.org/10.1038/s41556-022-00899-8

Porrello, E. R., Mahmoud, A. I., Simpson, E., Hill, J. A., Richardson, J. A., Olson, E. N., & Sadek, H. A. (2011). Transient Regenerative Potential of the Neonatal Mouse Heart. *Science*, *331*(6020), 1078–1080. https://doi.org/10.1126/science.1200708

Poss, K. D., Wilson, L. G., & Keating, M. T. (2002). Heart Regeneration in Zebrafish. *Science*, *298*(5601), 2188–2190. https://doi.org/10.1126/science.1077857

Potter, J. D., & Gergely, J. (1975). The regulatory system of the actin-myosin interaction. *Recent Advances in Studies on Cardiac Structure and Metabolism*, *5*, 235–244.

Pricolo, M. R., López-Unzu, M. A., Vicente, N., Morales-López, C., Huerta-López, C., Pérez-Franco, W., Dumitru, A. C., Espinosa, F. M., Sanchez, M. I., Garcia, R., Silva-Rojas, R., Herrero-Galán, E., & Alegre-Cebollada, J. (2025). *Titin cleavage in living cardiomyocytes induces sarcomere disassembly but does not* *trigger cell proliferation* (p. 2025.04.22.645658). bioRxiv. https://doi.org/10.1101/2025.04.22.645658

Puente, B. N., Kimura, W., Muralidhar, S. A., Moon, J., Amatruda, J. F., Phelps, K. L., Grinsfelder, D., Rothermel, B. A., Chen, R., Garcia, J. A., Santos, C. X., Thet, S., Mori, E., Kinter, M. T., Rindler, P. M., Zacchigna, S., Mukherjee, S., Chen, D. J., Mahmoud, A. I., … Sadek, H. A. (2014). The oxygen-rich postnatal environment induces cardiomyocyte cell-cycle arrest through DNA damage response. *Cell*, *157*(3), 565–579. https://doi.org/10.1016/j.cell.2014.03.032

Racca, A. W., Klaiman, J. M., Pioner, J. M., Cheng, Y., Beck, A. E., Moussavi-Harami, F., Bamshad, M. J., & Regnier, M. (2016). Contractile properties of developing human fetal cardiac muscle. *The Journal of Physiology*, *594*(2), 437–452. https://doi.org/10.1113/JP271290

Ran, F. A., Hsu, P. D., Wright, J., Agarwala, V., Scott, D. A., & Zhang, F. (2013). Genome engineering using the CRISPR-Cas9 system. *Nature Protocols*, *8*(11), 2281–2308. https://doi.org/10.1038/nprot.2013.143

Rausch, V., & Hansen, C. G. (2020). The Hippo Pathway, YAP/TAZ, and the Plasma Membrane. *Trends in Cell Biology*, *30*(1), 32–48. https://doi.org/10.1016/j.tcb.2019.10.005

Remien, K., & Majmundar, S. H. (2025). Physiology, Fetal Circulation. In *StatPearls*. StatPearls Publishing. http://www.ncbi.nlm.nih.gov/books/NBK539710/

Robinson, T. F., & Kinne, R. K. H. (1990). *Cardiac myocyte-connective tissue interactions in health and disease*. Karger.

Robinton, D. A., & Daley, G. Q. (2012). The promise of induced pluripotent stem cells in research and therapy. *Nature*, *481*(7381), 295–305. https://doi.org/10.1038/nature10761

Roth, G. A., Mensah, G. A., Johnson, C. O., Addolorato, G., Ammirati, E., Baddour, L. M., Barengo, N. C., Beaton, A. Z., Benjamin, E. J., Benziger, C. P., Bonny, A., Brauer, M., Brodmann, M., Cahill, T. J., Carapetis, J., Catapano, A. L., Chugh, S. S., Cooper, L. T., Coresh, J., … Fuster, V. (2020). Global Burden of Cardiovascular Diseases and Risk Factors, 1990–2019. *Journal of the American College of Cardiology*, *76*(25), 2982–3021. https://doi.org/10.1016/j.jacc.2020.11.010

Rudolph, A. M., & Heymann, M. A. (1969). *Circulatory Changes during Growth in the Fetal Lamb*. https://doi.org/10.1161/01.RES.26.3.289

Sadek, H., & Olson, E. N. (2020). Toward the Goal of Human Heart Regeneration. *Cell Stem Cell*, *26*(1), 7–16. https://doi.org/10.1016/j.stem.2019.12.004

Schindelin, J., Arganda-Carreras, I., Frise, E., Kaynig, V., Longair, M., Pietzsch, T., Preibisch, S., Rueden, C., Saalfeld, S., Schmid, B., Tinevez, J.-Y., White, D. J., Hartenstein, V., Eliceiri, K., Tomancak, P., & Cardona, A. (2012). Fiji: An open-source platform for biological-image analysis. *Nature Methods*, *9*(7), 676–682. https://doi.org/10.1038/nmeth.2019

Schlesinger, J., Schueler, M., Grunert, M., Fischer, J. J., Zhang, Q., Krueger, T., Lange, M., Tönjes, M., Dunkel, I., & Sperling, S. R. (2011). The Cardiac Transcription Network Modulated by Gata4, Mef2a, Nkx2.5, Srf, Histone Modifications, and MicroRNAs. *PLOS Genetics*, *7*(2), e1001313. https://doi.org/10.1371/journal.pgen.1001313

Secco, I., & Giacca, M. (2023). Regulation of endogenous cardiomyocyte proliferation: The known unknowns. *Journal of Molecular and Cellular Cardiology*, *179*, 80–89. https://doi.org/10.1016/j.yjmcc.2023.04.001

Senyo, S. E., Steinhauser, M. L., Pizzimenti, C. L., Yang, V. K., Cai, L., Wang, M., Wu, T.-D., Guerquin-Kern, J.-L., Lechene, C. P., & Lee, R. T. (2013). Mammalian heart renewal by pre-existing cardiomyocytes. *Nature*, *493*(7432), 433–436. https://doi.org/10.1038/nature11682

Severs, N. J. (2000). The cardiac muscle cell. *BioEssays*, *22*(2), 188–199. https://doi.org/10.1002/(SICI)1521-1878(200002)22:2%253C188::AID-BIES10%253E3.0.CO;2-T

Sheikh, F., Lyon, R. C., & Chen, J. (2015). Functions of Myosin Light Chain-2 (MYL2) In Cardiac Muscle and Disease. *Gene*, *569*(1), 14–20. https://doi.org/10.1016/j.gene.2015.06.027

Shen, H., Gan, P., Wang, K., Darehzereshki, A., Wang, K., Kumar, S. R., Lien, C.-L., Patterson, M., Tao, G., & Sucov, H. M. (2020). Mononuclear diploid cardiomyocytes support neonatal mouse heart regeneration in response to paracrine IGF2 signaling. *eLife*, *9*, e53071. https://doi.org/10.7554/eLife.53071

Shih, H. T. (1994). Anatomy of the action potential in the heart. *Texas Heart Institute Journal*, *21*(1), 30–41.

Siedner, S., Krüger, M., Schroeter, M., Metzler, D., Roell, W., Fleischmann, B. K., Hescheler, J., Pfitzer, G., & Stehle, R. (2003). Developmental changes in contractility and sarcomeric proteins from the early embryonic to the adult stage in the mouse heart. *The Journal of Physiology*, *548*(Pt 2), 493–505. https://doi.org/10.1113/jphysiol.2002.036509

Siegel, R. E. (1968). *Galen's System of Physiology and Medicine: An Analysis of His Doctrines and Observations on Blood Flow, Respiration, Humors and Internal Diseases*. Karger Medical and Scientific Publishers.

Slamon, D. J., Clark, G. M., Wong, S. G., Levin, W. J., Ullrich, A., & McGuire, W. L. (1987). Human breast cancer: Correlation of relapse and survival with amplification of the HER-2/neu oncogene. *Science (New York, N.Y.)*, *235*(4785), 177–182. https://doi.org/10.1126/science.3798106

Smolich, J. J., Soust, M., Berger, P. J., & Walker, A. M. (1992). Indirect relation between rises in oxygen consumption and left ventricular output at birth in lambs. *Circulation Research*, *71*(2), 443–450. https://doi.org/10.1161/01.res.71.2.443

Sönmez, M., Stüdemann, T., Manthey, C., Covic, A., Shehata, N., Im, J., Schwarzova, B., Rössinger, J., Srikantharajah, R., Shibamiya, A., Schwedhelm, E., Eschenhagen, T., Christ, T., & Weinberger, F. (2025). Modulation of cardiomyocyte contractility and action potentials with chemogenetic chloride currents. *The Journal of Physiology*, *603*(6), 1399–1415. https://doi.org/10.1113/JP286428

Soonpaa, M. H., Kim, K. K., Pajak, L., Franklin, M., & Field, L. J. (1996). Cardiomyocyte DNA synthesis and binucleation during murine development. *American Journal of Physiology-Heart and Circulatory Physiology*, *271*(5), H2183–H2189. https://doi.org/10.1152/ajpheart.1996.271.5.H2183

Soulez, M., Tuil, D., Kahn, A., & Gilgenkrantz, H. (1996). The Serum Response Factor (SRF) Is Needed for Muscle-Specific Activation of CArG Boxes. *Biochemical and Biophysical Research Communications*, *219*(2), 418–422. https://doi.org/10.1006/bbrc.1996.0248

Squire, J. M. (1997). Architecture and function in the muscle sarcomere. *Current Opinion in Structural Biology*, *7*(2), 247–257. https://doi.org/10.1016/S0959-440X(97)80033-4

Stein, J. M., Arslan, U., Franken, M., de Greef, J. C., E. Harding, S., Mohammadi, N., Orlova, V. V., Bellin, M., Mummery, C. L., & van Meer, B. J. (2022). Software Tool for Automatic Quantification of Sarcomere Length and Organization in

Fixed and Live 2D and 3D Muscle Cell Cultures In Vitro. *Current Protocols*, *2*(7), e462. https://doi.org/10.1002/cpz1.462

Sweeney, H. L., & Holzbaur, E. L. F. (2018). Motor Proteins. *Cold Spring Harbor Perspectives in Biology*, *10*(5), a021931. https://doi.org/10.1101/cshperspect.a021931

Takahashi, K., & Yamanaka, S. (2006). Induction of Pluripotent Stem Cells from Mouse Embryonic and Adult Fibroblast Cultures by Defined Factors. *Cell*, *126*(4), 663–676. https://doi.org/10.1016/j.cell.2006.07.024

Torrini, C., Cubero, R. J., Dirkx, E., Braga, L., Ali, H., Prosdocimo, G., Gutierrez, M. I., Collesi, C., Licastro, D., Zentilin, L., Mano, M., Zacchigna, S., Vendruscolo, M., Marsili, M., Samal, A., & Giacca, M. (2019). Common Regulatory Pathways Mediate Activity of MicroRNAs Inducing Cardiomyocyte Proliferation. *Cell Reports*, *27*(9), 2759-2771.e5. https://doi.org/10.1016/J.CELREP.2019.05.005

Townsend, N., Kazakiewicz, D., Wright, F. L., Timmis, A., Huculeci, R., Torbica, A., Gale, C. P., Achenbach, S., Weidinger, F., & Vardas, P. (2022). Epidemiology of cardiovascular disease in Europe. *Nature Reviews Cardiology*, *19*(2), 133–143. https://doi.org/10.1038/S41569-021-00607-3;SUBJMETA=174,4019,478,692,699,700,75;KWRD=CARDIOLOGY,CARDIOVASCULAR+DISEASES,EPIDEMIOLOGY

Tsai, Y.-W., Tseng, Y.-S., Wu, Y.-S., Song, W.-L., You, M.-Y., Hsu, Y.-C., Chen, W.-P., Huang, W.-H., Chng, J.-C., Lim, C.-L., Wei, K.-H., Ben Lai, S.-L., Lee, W.-C., & Yang, K.-C. (2025). N-Cadherin promotes cardiac regeneration by potentiating pro-mitotic β-Catenin signaling in cardiomyocytes. *Nature Communications*, *16*, 896. https://doi.org/10.1038/s41467-025-56216-y

Ulmer, B. M., Stoehr, A., Schulze, M. L., Patel, S., Gucek, M., Mannhardt, I., Funcke, S., Murphy, E., Eschenhagen, T., & Hansen, A. (2018). Contractile Work Contributes to Maturation of Energy Metabolism in hiPSC-Derived Cardiomyocytes. *Stem Cell Reports*, *10*(3), 834–847. https://doi.org/10.1016/j.stemcr.2018.01.039

Uribe, V., Ramadass, R., Dogra, D., Rasouli, S. J., Gunawan, F., Nakajima, H., Chiba, A., Reischauer, S., Mochizuki, N., & Stainier, D. Y. R. (2018). In vivo analysis of cardiomyocyte proliferation during trabeculation. *Development*, *145*(14), dev164194. https://doi.org/10.1242/dev.164194

Vartiainen, M. K., Guettler, S., Larijani, B., & Treisman, R. (2007). Nuclear actin regulates dynamic subcellular localization and activity of the SRF cofactor MAL. *Science (New York, N.Y.)*, *316*(5832), 1749–1752. https://doi.org/10.1126/science.1141084

Velayutham, N., Agnew, E. J., & Yutzey, K. E. (2019). Postnatal Cardiac Development and Regenerative Potential in Large Mammals. *Pediatric Cardiology*, *40*(7), 1345–1358. https://doi.org/10.1007/s00246-019-02163-7

Verdaasdonk, J. S., & Bloom, K. (2011). Centromeres: Unique chromatin structures that drive chromosome segregation. *Nature Reviews. Molecular Cell Biology*, *12*(5), 320–332. https://doi.org/10.1038/nrm3107

Versaevel, M., Braquenier, J.-B., Riaz, M., Grevesse, T., Lantoine, J., & Gabriele, S. (2014). Super-resolution microscopy reveals LINC complex recruitment at nuclear indentation sites. *Scientific Reports*, *4*(1), 7362. https://doi.org/10.1038/srep07362

von Gise, A., Lin, Z., Schlegelmilch, K., Honor, L. B., Pan, G. M., Buck, J. N., Ma, Q., Ishiwata, T., Zhou, B., Camargo, F. D., & Pu, W. T. (2012). YAP1, the nuclear target of Hippo signaling, stimulates heart growth through cardiomyocyte proliferation but not hypertrophy. *Proceedings of the National Academy of Sciences*, *109*(7), 2394–2399. https://doi.org/10.1073/pnas.1116136109

Vreeker, A., Stuijvenberg, L. van, Hund, T. J., Mohler, P. J., Nikkels, P. G. J., & Veen, T. A. B. van. (2014). Assembly of the Cardiac Intercalated Disk during Pre- and Postnatal Development of the Human Heart. *PLOS ONE*, *9*(4), e94722. https://doi.org/10.1371/journal.pone.0094722

Walczak, C. E., Cai, S., & Khodjakov, A. (2010). Mechanisms of chromosome behaviour during mitosis. *Nature Reviews. Molecular Cell Biology*, *11*(2), 91–102. https://doi.org/10.1038/nrm2832

Walklate, J., Ujfalusi, Z., & Geeves, M. A. (2016). Myosin isoforms and the mechanochemical cross-bridge cycle. *The Journal of Experimental Biology*, *219*(2), 168–174. https://doi.org/10.1242/jeb.124594

Wamstad, J. A., Alexander, J. M., Truty, R. M., Shrikumar, A., Li, F., Eilertson, K. E., Ding, H., Wylie, J. N., Pico, A. R., Capra, J. A., Erwin, G., Kattman, S. J., Keller, G. M., Srivastava, D., Levine, S. S., Pollard, K. S., Holloway, A. K., Boyer, L. A., & Bruneau, B. G. (2012). Dynamic and Coordinated Epigenetic Regulation of Developmental Transitions in the Cardiac Lineage. *Cell*, *151*(1), 206–220. https://doi.org/10.1016/j.cell.2012.07.035

Wang, S., Stoops, E., CP, U., Markus, B., Reuveny, A., Ordan, E., & Volk, T. (2018). Mechanotransduction via the LINC complex regulates DNA replication in myonuclei. *Journal of Cell Biology*, *217*(6), 2005–2018. https://doi.org/10.1083/jcb.201708137

Wang, Z., Long, D. W., Huang, Y., Chen, W. C. W., Kim, K., & Wang, Y. (2019). Decellularized neonatal cardiac extracellular matrix prevents widespread ventricular remodeling in adult mammals after myocardial infarction. *Acta Biomaterialia*, *87*, 140–151. https://doi.org/10.1016/j.actbio.2019.01.062

Watson, S. A., Duff, J., Bardi, I., Zabielska, M., Atanur, S. S., Jabbour, R. J., Simon, A., Tomas, A., Smolenski, R. T., Harding, S. E., Perbellini, F., & Terracciano, C. M. (2019). Biomimetic electromechanical stimulation to maintain adult myocardial slices in vitro. *Nature Communications*, *10*(1), 2168. https://doi.org/10.1038/s41467-019-10175-3

Wei, Y., Walcott, G., Nguyen, T., Geng, X., Guragain, B., Zhang, H., Green, A., Rosa-Garrido, M., Rogers, J. M., Garry, D. J., Ye, L., & Zhang, J. (2025). Follistatin From hiPSC-Cardiomyocytes Promotes Myocyte Proliferation in Pigs With Postinfarction LV Remodeling. *Circulation Research*, *136*(2), 161–176. https://doi.org/10.1161/CIRCRESAHA.124.325562

Weigert, M., & Schmidt, U. (2022). Nuclei Instance Segmentation and Classification in Histopathology Images with Stardist. *2022 IEEE International Symposium on Biomedical Imaging Challenges (ISBIC)*, 1–4. https://doi.org/10.1109/ISBIC56247.2022.9854534

Weinberger, F., Mannhardt, I., & Eschenhagen, T. (2017). Engineering Cardiac Muscle Tissue. *Circulation Research*, *120*(9), 1487–1500. https://doi.org/10.1161/CIRCRESAHA.117.310738

Wierstra, I. (2013). Chapter Three - The Transcription Factor FOXM1 (Forkhead box M1): Proliferation-Specific Expression, Transcription Factor Function, Target Genes, Mouse Models, and Normal Biological Roles**The present chapter is Part I of a two-part review on the transcription factor FOXM1. Part II of this FOXM1 review is published in Volume 119 of Advances in Cancer Research: Inken Wierstra, FOXM1 (Forkhead box M1) in tumorigenesis: overexpression in human cancer, implication in tumorigenesis, oncogenic functions, tumorsuppressive properties and target of anti-cancer therapy. Advances in Cancer Research, 2013, Volume 119, in press. In K. D. Tew & P. B. Fisher (Eds.), *Advances in Cancer Research* (Vol. 118, pp. 97–398). Academic Press. https://doi.org/10.1016/B978-0-12-407173-5.00004-2

Williams, C., Quinn, K. P., Georgakoudi, I., & Black, L. D. (2014). Young developmental age cardiac extracellular matrix promotes the expansion of neonatal cardiomyocytes in vitro. *Acta Biomaterialia*, *10*(1), 194–204. https://doi.org/10.1016/j.actbio.2013.08.037

Wu, C.-C., Jeratsch, S., Graumann, J., & Stainier, D. Y. R. (2020). Modulation of Mammalian Cardiomyocyte Cytokinesis by the Extracellular Matrix. *Circulation Research*, *127*(7), 896–907. https://doi.org/10.1161/CIRCRESAHA.119.316303

Wu, P., Deng, G., Sai, X., Guo, H., Huang, H., & Zhu, P. (2021). Maturation strategies and limitations of induced pluripotent stem cell-derived cardiomyocytes. *Bioscience Reports*, *41*(6), BSR20200833. https://doi.org/10.1042/BSR20200833

Wu, T., Hu, E., Xu, S., Chen, M., Guo, P., Dai, Z., Feng, T., Zhou, L., Tang, W., Zhan, L., Fu, X., Liu, S., Bo, X., & Yu, G. (2021). clusterProfiler 4.0: A universal enrichment tool for interpreting omics data. *Innovation (Cambridge (Mass.))*, *2*(3), 100141. https://doi.org/10.1016/j.xinn.2021.100141

Xiao, F., Nguyen, N. U. N., Wang, P., Li, S., Hsu, C.-C., Thet, S., Kimura, W., Luo, X., Lam, N. T., Menendez-Montes, I., Elhelaly, W. M., Cardoso, A. C., Pereira, A. H. M., Singh, R., Sadayappan, S., Kanchwala, M., Xing, C., Ladha, F. A., Hinson, J. T., … Sadek, H. A. (2024). Adducin Regulates Sarcomere Disassembly During Cardiomyocyte Mitosis. *Circulation*, *150*(10), 791–805. https://doi.org/10.1161/CIRCULATIONAHA.122.059102

Xin, M., Kim, Y., Sutherland, L. B., Murakami, M., Qi, X., McAnally, J., Porrello, E. R., Mahmoud, A. I., Tan, W., Shelton, J. M., Richardson, J. A., Sadek, H. A., Bassel-Duby, R., & Olson, E. N. (2013). Hippo pathway effector Yap promotes cardiac regeneration. *Proceedings of the National Academy of Sciences*, *110*(34), 13839–13844. https://doi.org/10.1073/pnas.1313192110

Xu, Q., Chen, X., Zhao, C., Liu, Y., Wang, J., Ao, X., & Ding, W. (2025). Cell cycle arrest of cardiomyocytes in the context of cardiac regeneration. *Frontiers in Cardiovascular Medicine*, *12*. https://doi.org/10.3389/fcvm.2025.1538546

Xuan, Q., Li, J., Feng, Z., Zhu, L., Jiang, T., Li, H., Liu, M., Qian, X., & Ma, X. (2025). Modulation of PPAR-α and PPAR-γ Influences Cardiomyocyte Growth and Cardiac Remodeling. *IUBMB Life*, *77*(6), e70035. https://doi.org/10.1002/iub.70035

Yahalom-Ronen, Y., Rajchman, D., Sarig, R., Geiger, B., & Tzahor, E. (2015). Reduced matrix rigidity promotes neonatal cardiomyocyte dedifferentiation, proliferation and clonal expansion. *eLife*, *4*, e07455. https://doi.org/10.7554/eLife.07455

Yang, X., Pabon, L., & Murry, C. E. (2014). Engineering adolescence: Maturation of human pluripotent stem cell-derived cardiomyocytes. *Circulation Research*, *114*(3), 511–523. https://doi.org/10.1161/CIRCRESAHA.114.300558

Ye, L., D'Agostino, G., Loo, S. J., Wang, C. X., Su, L. P., Tan, S. H., Tee, G. Z., Pua, C. J., Pena, E. M., Cheng, R. B., Chen, W. C., Abdurrachim, D., Lalic, J., Tan, R. S., Lee, T. H., Zhang, J., & Cook, S. A. (2018). Early Regenerative Capacity in the Porcine Heart. *Circulation*, *138*(24), 2798–2808. https://doi.org/10.1161/CIRCULATIONAHA.117.031542

Yu, J., Vodyanik, M. A., Smuga-Otto, K., Antosiewicz-Bourget, J., Frane, J. L., Tian, S., Nie, J., Jonsdottir, G. A., Ruotti, V., Stewart, R., Slukvin, I. I., & Thomson, J. A. (2007). Induced Pluripotent Stem Cell Lines Derived from Human Somatic Cells. *Science*, *318*(5858), 1917–1920. https://doi.org/10.1126/science.1151526

Yu, Z., Zhang, L., Cattaneo, P., Guimarães-Camboa, N., Fang, X., Gu, Y., Peterson, K. L., Bogomolovas, J., Cuitino, C., Leone, G. W., Chen, J., & Evans, S. M. (2023). Increasing Mononuclear Diploid Cardiomyocytes by Loss of E2F Transcription Factor 7/8 Fails to Improve Cardiac Regeneration After Infarct. *Circulation*, *147*(2), 183. https://doi.org/10.1161/CIRCULATIONAHA.122.061018

Yuan, Q., Maas, R. G. C., Brouwer, E. C. J., Pei, J., Blok, C. S., Popovic, M. A., Paauw, N. J., Bovenschen, N., Hjortnaes, J., Harakalova, M., Doevendans, P. A., Sluijter, J. P. G., van der Velden, J., & Buikema, J. W. (2022). Sarcomere Disassembly and Transfection Efficiency in Proliferating Human iPSC-Derived Cardiomyocytes. *Journal of Cardiovascular Development and Disease*, *9*(2), 43. https://doi.org/10.3390/jcdd9020043

Zhu, F., Meng, Q., Yu, Y., Shao, L., & Shen, Z. (2021). Adult Cardiomyocyte Proliferation: A New Insight for Myocardial Infarction Therapy. *Journal of Cardiovascular Translational Research*, *14*(3), 457–466. https://doi.org/10.1007/s12265-020-10067-8

Zhu, W., Zhang, E., Zhao, M., Chong, Z., Fan, C., Tang, Y., Hunter, J. D., Borovjagin, A. V., Walcott, G. P., Chen, J. Y., Qin, G., & Zhang, J. (2018). Regenerative Potential of Neonatal Porcine Hearts. *Circulation*, *138*(24), 2809–2816. https://doi.org/10.1161/CIRCULATIONAHA.118.034886

Zimmermann, W.-H., Schneiderbanger, K., Schubert, P., Didié, M., Münzel, F., Heubach, J. F., Kostin, S., Neuhuber, W. L., & Eschenhagen, T. (2002). Tissue engineering of a differentiated cardiac muscle construct. *Circulation Research*, *90*(2), 223–230. https://doi.org/10.1161/hh0202.103644

Zuppo, D. A., Missinato, M. A., Santana-Santos, L., Li, G., Benos, P. V., & Tsang, M. (2023). Foxm1 regulates cardiomyocyte proliferation in adult zebrafish after cardiac injury. *Development (Cambridge, England)*, *150*(6), dev201163. https://doi.org/10.1242/dev.201163

Appendix

i) Table of Figures

ii) Macro and codes

1. Stardist batch analysis Macro ImageJ/Fiji

```
//make sure to set windowless that option. from Plugins --> Bio-Formats --> Bio-
Formats plug-ins configurations --> in Formats tab go down the list to zeiss czi -
-> check windowless
// Ask for the input folder
input = getDirectory("Choose the Input Folder");

// Ask for the output folder
output = getDirectory("Choose the Output Folder");

processFolder(input);

// function to scan folders/subfolders/files to find files with correct suffix
function processFolder(input) {
    list = getFileList(input);
    list = Array.sort(list);
    for (i = 0; i < list.length; i++) {
// Check if the file has the .czi extension
        if (endsWith(list[i], ".czi")) {
            open(input + list[i]);
//   run("Split Channels");
                          //close(); if the opened channel is not Dapi
                          //close(); if the opened channel is not Dapi
            myDir = getDirectory("image");
            name1 = getTitle();
            name2 = File.nameWithoutExtension;

                run("Duplicate...", "title=[Raw Image]");
                run("Set Scale...", "distance=4.6 known=1 pixel=4.6 unit=um"); //in
case 2048 resolution used
                          run("Command From Macro",
"command=[de.csbdresden.stardist.StarDist2D], args=['input':'Raw Image',
'modelChoice':'Versatile (fluorescent nuclei)', 'normalizeInput':'true',
'percentileBottom':'1.0', 'percentileTop':'99.8', 'probThresh':'0.75',
'nmsThresh':'0.4', 'outputType':'Both', 'nTiles':'1', 'excludeBoundary':'2',
'roiPosition':'Automatic', 'verbose':'false', 'showCsbdeepProgress':'false',
'showProbAndDist':'false'], process=[false]");

            selectWindow("Label Image");
            rename(name1);

            run("Set Measurements...", "area perimeter limit display redirect=None
decimal=3 circularity");

           roiManager("Measure");
           saveAs("Tiff", output + name2 + ".tiff");
```

```
              //  roiManager("Save", output + name2 + ".zip");
                roiManager("delete");
                close("ROI Manager");
                saveAs("Results", output + name2 + ".csv");
                run("Clear Results");
                close("Results");
                close();
                close();
                close();

                print("Processing: " + input + list[i]);
                print("Saving to: " + output);
            } else {
                // Print a message indicating the file was skipped
                 print("Skipping: " + list[i] + " (not a .czi file)");
            }
        }
    }
```

2. Python script collecting Dapi count from each StarDist-generated excel file into one csv file

```
import pandas as pd
import os
# Specify the directory containing the CSV files
directory = 'file path'
# Create an empty list to store results
results = []

# Loop through all files in the specified directory
for filename in os.listdir(directory):
    if filename.endswith('.csv'):  # Check if the file is a CSV file
        file_path = os.path.join(directory, filename)

        print(f"Checking file: {file_path}...")  # Checkpoint 1: Find the file

        # Try to open and read the CSV file
        try:
            df = pd.read_csv(file_path)
            # Checkpoint 3: File name
            print(f"Successfully opened file: {filename}")  # Checkpoint 2: Open the
file
            # Count the number of rows
            num_rows = df.shape[0]
            # Checkpoint 4: Number of rows
            print(f"Number of rows in '{filename}': {num_rows}")  # Row count

            # Append the filename and number of rows to the results list
            results.append({'File Name': filename, 'Row Count': num_rows,
'Success': 'Yes'})

        except Exception as e:
            # If there's an error, log it
            print(f"Could not read {filename}: {e}")  # Log error message
            results.append({'File Name': filename, 'Row Count': 0, 'Success': 'No'})
            continue  # Move to the next file

# Convert results to a DataFrame
results_df = pd.DataFrame(results)

# Specify the path to save the new Excel file
output_file_path = Dapi_counts.csv'  # Change output file extension to .csv
# Save the results to a new CSV file
results_df.to_csv(output_file_path, index=False)

print(f"Row counts saved to {output_file_path}.")
```

3. RScript for side bar graph

```
install.packages("readxl")
install.packages("dplyr")
install.packages("ggplot2")
install.packages("BiocManager")
BiocManager::install("clusterProfiler")
BiocManager::install("org.Hs.eg.db")
BiocManager::install("enrichplot")

# Load required libraries
library(readxl)
library(dplyr)
library(ggplot2)
library(stringr)

# === 1. Read Excel file ===
gsea_data <- read_excel("file path and name.xlsx”)

# === 2. Filter for significant pathways only (FDR < 0.05) ===
upregulated <- gsea_data%>% filter(NES > 0)%>% slice_max(NES, n = 10, with_ties = FALSE)
downregulated <- gsea_data%>% filter(NES < 0)%>% slice_min(NES, n = 10, with_ties = FALSE)

gsea_balanced <- bind_rows(downregulated, upregulated)%>%
  distinct(Transcription_regulator, .keep_all = TRUE)%>%        # drop any duplicate labels
  mutate(Transcription_regulator = stringr::str_wrap(Transcription_regulator, width = 40))

# --- Plot: order categories by NES directly in aes() ---
plot_gsea <- ggplot(
  gsea_balanced,
  aes(x = NES, y = reorder(Transcription_regulator, NES), fill = NES)
) +
  geom_col() +
  scale_fill_gradient2(low = "blue", mid = "white", high = "red", midpoint = 0, name = "NES") +
  theme_minimal(base_size = 12) +
  labs(title = "", x = "Normalized Enrichment Score (NES)", y = NULL) +
  theme(axis.text.y = element_text(size = 10, color ="black"),
        plot.title = element_text(hjust = 0.5, face = "bold"),
        legend.position = "right")

ggsave("File path and name",
       plot = plot_gsea, dpi = 600, width = 10, height = 6, units = "in")
```

4. RScript for Heatmaps

```
# Load required libraries
library(dplyr)
library(readr)
library(ggplot2)
library(readxl)
library(pheatmap)
library(RColorBrewer)
library(tibble)
library(grid)

# Read the reorganized Excel file
data <- read_excel(“file path and name.xlsx”)

# Extract gene names (now in columns)
genes <- colnames(data)[-1]  # Exclude the first column (sample names)
#print(head(genes))

# Convert the data to a numeric matrix
RNAseq_numeric <- data%>%
  select(-1)%>%  # Exclude the first column (sample names)
  as.matrix()

# Set row names to sample names
rownames(RNAseq_numeric) <- data[[1]]

# Define heatmap colors
heatmap_colors <- colorRampPalette(c("royalblue", "white", "red"))(100)
#RNAPlot<-t(RNAseq_numeric)

# Plot the heatmap
pheatmap(RNAseq_numeric,
         color = heatmap_colors,
         cluster_rows = FALSE,  # Cluster the rows (samples)
         cluster_cols = FALSE,  # Cluster the columns (genes)
         show_rownames = TRUE,  # Show row names (samples)
         show_colnames = FALSE,  # Show column names (genes)
         scale = "row",      # Scale by column (genes)
         fontsize = 7,          # Font size for row and column names
         cellwidth = 7,         # Width of each cell (adjust as needed)
         cellheight = 7,        # Height of each cell (adjust as needed)
         treeheight_col = 20,   # Height of the column dendrogram
         border_color = "white",
         angle_col = 90, # Add white outlines to each cell
         filename = "file path and name.png",
         dpi=600
 )
```

ACKNOWLEGEMENT

This work would not have been possible without the support and contribution of many people.
First, I would like to thank Prof. Dr. Eschenhagen for giving me the opportunity to join his institute and pursue this project. His grant support, continuous feedback and deep scientific insight helped shaping the direction of this work.

I am grateful to Prof. Dr. Baris Tursun for his interest in my project and for providing valuable feedback during supervision process.

My deepest thanks go to Dr. Florian Weinberger, who offered me this PhD position and closely supervised my work throughout these 4 years in Hamburg and Madrid. He encouraged me to always take initiative and to bring new ideas to the table. His guidance, patience, and creativity have been vital both for the success of this project and for my development as a scientist. He provided me with access to the facilities in both cities, and his strong network contributed greatly to the success of this project.

I would also like to thank my colleagues and team members in Hamburg and Madrid for their help in experiments and for making the PhD journey enjoyable despite its challenges. In particular, I thank Marie Nehring for sharing this journey with me and Gesa Rossler for the many coffee breaks and cakes that made the days lighter. I am grateful to Rajiven Srikantharajah for his assistance with microscopy, Moritz-Meyer-Jens for teaching me Western blot and Simona Parretta for supporting with live cell imaging, and Maggie Nandudu for always offering me help when I most needed. I also thank Dr. Sandra Laufer for providing the UKEi-001a WT cell line, Dr. Ingke Braren for providing the PSAM4 AAV6, and the UKE core Facilities for technical assistance.

My sincere appreciation goes to the technical staff who taught me the laboratory skills essential for this project. I specially thank Thomas Schulze and Birgit Klampe from the stem call lab, and Elisabeth Krämer, Grit Höppner, Ellen Orthey, and Angelika Piasecki from the molecular biology labs for their invaluable expertise and support.

I am also thankful to our collaborators Munich, Münster, and at CNIC in Madrid, as well as to OrganVision and DZHK for their financial support.

Finally, I would like to express my gratitude to my family and friends for supporting me throughout this journey and helping me maintain a good mental health during challenging times. Above all I thank my husband George for his constant support both in daily life and in my work, including help with coding. I am also grateful to our newest family addition my niece Mikaela Tadros who filled our life with joy, and to Lilli Schwarz for the padel games and bringing creativity even into the choice of histology colours.

DECLARATION OF ACADEMIC HONESTY

I hereby declare that my thesis titled:

“Evidence for the inhibition of cardiomyocytes cycle activity by cardiac contraction“

carried out at the Institute of Experimental Pharmacology and Toxicology, UKE Hamburg in the laboratory of Prof. Dr. Thomas Eschenhagen, with the supervision of Prof. Dr. Boris Tursun and Dr. Florian Weinberger for the Department of Biology, was written independently by myself. No other sources or aids than those indicated were used. The submitted written form of the thesis complies with the electronic version. This thesis was not handed in any other form for another examination procedure.

Hamburg, 20.10.2025 Nancy Sorial Samy Shehata